Gas Mass Fractions from XMM-Newton

Ferreira, Desiree Della Monica; Pedersen, Kristian

Publication date:
2011

Document Version
Publisher's PDF, also known as Version of record

GAS MASS FRACTIONS FROM XMM-NEWTON

DESIREE DELLA MONICA FERREIRA

Dissertation
Submitted for the Degree

PHILOSOPHIÆ DOCTOR

Dark Cosmology Centre
Niels Bohr Institute
Faculty of Science
Copenhagen University

Submission: *December 20th, 2010*
Defence: *March 4th, 2011*

Supervisor: *Assoc. Prof. Kristian Pedersen*

Opponents: *Dr. Stefano Ettori*
Dr. Sabine Schindler

CONTENTS

LIST OF FIGURES

LIST OF TABLES

ACKNOWLEDGMENTS

"A vida é a arte do encontro,
embora haja tanto desencontro pela vida."

Vinícius de Moraes (1981)

I would like to thank, first of all, my supervisor Kristian Pedersen, for his help in all matters and for his supervision through this work. He deserves a special thanks for introducing me to X-ray Astrophysics and for invaluable support since my early days in Denmark. Thanks also to Jens Hjorth for creating DARK, for being such a good leader, and for overall support. A big thanks go to Steen H. Hansen for his help during the final stages of this work and for making me write, to Marianne Vestergaard for the good advices and daily hugs, and to Michelle Cumming Løkkegaard for taking good care of all of us.

I would like to thank Steven W. Allen for my stay at Stanford University and for suggesting this project. Thanks to Norbert Werner for sharing his expertise on XMM-Newton data analysis and for contributing to making my stay in California so enjoyable.

Thanks to David Rapetti for performing his cosmological analysis on my results, to Johan Richard for extending his strong lensing model according to my needs and for the "surprise" proofreading, Radek Wojtak for the cross check of the mass profile models, and all members of the Dark Cosmology Centre for the discussions on mathematical methods and programming.

I am greatly indebted to Justyn Robert Maund for his willingness to help, honest comments, for proofreading this thesis and for his support. Thank you to Darach Watson for discussions on X-ray data analysis and to Anja C. Andersen for useful comments on chapter 4. Thanks to Brian Lindgren Jensen for all the IT support, and to Corinne Toulouse-Aastrup, Julie Meier Hansen and Sarah Pearson for the administrative matters.

I would like to thank all the members of the Dark Cosmology Centre, former and new, for creating such an inspiring environment where I experience collaboration and friendship. A special thanks goes to Daniele Malesani, my office mate Bo Milvang-Jensen, and former office mates Christa Gall, Thomas Greve and Andrew Zirm, for

their company throughout the several levels of struggle, and for tolerating me. Thanks to the "backyard squad" for the absolutely necessary breaks, to Stefan Geier for sharing his midnight pizza, and to the master students next door for some good laughs.

Over the past three years I had the chance of meeting amazing people, not all listed here. They all contributed in some way to what I have accomplished, and for that I am grateful.

Last but not least, I would like to express my deep appreciation and gratitude to those who are dearest to me and have been so neglected over the past year, for their love, understanding and patience.

Desiree Della Monica Ferreira

ABSTRACT

The gas mass fraction from X-ray observations of clusters of galaxies provides an independent method to constrain cosmological parameters. This thesis presents a study where the gas mass fraction of seven clusters of galaxies observed with XMM-Newton is measured. The selected clusters are hot, dynamically relaxed and span the redshift range z=0.14 to 0.89.

The cluster masses are derived under the assumptions of spherical symmetry and hydrostatic equilibrium, and the effects of assumptions on the distributions of the gas temperature, gas density and total gravitating mass are investigated. A model independent approach is adopted to compute the final mass results from spectral fitting alone.

Due to the good angular resolution of Chandra and its well-constrained background, previous studies of the gas mass fraction for constraining cosmology are largely based on Chandra observations. This work presents a complementary and independent study of galaxy clusters, where the gas mass fraction is obtained by using XMM-Newton data only. Background and PSF effects were both carefully considered.

In order to check for consistency and biases, the results from this analysis are compared with previous X-rays studies from Chandra and XMM-Newton observations, and optical studies of strong gravitational lensing.

The accuracy in the determination of the gas mass fraction is dependent on the uncertainties in the gas mass and total cluster mass measurements, and is also affected by the underlying assumptions adopted. The uncertainties derived from the model independent approach are more conservative, and are reduced by 40% on average if an NFW model is fit to the model independent mass profile, and by 75% if assuming an isothermal intra cluster gas.

The model independent measurements of the gas mass fractions are used to test the capability of XMM-Newton observations for constraining cosmology. The results obtained are consistent with previous results based on Chandra data and motivate the use of XMM-Newton to constrain cosmological parameters.

1

INTRODUCTION

"Interestingly, according to modern astronomers, space is finite.
This is a very comforting thought - particularly for people
who can never remember where they have left things."

Woody Allen (1935 -)

ABSTRACT – *This chapter provides a brief introduction to the study of clusters of galaxies as cosmological probes, the motivation for the study of the gas mass fraction and the work presented in this thesis.*

1.1 CLUSTERS OF GALAXIES

In the hierarchical scenario of structure formation, the collapse of primordial density perturbations results in the formation of small scale objects that then merge together to form the large scale structures (Press & Schechter 1974; White & Rees 1978) .

Clusters of galaxies are the largest structures in the Universe that have had time to undergo gravitational collapse and reach virial equilibrium. As structure grows hierarchically, clusters of galaxies are the most recently formed gravitationally relaxed systems. Among relaxed systems, they are the most massive, with masses ranging from $10^{13} M_{\odot}$ to over $10^{15} M_{\odot}$.

The majority of the mass in a galaxy cluster ($\approx 80\%$), is in the form of invisible non baryonic dark matter (Zwicky 1933, 1937; White et al. 1993). The remaining baryonic component is mostly in the form of a hot, diffuse, intra cluster gas, with small contribution from stars, dust and cold gas. The hot, low density, intra cluster gas accounts for approximately 85% of the baryons within galaxy clusters and is observed through its X-ray emission.

Galaxy clusters are particularly interesting for cosmology. The baryonic component trapped in the potential well of clusters carries information on the gravitational process involved in the formation of structures in the Universe. The measurements of the mass distribution on large scales, and the evolution of the growth of cosmic structures, place important constraints on cosmological models (Jenkins et al. 2001; Tinker et al. 2008;

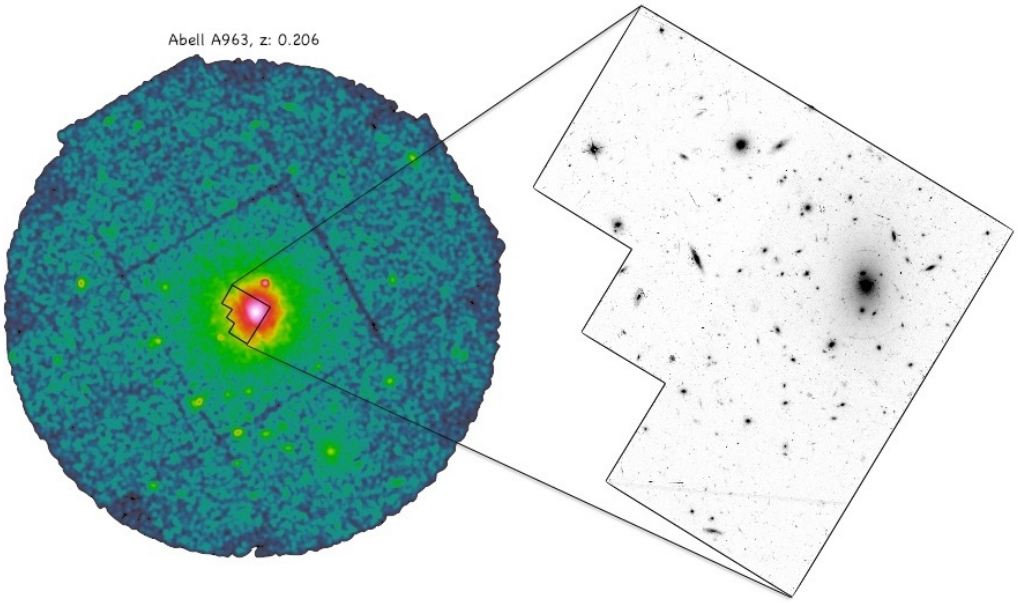

Figure 1.1: *The cluster Abell 963 at redshift 0.206 as seen in X-rays by XMM-Netwton (left) and in optical light by the Hubble Space Telescope (right).*

Kravtsov et al. 2006).

Theoretical predictions and observations indicate that the ratio between the gas mass and the total gravitating mass in the most massive, dynamically relaxed clusters, is a standard quantity. (e.g., Allen et al. 2008; White et al. 1993, and references therein). Based on this assumption, the study of the gas mass fraction in clusters can place strong constraints on cosmological parameters (e.g., Ettori et al. 2010, 2009; Allen et al. 2008, 2004, 2003; Fabian & Allen 2003; Ettori et al. 2003; Schindler 2002; Ettori & Fabian 1999; Schindler 1999).

1.2 CLUSTER OBSERVATIONS

By the end of the eighteenth century, Charles Messier and William Herschel had already identified concentrations of galaxies in what today are known as the Virgo and Coma clusters (see Biviano 2000). Nowadays observations of clusters of galaxies in optical, X-rays and microwaves complement each other, and are combined into making clusters a powerful cosmological tool.

Optical observations of galaxy clusters provide the determination of the luminosity of the galaxies belonging to the cluster, their velocity dispersion and the gravitational lensing effect, where light from background galaxies is distorted by the gravitational potential of a cluster in the line of sight.

The lensing effect a cluster of galaxies produces depends on the total distribution of

the mass of the cluster, therefore, the study of gravitational lensing provides a determination of the mass of the cluster in the line of sight and gives estimates of the amount of dark matter in it (e.g., Bartelmann & Schneider 2001; Hoekstra et al. 1998; Kaiser & Squires 1993; Tyson et al. 1998).

In 1937, Zwicky proposed that gravitational lensing could be applied to measure the mass of clusters of galaxies (Zwicky 1937). The first reference to the existence of large amounts of dark matter was also made by Zwicky while studying the dispersion in the radial velocity of the galaxies in the Coma galaxy cluster. Zwicky observed that the dispersion in the radial velocity of the galaxies was large and the gravity necessary to keep this cluster bond was far beyond that provided by the observed luminous matter (Zwicky 1933, 1937; Smith 1936). Later on, X-ray observatories revealed large amounts of gas in the intra cluster medium (e.g., Byram et al. 1966; Forman et al. 1972). However, that still couldn't account for the large gravitational potential necessary to keep the system bound.

The hot intra cluster gas makes galaxy clusters very bright X-ray sources. Observations of the X-ray emitting gas allow for the determination of the cluster overall X-ray luminosity, temperature, density and abundance of elements.

In a relaxed cluster, the intra cluster gas appears to be in hydrostatic equilibrium. For those systems, the gas temperature is closely related to their overall mass. Under the assumptions of spherical symmetry and hydrostatic equilibrium, the total cluster mass can be directly derived from the X-ray observables of clusters.

A more detailed introduction to X-ray observations and X-ray properties of galaxy clusters is given in chapter 2. The derivation of the gas mass and the total mass of clusters of galaxies is presented in chapter 6.

Hot gas in clusters of galaxies are also observed through its distortion effects on the cosmic microwave background. Sunyaev and Zeldovich predicted that hot gas in clusters of galaxies would produce a distortion in the blackbody spectrum, shifting some of the microwave photons to higher energies because of Compton scattering as photons pass through the hot intergalactic gas (Sunyaev & Zeldovich 1970, 1972). The photons acquire energy from the interaction with the electrons in the hot intra cluster gas, producing distortions in the signal detected from the microwave background in the direction of the clusters.

Figure 1.1 shows the cluster Abell 963 as seen in X-rays and optical light. The Sunyaev-Zeldovich effect and the gravitational lensing effect are illustrated in figure 1.2.

1.3 COSMOLOGICAL CONTEXT

Cosmology is the study of the large scale Universe. On large scales, gravity is the dominant force. Einstein's theory of general relativity views gravity as a manifestation

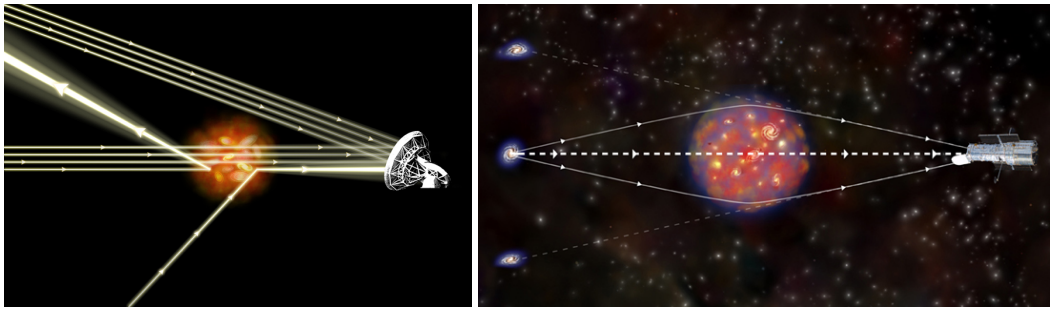

Figure 1.2: *Illustration of the Sunyaev-Zeldovich effect where the the signal from the cosmic microwave background is distorted in the direction of the clusters (left). Strong gravitational lensing effect (right) where the light from a background galaxy is bended by a massive object, such as a galaxy cluster, producing fake lensed images of the original galaxy. (Illustrations: NASA/CXC/M.Weiss) .*

of the curvature of space-time. The presence of mass-energy curves space-time, and the curvature of space-time dictates how mass-energy moves. A brief introduction to the most relevant cosmological information is listed below. Discussion on the underlying assumptions is found in Peebles & Ratra (2003).

The Friedmann equation,

$$H^2\left(t\right) = \left(\frac{\dot{a}}{a}\right)^2 = \frac{8\pi G}{3}\rho\left(t\right) - \frac{\kappa}{R_0^2 a\left(t\right)^2} \quad , \tag{1.1}$$

and the fluid equation,

$$\dot{\rho} + 3\left(\frac{\dot{a}}{a}\right)\left(\rho + P\right) = 0 \quad . \tag{1.2}$$

relate the scale factor $a(t)$, the energy density, $\rho(t)$, and pressure $P(t)$ of the contents of the Universe. Equations 1.1 and 1.2 are derived from Einstein's field equations for a homogeneous and isotropic Universe. They describe the dynamics of the Universe and relate the rate of change in the total energy to the work done by the pressure as the Universe expands. In equation 1.1, H is the Hubble parameter, G is the gravitation constant, κ describes the curvature of the Universe and R_0 is the radius of curvature at the present time.

The equation of state, $P = \omega\rho$, relates the pressure P and the energy density ρ. The parameter ω is a dimensionless number and its value depends on the component it describes. The equation of state of non-relativistic matter has $\omega = 0$, $\omega = 1/3$ for radiation, and $\omega \leq -1/3$ for the dark energy in an accelerating Universe.

The scale factor of the Universe a in equations 1.1 and 1.2 is related to the redshift z according to,

$$1 + z = \frac{\lambda_{obs}}{\lambda_{em}} = \frac{a(t_{obs})}{a(t_{em})} \quad , \tag{1.3}$$

where λ_{obs} is the observed wavelength of a spectral feature that had wavelength λ_{em} at the time of emission.

As a function of the scale factor, the energy density of a Universe component with a the equation of state parameter ω is given by

$$\rho(a) = \rho_0 a^{-3(1+\omega)} \quad . \tag{1.4}$$

The dimensionless density parameter is defined as

$$\Omega = \frac{\rho}{\rho_c} \quad , \tag{1.5}$$

where $\rho_c\,(t)$ is the critical density of the Universe given by,

$$\rho_c\,(z) = \frac{3}{8\pi G} H\,(z)^2 \quad . \tag{1.6}$$

Making use of all equations above, the Friedmann equation can be written in terms of the dimensionless density parameter and redshift,

$$H^2\,(z) = H_0^2 E(z) \quad , \tag{1.7}$$

where

$$E(z) = \left[\Omega_r(1+z)^4 + \Omega_m(1+z)^3 + \Omega_\Lambda(1+z)^{2(1+\omega_\Lambda)} + \Omega_\kappa(1+z)^2\right]^{1/2} \quad . \tag{1.8}$$

In equation 1.7, H_0 is the Hubble parameter at the present time. The parameters Ω_r, Ω_m, Ω_Λ and Ω_κ in equation 1.8 are the density parameter for radiation, matter, dark energy and curvature, respectively.

The current cosmological paradigm, Lambda Cold Dark Matter (ΛCDM), is the simplest known model for the Universe that is in agreement with the available cosmological observational data (e.g., Bennett et al. 2003; Spergel et al. 2007; Komatsu et al. 2010). In the ΛCDM model, the Universe is homogeneous and isotropic at large scales and spatially flat ($\Omega = 1$). It contains radiation, baryonic and non baryonic matter, and a cosmological constant, Λ (Spergel et al. 2007).

The model has six parameters, which are enough to predict not only the statistical properties of the microwave sky but also the large scale distributions of matter and galaxies. The parameters are: the matter density ($\Omega_m h^2$), baryon density ($\Omega_b h^2$), Hubble constant (H_0), amplitude of fluctuations (σ_8), optical depth (τ), and a slope for the scalar perturbation spectrum (n_s) (see Spergel et al. 2007).

At the present time, the two dominant components of the Universe are believed to be a form of non baryonic dark matter and dark energy. The dark matter gravity is responsible for the formation of structure, while dark energy is responsible for the accelerated expansion of the Universe.

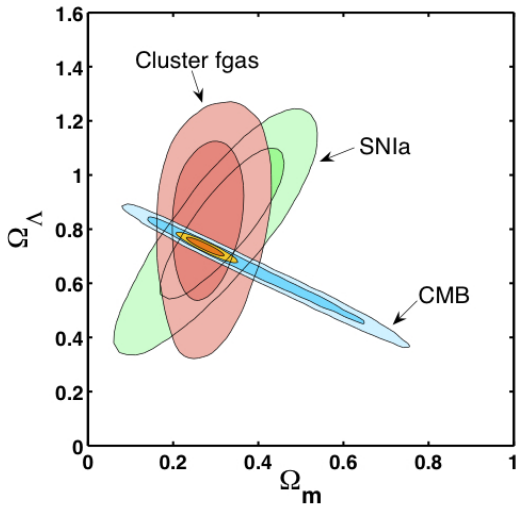

Figure 1.3: *Cosmological constraints reported by Allen et al. (2008) showing the 1 and 2σ confidence constraints in the Ω_m, Ω_Λ plane for the Chandra f_{gas} data (red contours). Results obtained from CMB data (blue contours) and SNIa data (green contours) by Davis et al. (2007). Figure from (Allen et al. 2008).*

1.4 THE GAS MASS FRACTION

The gas mass fraction (f_{gas}) is the ratio between the mass of the hot gas M_{gas} trapped in the gravitational potential of a galaxy cluster and the total gravitating mass of the cluster M_T within a defined radius R.

$$f_{gas}(R) = \frac{M_{gas}(< R)}{M_T(< R)} \tag{1.9}$$

Both the gas mass and the total mass of galaxy cluster can be obtained through X-ray observations (see chapter 6).

The total cluster mass, M_T in equation 1.9, includes gas, dark matter, stars; anything that contributes to the gravitational potential of the cluster.

The baryonic content of the largest galaxy clusters is expected to be representative of the cosmic baryon fraction, $\Omega_b/\ \Omega_m$ (White et al. 1993). The gas mass fraction can be used as a cosmological probe based on the assumption that this quantity is constant for a given cluster radius, and being a standard measure, should be invariant with redshift (Sasaki 1996; Pen 1997).

The stellar masses in clusters correspond to approximately 15% of the total baryon budget. The determination of stellar masses from optical and near infrared observations, combined with the values of baryon density Ω_b (Burles et al. 2001; Spergel et al. 2007) and the Hubble constant H_0 (e.g., Freedman et al. 2001; Spergel et al. 2007) allow for the determination of the density parameter of matter in the Universe Ω_m, based on the assumption that the ratio between baryonic and total matter in galaxy clusters closely match the cosmic baryon fraction, $\Omega_b/\ \Omega_m$.

The study of the gas mass fraction as a function of redshift can also probe the acceleration of the Universe. This use of the gas mass fraction is primarily geometric. To derive both the mass of the gas and the total mass in galaxy clusters it is necessary to make use of the angular diameter distance, d_A.

$$d_A = \frac{c}{H_0(1+z)\sqrt{\Omega_\kappa}} \sinh\left(\sqrt{\Omega_\kappa}\int_0^z \frac{dz}{E(z)}\right) \quad , \quad \Omega_\kappa > 0 \tag{1.10}$$

$$d_A = \frac{c}{H_0(1+z)} \int_0^z \frac{dz}{E(z)} \quad , \quad \Omega_\kappa = 0 \tag{1.11}$$

$$d_A = \frac{c}{H_0(1+z)\sqrt{\Omega_\kappa}} \sin\left(\sqrt{\Omega_\kappa}\int_0^z \frac{dz}{E(z)}\right) \quad , \quad \Omega_\kappa < 0 \tag{1.12}$$

The gas mass fraction is dependent on the cosmology assumed for computing the angular diameter distance using equations 1.10-1.12,

$$f_{gas} = \frac{M_{gas}}{M_T} \propto \frac{S_X^{1/2}\theta_c^{3/2}d_A^{5/2}}{\theta_c d_A} \propto d_A(z, \Omega_m, \Omega_\Lambda, w)^{3/2} \quad , \tag{1.13}$$

where S_X is the X-ray flux and θ_c is the angular radius of the galaxy cluster at which the gas mass fraction is measured (see e.g., Ettori et al. 2003).

The latest results on cosmological constraints from X-ray gas mass fractions make use of large sample of clusters (≈50) over a wide redshift range ($z = 0 - 1.3$) (Ettori et al. 2009; Allen et al. 2008).

1.5 THIS THESIS

The use of clusters of galaxies for cosmology requires precise measurements of cluster observables. Limitations on the application of results derived from the study of galaxy clusters to constrain cosmological parameters lies on biases in the observational studies, limited accuracy of measurements and inaccuracy of theoretical models, which may not be capable of truly describing the complex physical processes within the cluster's potential.

To confront theoretical predictions with observations, and cross check between the use of different instruments and methods, is of extreme importance to achieve the necessary confidence in clusters determinations of cosmology.

The superior spatial resolution of Chandra and well constrained background allow for derivation of the gas mass fraction in galaxy clusters to high precision. To use XMM-Newton observations it is necessary to address two main issues: 1) proper background subtraction; and 2) the possible effect of the PSF. If there are no biases or systematic effects, the results from XMM-Newton should be able to reproduce, at least to the same quality, the results from Chandra.

An independent study of clusters of galaxies observed by XMM-Newton is presented in this thesis, where the gas mass fraction measurement of a sample of seven galaxy clusters is performed. All objects are hot ($T \gtrsim 5$ keV) and present regular X-ray morphology. The selected targets are Abell 1413, Abell 963, Abell 2390, Abell 1835, MS2137.3-2353, MACSJ0744.9+3927 and ClJ1226.9+3332, covering a redshift range from z=0.143 to z=0.89.

The data reduction and analysis of XMM-Newton observations of the clusters in this study was performed such that background and PSF effects were both carefully considered.

The cluster masses are derived under the assumptions of spherical symmetry and hydrostatic equilibrium. The effects of parametrizations or assumptions on the distributions of the gas temperature, gas density and total gravitating mass are investigated. A model independent approach is adopted to compute the final mass results from spectral fitting only.

Throughout this work, a standard ΛCDM cosmology is adopted, with $\Omega_\Lambda = 0.70$, $\Omega_M = 0.30$, and $H_0 = 70\,\mathrm{km\,s^{-1}\,Mpc^{-1}}$. Unless otherwise stated, quoted uncertainties are considered at 68% confidence level.

2

X-RAY OBSERVATIONS

"L'essentiel est invisible pour les yeux."

Antoine de Saint-Exupery, Le Petit Prince (1943)

ABSTRACT – *The aim of this chapter is to provide a brief introduction to X-ray observations, the features that galaxy clusters present in X-rays, a short description of the XMM-Newton Observatory and the tools used for the analysis of XMM-Newton observations.*

2.1 INTRODUCTION

X-rays are a form of electromagnetic radiation with wavelength in the range of 0.01 to 10 nanometers, corresponding to energies between 0.12 keV and 120 keV. According to the energy level, X-rays are referred to as being either soft, with energies up to 10 keV, or hard, with energies between 10 keV and 120 keV.

Thermal X-ray emission is observed from astronomical sources hosting gas at temperatures of the order 10^7 K. Non thermal X-ray emission from astronomical sources occurs through synchrotron radiation, when relativistic charged particles travel through magnetic fields.

X-rays are absorbed by the Earth's atmosphere, therefore X-ray observations are only possible at very high altitudes, onboard rockets, balloons, and satellites.

The first X-ray observations of the Sun happened in 1949 using a detector placed in a sounding rocket launched above the atmosphere (Friedman et al. 1951). In 1962, a rocket carrying X-ray detectors observed the first X-rays from an extra solar source (Giacconi et al. 1962, 1964).

Since the first observations of astronomical X-ray sources, the technology behind X-ray telescopes has developed enormously allowing for the study of the high energy Universe. The possibility to observe astronomical objects in X-rays has had a profound significance for all astronomy.

The studies of X-ray emission from celestial objects revealed that the high energy phenomena play a fundamental role in astronomical structures on all scales (Giacconi 2003).

In the early 70's, the space mission UHURU observed the diffuse X-ray emission from many galaxy clusters (e.g., Kellogg et al. 1971; Forman et al. 1972). The observation of X-ray emission from the gas in clusters of galaxies showed that most of the baryonic component in clusters is in the form of a high temperature plasma, which has consequences not only for the understanding of clusters in general but also for cosmology. Among other things, the discovery of X-ray emission in clusters is used today to investigate the formation and evolution of structures in the Universe (see e.g., Golwala et al. 2009; Kravtsov et al. 2009; Vikhlinin et al. 2009).

2.2 X-RAYS FROM GALAXY CLUSTERS

X-ray emission is observed from the hot, low density gas in the intra-cluster medium. The X-rays from galaxy clusters are primally due to thermal emission from diffuse hot gas within the intra-cluster medium.

The continuum part of the X-ray spectrum is mainly due to thermal bremsstrahlung (free-free) emission with contributions from recombination radiation (free-bound emission) and two photon decay (bound-bound emission).

Free-free emission is produced by the acceleration of electrons when deflected by another charged particle. The radiation is created by charged particles that are free both before and after the acceleration. Free-bound emission is produced when a free electron is captured by an ion while emitting a photon.

Bound-bound emission occurs when an electron from a bound 1s shell is excited to the 2s shell after a collision with a free electron. The decay of a 2s electron back to the 1s orbit, by a radiative transition, is forbidden by quantum mechanical selection rules. In a common case, the ion would be excited to a higher level by another collision, and it would be able to decay radiatively back to the 1s ground state.

In cases of very low densities, such as in the very tenuous gas in galaxy clusters, with densities of 10^{-5} to $10^{-1}\ \mathrm{cm}^{-3}$ (see e.g., Böhringer & Werner 2010), the probability for a second collision is very small, therefore, two photon emission can occur. The electron decays from the 2s orbit to the 1s orbit while emitting two photons. (see e.g., Kaastra et al. 2008).

Other than the continuum emission, line radiation is also present in the X-ray spectrum of galaxy clusters, of which the Iron (Fe) complex emission lines between 6.5 keV and 7 keV are the strongest. The X-ray spectrum of the cluster Abell 963 is shown in figure 2.1.

An atom or ion must first be brought into an excited state before it can emit line photons. Several processes can bring a ion into an excited state, in galaxy clusters this

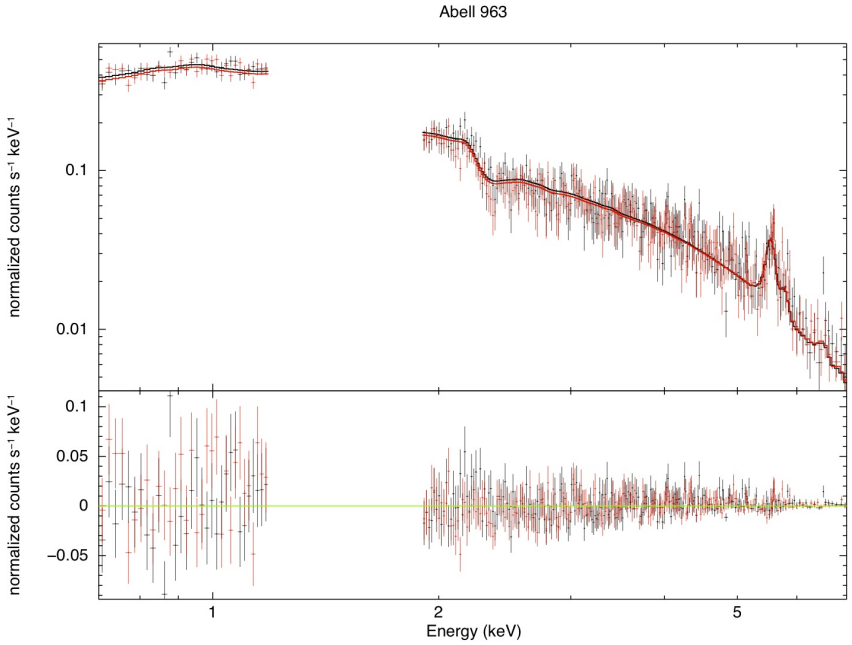

Figure 2.1: *X-ray spectrum between 0.7 keV and 7 keV from the galaxy cluster Abell 963 at redshift 0.206. The spectrum presents continuum emission with the Fe line complex at this redshift visible around 5-6 keV.*

happens through bound-bound emission. An ion in such a state may decay back to a lower energy level by emitting a photon. The decay energy is characteristic for each atom/ion and so is the emission line produced.

In addition to the 7 keV Fe line complex, the X-ray spectrum of a low density plasma, contains a large number of lower energy lines (Sarazin 1988). Figure 2.2 shows an example of the emission lines in the X-ray spectrum of galaxy clusters.

The emission processes discussed above result in a X-ray emissivity that is proportional to the ion and electron densities.

$$\epsilon_\nu = \sum_{X,i} \Lambda_\nu(X^i, T_g) n(X^i) n_e \tag{2.1}$$

In equation 2.1, ϵ_ν is the emissivity at a given frequency ν, X^i is a given ion, Λ is the emission per ion at unit electron density and it is dependent on the gas temperature T_g, $n(X^i)$ is the density of the ion X^i and n_e is the electron density.

The shape of the resulting spectrum depends on the gas temperature and its chemical abundances. The normalization of the spectrum, which reflects the X-ray luminosity, is set by the emission integral EI (Sarazin 1988).

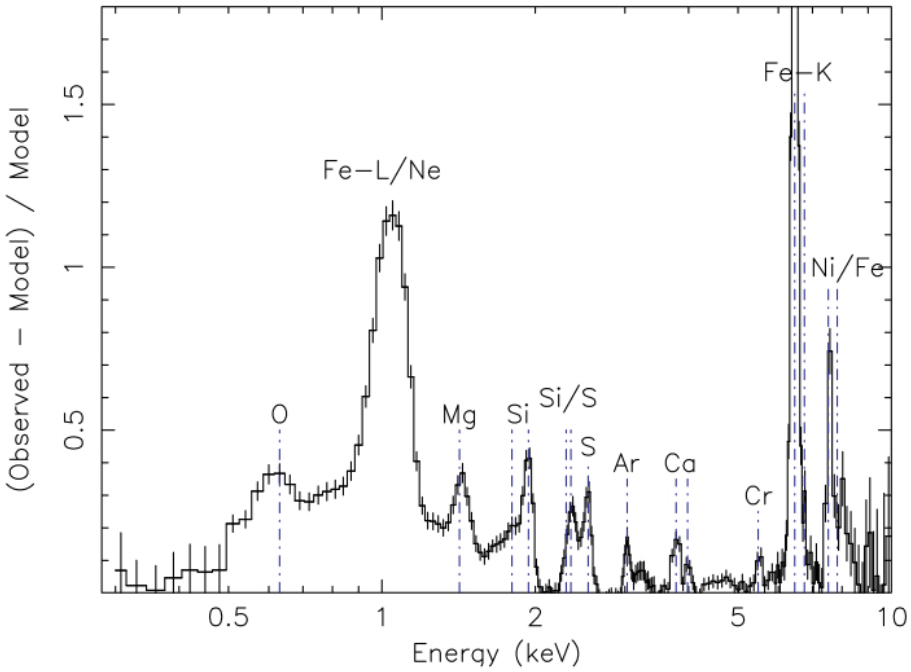

Figure 2.2: *Identification of emission lines in a galaxy cluster spectrum. The line spectrum of the cluster 2A 0335+096, as observed with XMM-Newton EPIC [from Werner et al. (2006)].*

$$EI = \int n_p n_e dV \tag{2.2}$$

Equation 2.2 defines the emission integral EI, where n_p is the proton number density, n_e is the electron number density, and V is the volume of the gas in the cluster.

For the interested reader, an extensive description of the X-ray emission mechanisms in galaxy cluster can be found in "X-ray Emission from Clusters of Galaxies" by Craig L. Sarazin (Sarazin 1988).

2.3 X-RAY OBSERVATORIES

During the 1960's, X-ray observations were made through rocket flights. Each launch would result in about five minutes of X-ray observations above an altitude of 100 km and the total amount of time which was available for observation during the whole decade was about one hour.

UHURU, launched in 1970, was the first observatory onboard of a satellite entirely dedicated to X-ray astronomy, followed by several other X-ray missions. Among other discoveries, UHURU made possible the detection of the X-ray emission from clusters of galaxies (e.g., Forman et al. 1972).

In 1979 a fully instrumented X-ray telescope suitable for the detection and study of all types of X-ray sources was launched. The Einstein satellite was the first with

focusing optics and a true imaging X-ray telescope. Its substantial technical improvement over the previous X-ray missions, made possible the detection of all types of X-ray sources (Giacconi 1980).

Since the launch of the Einstein satellite, many X-ray missions contributed to our understanding of the high energy Universe, e.g. ROSAT, ASCA observatory, EXOSAT, and BeppoSAX. These, however, are no longer in operation.

X-ray telescopes onboard of satellites which are in use at the time of writing include the XMM-Newton observatory, the INTEGRAL satellite, the Rossi X-ray Timing Explorer (RXTE), the Swift X-Ray Telescope (XRT), Chandra observatory and Suzaku (despite its failed spectrometer), among other smaller missions carrying X-ray detectors.

The two satellite X-ray observatories of particular relevance for the study presented in this thesis are the ESA mission, XMM-Newton, and the NASA mission, Chandra. The two observatories are complementary. Chandra has superior spatial resolution and contains one telescope, while XMM-Newton has superior collecting area and contains three telescopes. These modern X-ray observatories use CCD detectors that are able to read out the position and energy of individual X-ray photons. The X-rays are collected by mirror modules, which are grazing-incident telescopes, and focused in the focal plane equipped with CCD cameras (see e.g., Jansen & XMM Science Operations Team 2000; Tomlin 1999).

Modern X-ray observatories have had a tremendous impact on the study of galaxy clusters. Today it is possible to map the gas distribution in clusters in detail, as well as derive temperature and mass profiles.

The study of such systems has been extended to redshifts higher than one, and the search and identification of new clusters keeps revealing exciting results.

The next generation of X-ray observatories will be composed of several missions. The Spectrum-Roentgen-Gamma (SRG) satellite, the Nuclear Spectroscopic Telescope Array (NuSTAR), Astro-H, and the International X-ray Observatory (IXO), to name a few.

The SRG is a Russian/German mission carrying eROSITA (extended Roentgen Survey with an Imaging Telescope Array) onboard. eROSITA will perform the first imaging all-sky survey in the X-ray energy range up to 10 keV with unprecedented spectral and angular resolution (Predehl et al. 2007).

NuSTAR is a NASA mission planned for launch in 2012. NuSTAR will be the first focusing hard X-ray mission and will allow X-ray imaging in the energy range between 6 keV and 79 keV (Harrison et al. 2010).

Astro-H is a Japanese mission with NASA participation and is planned for launch in 2013. Astro-H will provide high resolution spectroscopy and imaging up to 10 keV, and hard X-ray imaging spectroscopy up to 80 keV (Takahashi et al. 2010).

The International X-ray Observatory (IXO) is a joint ESA/JAXA/NASA mission

and is planned for launch in 2021. IXO is planned to have improved instrumental capabilities in X-ray observations far beyond the current generation of X-ray missions. The IXO design will provide up to 100-fold increase in effective area for high resolution spectroscopy between 0.3 keV and 10 keV, deep spectral imaging from 0.3 keV to 40 keV over a wide field of view, microsecond spectroscopic timing with high count rate capability, and high sensitivity, imaging polarimetry (Bookbinder 2010).

2.3.1 XMM-Newton vs Chandra

The XMM-Newton and Chandra observatories are complementary. Chandra, the NASA mission, has better spatial resolution, producing highly resolved images, while XMM-Newton, the European mission, has a larger collecting area and higher spectral resolution.

Chandra contains one telescope and XMM-Newton carries three telescopes. The main difference in instrument operation between XMM-Newton and Chandra is that on XMM-Newton all instruments operate simultaneously, while on Chandra they are alternated.

The study of galaxy clusters included in this thesis uses XMM-Newton data only and the results obtained are compared to the previous studies by several authors carried out using Chandra data.

2.4 XMM-Newton

XMM-Newton is an X-ray observatory satellite named in honor of Sir Isaac Newton. XMM stands for X-ray Multi Mirror. It is a mission developed by the European Space Agency (ESA), dedicated to exploring the Universe in the soft-X-ray part of the electromagnetic spectrum, between 0.2 and 12keV (XMM Users Handbook 2010).

The XMM-Newton ESA mission was launched on December 10th, 1999. It weighs 3800 kg and is 10 m long. It is placed in a 48 hour elliptical orbit at 40 degrees. Its apogee is about 114000 km from Earth and its perigee about 7000 km (XMM Users Handbook 2010). The diagram of the XMM-Newton orbit is shown if figure 2.3.

XMM-Newton carries two distinct types of telescopes, an X-ray telescope and an optical/UV telescope. Three types of instruments are onboard the satellite:

1. The European Photon Imaging Camera (EPIC), for X-ray imaging, X-ray spectroscopy and photometry.

2. The Reflection Grating Spectrometer (RGS), for high-resolution X-ray spectroscopy and spectro-photometry.

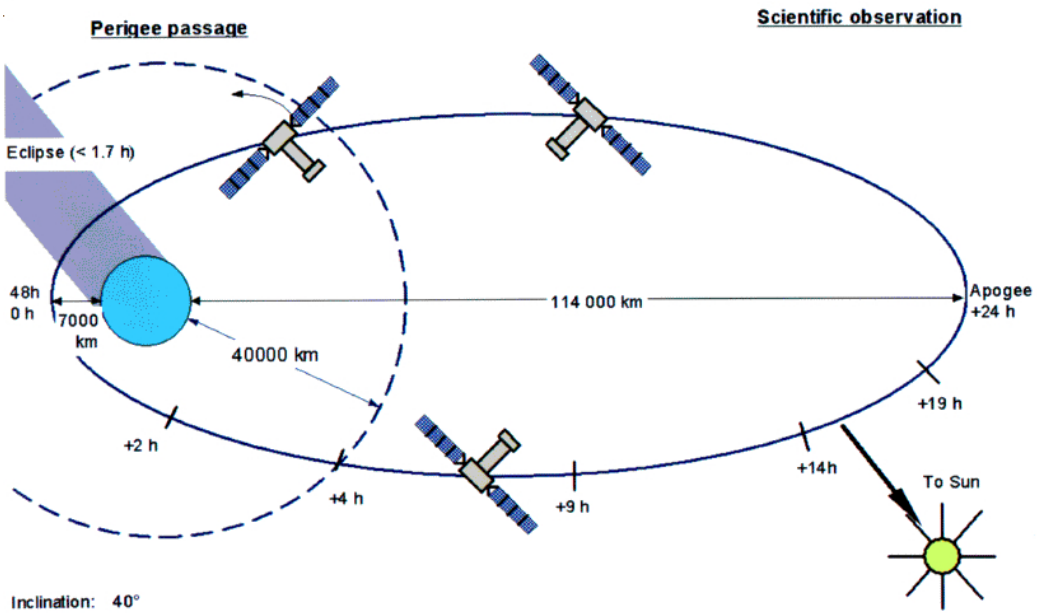

Figure 2.3: *Diagram of the XMM-Newton orbit. Image from VILSPA XMM-Newton Science Operations Center, Dornier Satellitensysteme GmbH.*

3. The Optical Monitor (OM), for optical/UV imaging and spectroscopy.

The arrangement of the telescopes and instruments in the XMM-Newton spacecraft is shown in figure 2.4.

The basic characteristics of XMM-Newton are: simultaneous operation of all science instruments; high sensitivity; good angular resolution; moderate and high spectral resolution; simultaneous optical/UV observations; and long continuous target visibility. A detailed description of the XMM-Newton mission can be found in XMM Users Handbook (2010).

The XMM-Newton observatory has three telescopes for collecting X-ray photons. The optics of each telescope consist of 58 nested mirror modules. They are designed to operate in the X-ray energy range of 0.1 keV to 12.0 keV, with a focal length of 7.5m, and X-ray point-spread function values for the full width at half maximum ($FWHM$) on the order of 6 arc seconds and the half energy width (HEW) of about 15 arc seconds.

Each mirror module consists of two parts. The front part has a paraboloid surface and the rear part a hyperboloid surface. This configuration allows for double reflection of the grazing X-rays, and therefore, focussing of X-rays. Behind each of the X-ray telescopes an EPIC camera is installed, providing extremely sensitive imaging observations.

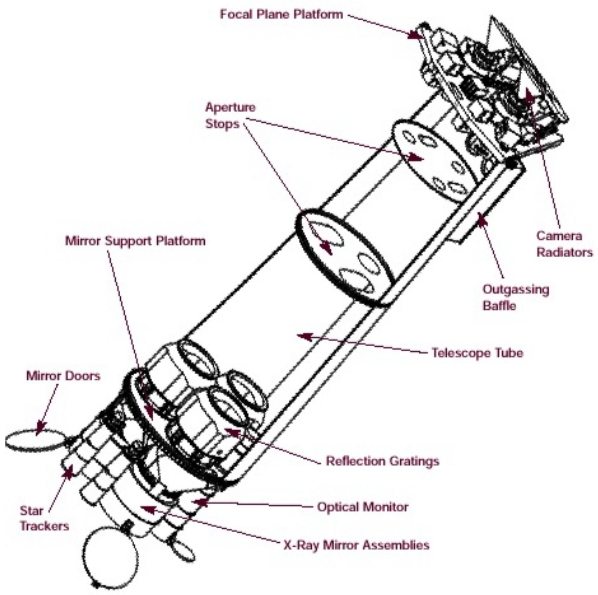

Figure 2.4: *Diagram of the XMM-Newton spacecraft. Image from ESA.*

Figures 2.5 and 2.6 show the optical concept of the XMM-Newton mirror modules.

2.4.1 EPIC CAMERAS

The XMM-Newton telescope carries three EPIC cameras of two different types: 1) MOS (Metal Oxide Semi-conductor) CCD arrays type, and 2) fully depleted pn CCDs (see XMM Users Handbook 2010).

Two of the cameras are EPIC MOS CCDs, with the Reflection Grating Spectrometer (RGS) in the light path. The third X-ray telescope has an unobstructed beam with an EPIC camera at the focus, using pn CCDs.

Each camera has a field of view (FOV) of 30 arc minutes. The cameras allow several modes of data acquisition, and different cameras may operate in different modes. The MOS and pn cameras are fundamentally different. They have different geometries and differ in others properties as well, such as their readout time. Figure 2.7 illustrates the layout of the two types of cameras.

All EPIC CCDs operate in a photon counting mode, producing so called "event lists". An event is an X-ray hitting the detector. An event list is a table with the event's attributes, such as position, time and energy, among others.

EPIC cameras are not only sensitive to X-ray photons but also to infrared, visible and ultra-violet light. The cameras include blocking filters to reduce the contamination of the X-ray signal by those photons.

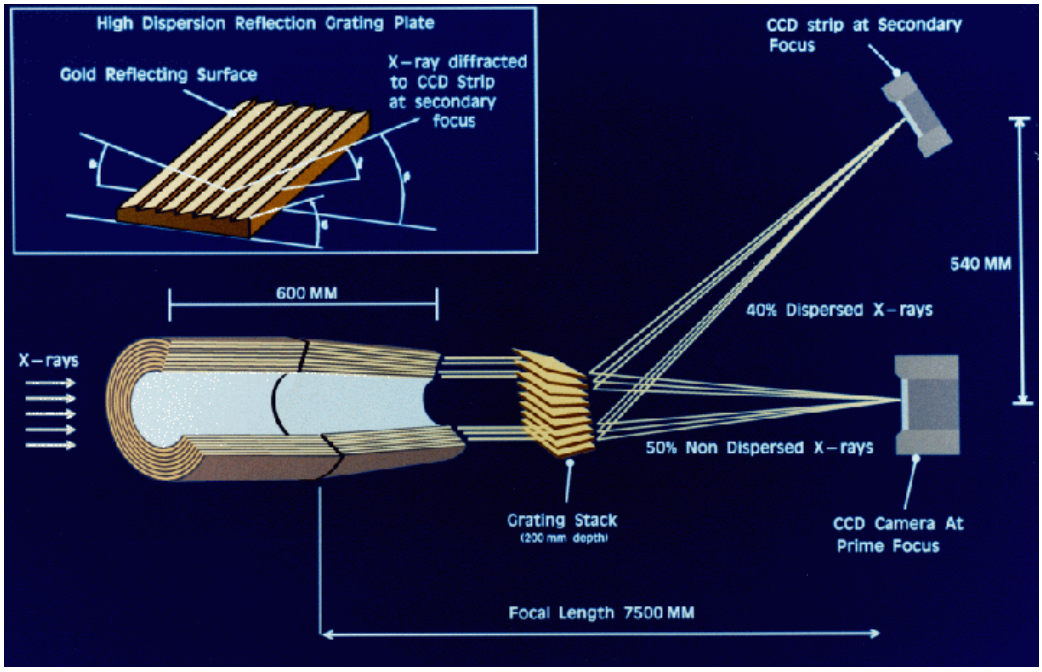

Figure 2.5: *Schematic light path for the two XMM-Newton telescopes in which a Reflection Grating Array (RGA) is mounted into the optical path. Image from ESA.*

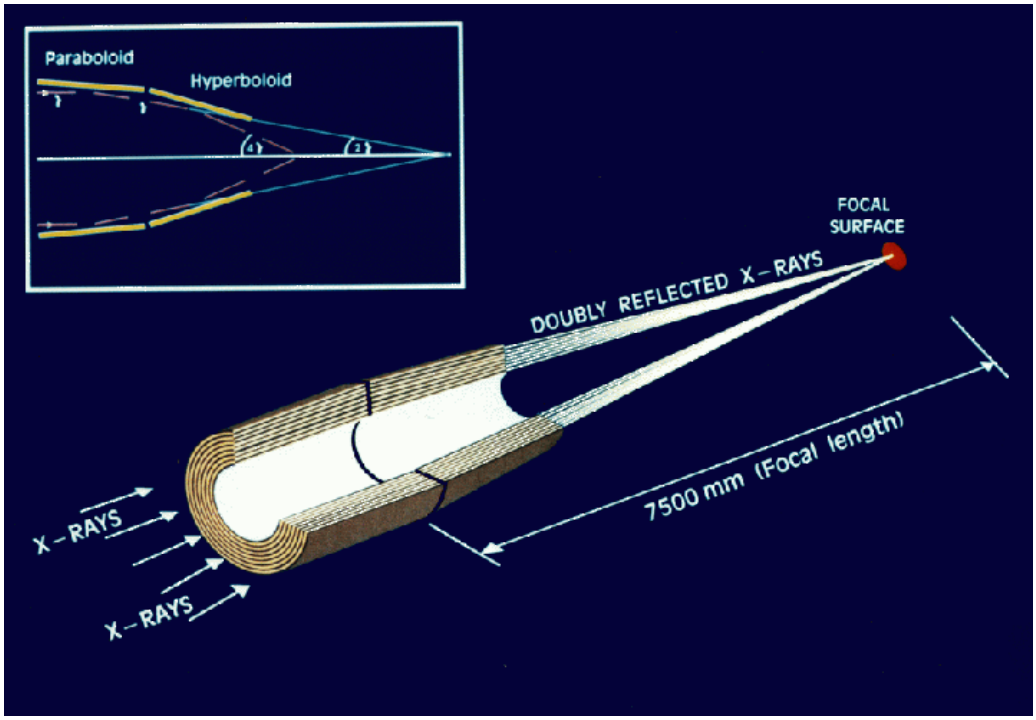

Figure 2.6: *The unobstructed light path in the XMM-Newton telescope with an EPIC pn camera in its primary focus. Image from ESA.*

2.4.2 EPIC BACKGROUND

The EPIC cameras are affected by different sources of background. Chapter 4 describes the treatment of the X-ray background affecting the XMM-Newton observations used in this study.

The background effect in the detectors can be divided in to three categories: 1) the cosmic X-ray background, 2) the particle X-ray background, and 3) the instrumental background. (see XMM Users Handbook 2010)

The cosmic X-ray background consists of photons from astrophysical sources and is dominated by thermal emission at lower energies (< 1 keV) and a power law at higher energies (primarily from unresolved cosmological sources). This background varies over the sky at lower energies. Solar wind charge exchange can also contribute to the cosmic X-ray background.

The particle X-ray background consists of soft proton flares from the Sun, with spectral variations from flare to flare, and internal (cosmic-ray induced) background, created directly by particles penetrating the CCDs, and indirectly by the fluorescence of satellite material to which the detectors are exposed.

The instrumental background consists of electronic noise, it is a detector noise component, such as bright pixels and readout noise.

The data reduction and analysis of XMM-Newton observations carried out in this study considered carefully the effect of the different background components.

2.5 ANALYSIS OF XMM-NEWTON DATA

The XMM-Newton scientific data is organized in the Observation Data Files (ODF) and Slew Data Files (SDF), most of these files have a FITS format. The ODF/SDF files contain uncalibrated files. To perform scientific analysis of XMM-Newton data, specific XMM-Newton data reduction and analysis software are available.

The procedures applied to the data reduction and analysis of XMM-Newton observations performed in this study are described in chapter 3, and chapters 4 and 5, respectively.

2.5.1 SAS

The Science Analysis System (SAS) is a collection of tasks, scripts and libraries, specifically designed to reduce and analyze data collected by the XMM-Newton observatory. SAS is necessary to extract standard and/or customized science products, such as spectra, images, light curves.

The latest version of SAS available at the time of writing and applied in this study is the SAS v.10.0.0.

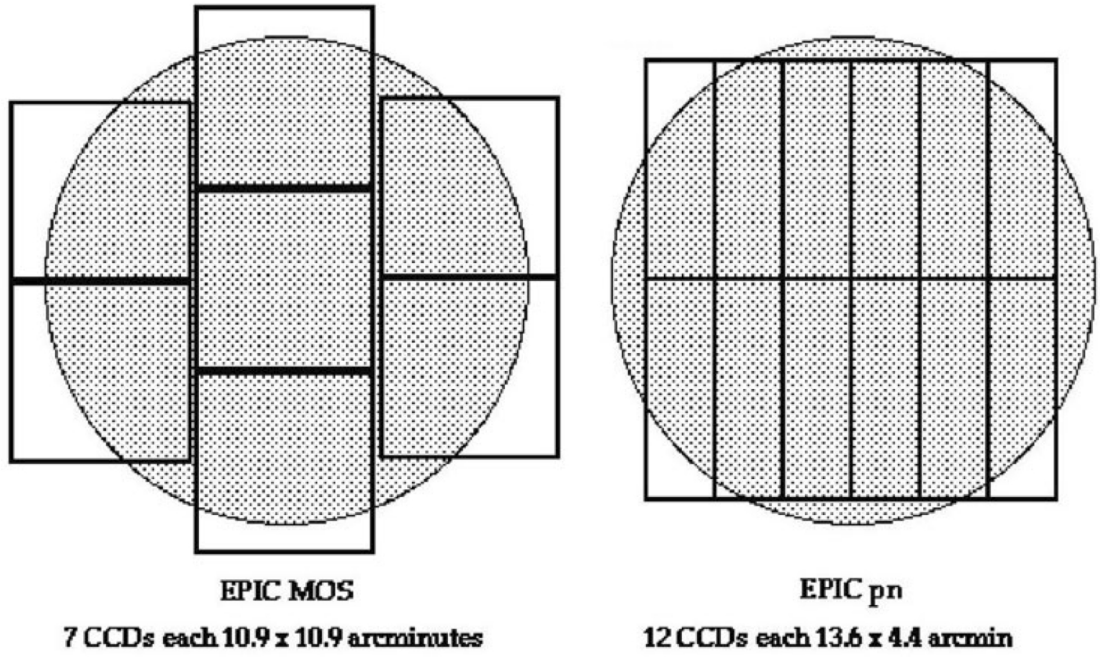

Figure 2.7: *Layout of the MOS and pn EPIC cameras. Image from XMM-Newton User's Hand Book .*

2.5.2 XMM-ESAS

To study X-ray emission from extended sources such as a galaxy cluster, the XMM-Newton Extended Source Analysis Software package (XMM-ESAS) is available (Snowden et al. 2010).

XMM-ESAS is based on the methods described in Snowden et al. (2008).

XMM-ESAS used to be a separate software package, but it is now integrated in SAS. At the time of writing, XMM-ESAS is available for the analysis of the EPIC MOS camera only. The extended version including methods for the pn detectors is expected soon.

With XMM-ESAS it is possible to model the quiescent particle background for both spectral and spatial analysis of EPIC MOS observations. It allows for the production of background spectra and images that are used in the treatment of the X-ray background affecting the EPIC MOS cameras.

The use of XMM-ESAS for the present work is described in chapter 3.

2.5.3 XSPEC

The X-ray spectral fitting program, XSPEC (Arnaud 1996), is used to perform analysis of the spectral products obtained by using the XMM-Newton specific software SAS and XMM-ESAS.

XSPEC is a command-driven, interactive, X-ray spectral-fitting program, designed

to be detector independent so that it can be used for any spectrometer.

The spectral analysis in this work was performed with XSPEC version 12.5, and is described in chapter 5.

3

SAMPLE SELECTION AND DATA PROCESSING

"Mama always said life was like a box of chocolates.
You never know what you're gonna get."

Forrest Gump (1994)

ABSTRACT – *The aim of this chapter is to introduce the sample of clusters and the criteria considered for the sample selection. The steps of data reduction are described and the final data products, used later for the data analysis, are presented.*

3.1 THE CLUSTER SAMPLE

The selection of the galaxy clusters used in this study is based on several criteria.

One of the goals of this study is to derive the clusters' total masses under the assumption that the systems are in hydrostatic equilibrium. This assumption is only valid for relaxed clusters. The true dynamical condition of the clusters is unknown and the selection is based on the overall X-ray morphology. The clusters should, therefore, be dynamically relaxed, not presenting strong indication of disturbance.

Previous studies (Bialek et al. 2001; Muanwong et al. 2002; Ettori et al. 2004; Kravtsov et al. 2005; Vikhlinin et al. 2006) have shown that cooler galaxy clusters and groups present a larger scatter in the measurements of the ratio between the gas mass and the total mass of clusters. To avoid introducing scatter in the measurement of the gas mass fraction, hot clusters, with average temperature $\gtrsim 5$ keV were selected.

To study the application of galaxy clusters as cosmological probes it is necessary to compare observations at different redshifts to understand how the properties of the Universe affect our view of these systems, therefore the clusters in this sample are distributed in a wide redshift range ($z = 0.14 - 0.89$).

The observations of the clusters selected should have enough X-ray detection to allow for the production of a temperature profile containing at least a few bins. Particularly for systems at high redshift the duration of exposure is a strong constraint. The

Cluster	Redshift	ObsID	Exposure time (ks)	R.A. (J2000)	DEC. (J2000)
Abell 1413	0.143	0502690201	82.448	11 55 18.1	23 24 17
Abell 963	0.206	0084230701	27.461	10 17 03.8	39 02 49
Abell 2390	0.230	0111270101	23.105	21 53 36.8	17 41 44
Abell 1835	0.325	0551830201	120.870	14 01 01.9	02 52 43
MS2137.3-2353	0.313	0008830101	22.621	21 40 15.2	-23 39 40
MACSJ0744.9+3927	0.686	0551851201	98.286	07 44 52.9	39 27 27
ClJ1226.9+3332	0.890	0200340101	98.829	12 26 58.1	33 32 47

Table 3.1: *Overview of the selected cluster sample observed by XMM-Newton.*

choice of systems is based on availability of good quality data in the XMM-Newton archive.

To check for consistency with previous studies and biases, the selected systems are a subsample of the 42 galaxy clusters analyzed and reported by Allen et al. (2008) using data from the Chandra observatory. Throughout this study we carefully compare the methods and results obtained by reducing and analyzing the observations of clusters, with the most recent knowledge on XMM-Newton data analysis, to the previous work by Allen et al. (2008), performed with Chandra data.

Seven galaxy clusters fulfilling the conditions mentioned above are included in the present study. The cluster observations selected differ in exposure time and overall data quality. In cases where more than one observation was available the one with the longest exposure time was selected.

The seven galaxy clusters selected are hot, dynamically relaxed, and span the redshift range $0.1 < z < 0.9$. The XMM-Newton observations of the sample of clusters considered in this study are presented in table 3.1. Figure 3.1 shows the mosaic MOS image of each galaxy cluster.

3.2 THE STANDARD DATA PROCESSING

The XMM-Newton Observation Data Files (`ODF`) of the galaxy clusters selected were downloaded from the `HEASARC` archive and the standard initial processing is performed by using the XMM's Science Analysis Software (`XMM-SAS`).

The tasks `cifbuild` and `odfingest` are the first used. The task `cifbuild` generates the Current Calibration File Index (`CIF`) of the observation. The `XMM-SAS` tasks access the correct calibration files necessary for the data processing through the index file (SAS User Guide 2010).

The task `odfingest` extends the basic summary file contained in the `ODF` adding

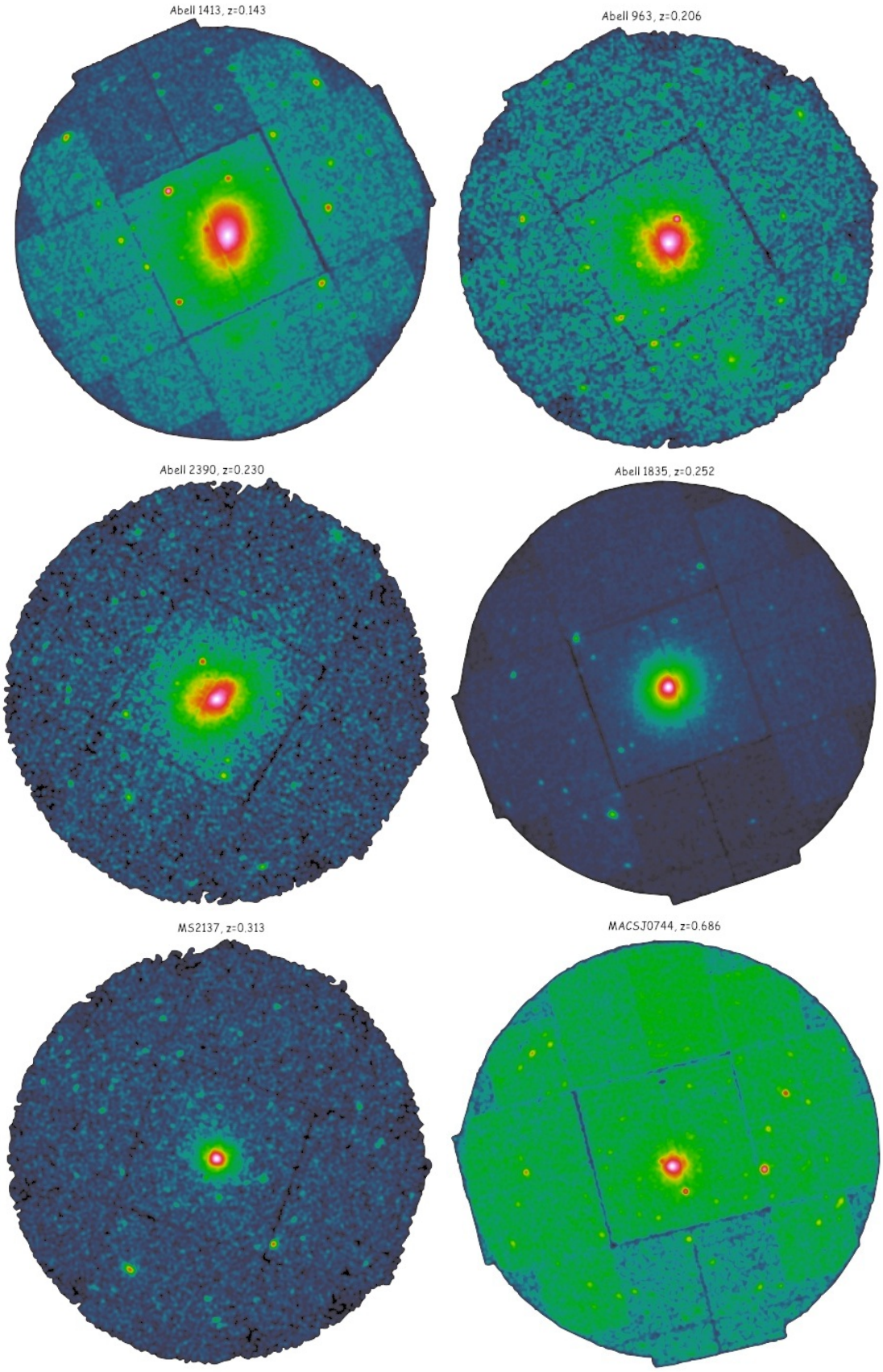

Figure 3.1: *The cluster sample - mosaic MOS images. Figure continues.*

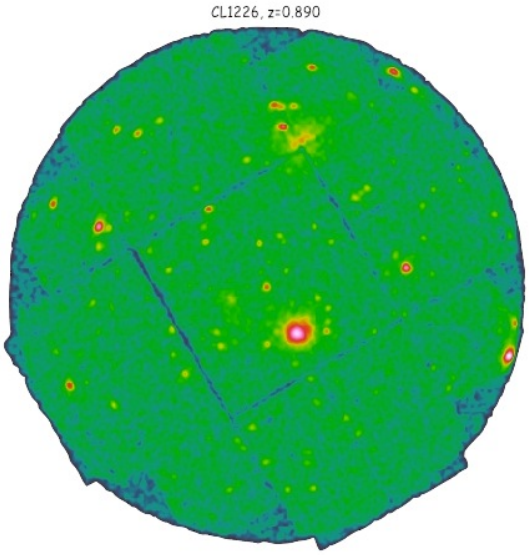

Figure 3.1 *continued, ClJ1226.9+3332.*

information extracted from the instrument housekeeping data files and the calibration database. It creates a new extended summary file of the observation in question (SAS User Guide 2010). The summary file is accessed by the different `XMM-SAS` tasks used in the data processing.

To produce event files for the MOS1 and MOS2 detectors the task `emchain` is used. The event files generated are the output of the standard data processing and are ready for scientific analysis.

Clusters of galaxies are extended X-ray sources. The analysis of extended objects and the diffuse background using XMM-Newton MOS observations is addressed with the use of the XMM-Newton Extended Source Analysis Software (`XMM-ESAS`) package, part of `XMM-SAS`. The package `XMM-ESAS` consists of a collection of tasks developed by Snowden et al. and follows the methods outlined in Snowden et al. (2008).

The treatment of the event files for scientific analysis consists of: 1) filtering the data for soft proton contamination; 2) examination of the detector's CCDs in case they are operating in anomalous state; and 3) identification and exclusion of point sources and substructures.

The output obtained by performing these three steps are cleaned event files that are now used to subtract the quiescent particle background, model the cosmic X-ray background and account for possible effects of the limited Point Spread Function (PSF) of XMM-Newton. The effect of the X-ray background is addressed in chapter 4.

Observations from the EPIC pn detector were not considered at any point for scientific analysis due to the fact that, at the time of writing, pn specific software is not included in the `XMM-ESAS` release version and open issues remain concerning an un-

derestimation of the pn particle background (Snowden et al. 2010). To keep the analysis simple, only data from the EPIC MOS detectors is considered.

3.3 FILTERING THE DATA

To filter the events files, produced by `emchain`, the `XMM-ESAS` task `mos-filter` is used. It finds the observation processed by `emchain` and filters the data for soft protons flares.

The task `mos-filter` calls the task `espfilt`, which identifies the observation good time intervals and removes the intervals affected by soft proton flares, providing what is called "light curve cleaning". In short, two light curves and a high-energy count rate histogram are extracted from the field of view data. A Gaussian is fit to the histogram peak and the thresholds are determined at plus and minus 1.5σ (see Snowden et al. 2010).

Diagnostic files that are very helpful when evaluating the quality of the observation are also produced by `mos-filter`. Of particular interest are the plot files showing the light curves, the histogram fit and the accepted time intervals. By examining these diagnostic files it is possible to determine the level of contamination and if the observation in question is useful for the study of extended sources such as galaxy clusters.

Figure 3.2 shows an example of a diagnostic file, showing the temporal filtering results of the observation of Abell 1835 (the accepted time intervals are identified in green).

The light curve filtering applied by `mos-filter` physically excises data from the event files. In cases where the observations are significantly affected, a large amount of the observation time is rejected. The filtering is therefore, in all cases, a trade-off between good time interval (G.T.I.) and quality of data.

3.4 MOS IMAGES

Images of the whole field of view are extracted from the filtered event files using the `XMM-SAS` task `evselect`. That allows for a first look at the systems selected.

Direct inspection of the images permits the identification of bright X-ray point sources and eventual substructures within the intra cluster medium.

Even though the systems selected in this study are a subsample of a larger cluster sample reported by Allen et al. (2008) with a selection criteria based on, among other things, the dynamical condition of the galaxy clusters, two of the clusters do present obvious substructure.

The clusters Abell 2390 and MACSJ0744+3927 are systems where clear substructure is observed between position angles of 255-15 degrees and 210-330 degrees, respectively. The presence of substructure in these clusters has been reported previously in

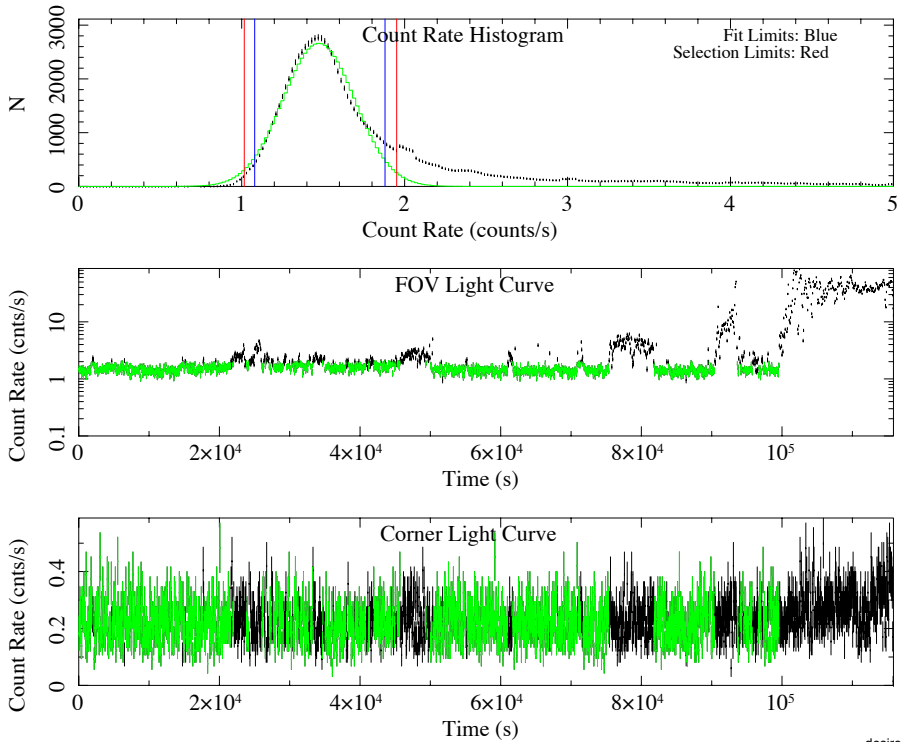

Figure 3.2: *Diagnostic file showing the temporal filtering results of the observation of Abell 1835. The accepted time intervals are identified in green.*

studies considering Chandra data (Allen et al. 2008, 2002).

The point sources and regions associated with substructure in these clusters have been excluded from the further analysis. Figure 3.4 shows the MOS image of Abell 1413 where point sources and substructure were excised.

3.4.1 Examination of CCDs

Depending on the time of observation, a MOS1 detector CCD can be missing (MOS1 is missing a CCD), and CCDs from both MOS1 and MOS2 can be operating in anomalous state, where the X-ray background below 1 keV is strongly enhanced. A missing CCD is easily detected by image inspection while a detector operating in a anomalous state may not be obvious and screening of a image considering the whole energy band may not be sufficient.

In order to check for CCDs operating in anomalous state, images of the entire field of view were produced covering the energy ranges 0.3 keV to 1.0 keV and 1.0 to 3.0 keV to look for enhanced numbers of counts revealing the affected CCDs.

The affected CCDs have been identified and excluded from the analysis. In figure 3.3 it is clear to see the missing MOS1 CCD. Figure 3.3 also shows the low energy image

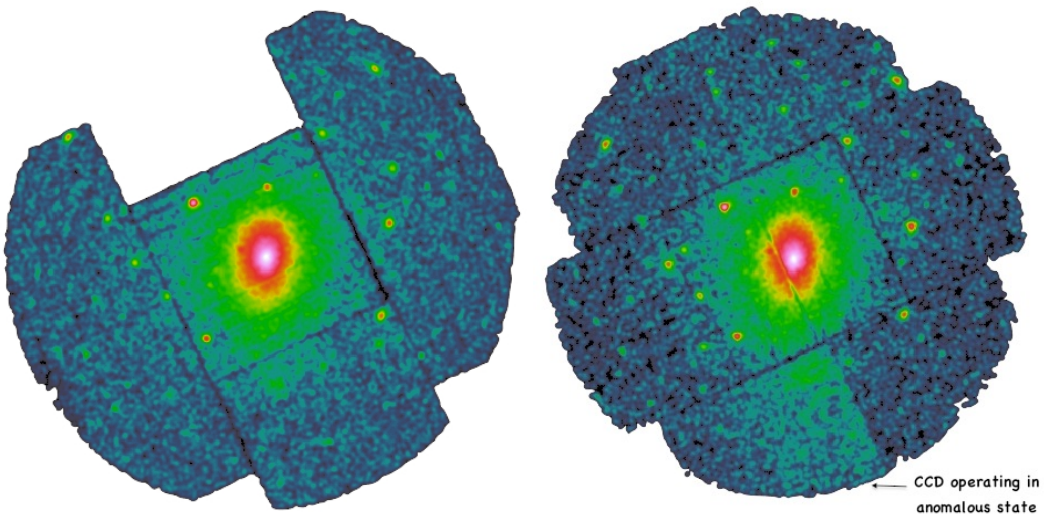

Figure 3.3: *MOS1 (left) and MOS2 (right) low energy images of Abell 1413. The energy range covered is between 0.3keV and 1.0keV. The MOS1 image (left) shows a missing CCD. The MOS2 image (right) reveals a CCD operating in anomalous state, with the enhanced number of counts (lower right CCD).*

of Abell 1413 with a MOS2 CCD operating in an anomalous state.

3.4.2 POINT SOURCES

For the analysis of diffuse X-ray emission it is necessary to remove the contribution of point sources. To detect and exclude point sources, images, exposure maps and detection masks were created, which are then used by the source-searching task `eboxdetect` to create source lists.

The source list produced by the `eboxdetect` task is compared to the images, examined by eye and corrected if necessary. A filtered event file with point sources excised is produced. Figure 3.4 shows the image of the cluster Abell 1413 with the point sources and eventual substructure removed.

3.4.3 CLEAN IMAGES

After identifying the regions of the images with substructure, point sources and CCDs operating in an anomalous state, a new "clean" event file is produced where identified substructure, point sources and detectors are excised.

The *clean* event files are used to produce the images that will later be used in the spatial analysis of the clusters. The `XMM-ESAS` task `mos-spectra` is used to create images. This task produces both spectra and images for defined regions or the entire field of view depending on the input given. The images were produced considering the entire field of view and an energy range between 0.7keV and 7.0keV.

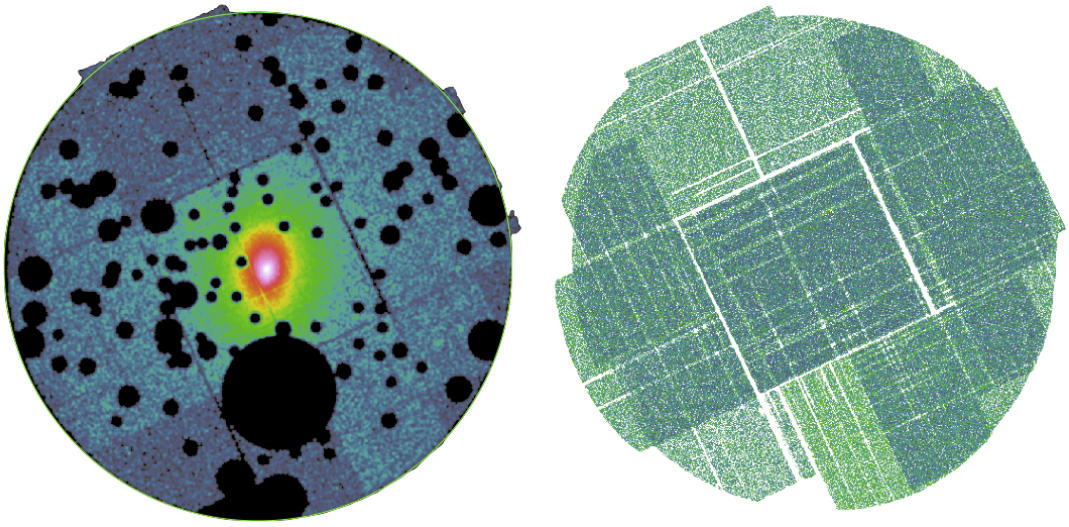

Figure 3.4: *Mosaic image (left) of the cluster Abell 1413, produced by combining the images from MOS1 and MOS2, showing the areas of excluded point sources and substructure. Mosaic image of the X-ray particle background (right) affecting the observation of Abell 1413.*

The source images from the detectors MOS1 and MOS2 are combined into a mosaic image. Both figures 3.4 and 3.5 are examples of the combined images of Abell 1413 and Abell 1835 respectively.

Exposure maps containing the exposure (in units of seconds) of the observation are also produced by `mos-spectra` for the energy range selected. The exposure maps created for each detector are also combined into a mosaic exposure image.

The `XMM-ESAS` task `mos-back` uses the intermediate files generated by `mos-spectra` to model the quiescent particle background and create images. The background images are combined into a mosaic background image and subtracted from the source image for the spatial analysis. Figure 3.4 shows the quiescent particle background image of Abell 1835.

The background image produced by `mos-back` is given in detector coordinates. To reproject the image from detector coordinates into sky coordinates the `XMM-ESAS` task `rot-im-det-sky` is called. It uses information from the source image created by `mos-spectra` in sky coordinates to rotate the detector coordinate particle background images produced by `mos-back` into sky coordinate images (Snowden et al. 2010).

The final image set produced here includes combined source images, exposure maps and particle background images that will be used for the scientific analysis described in chapter 5.

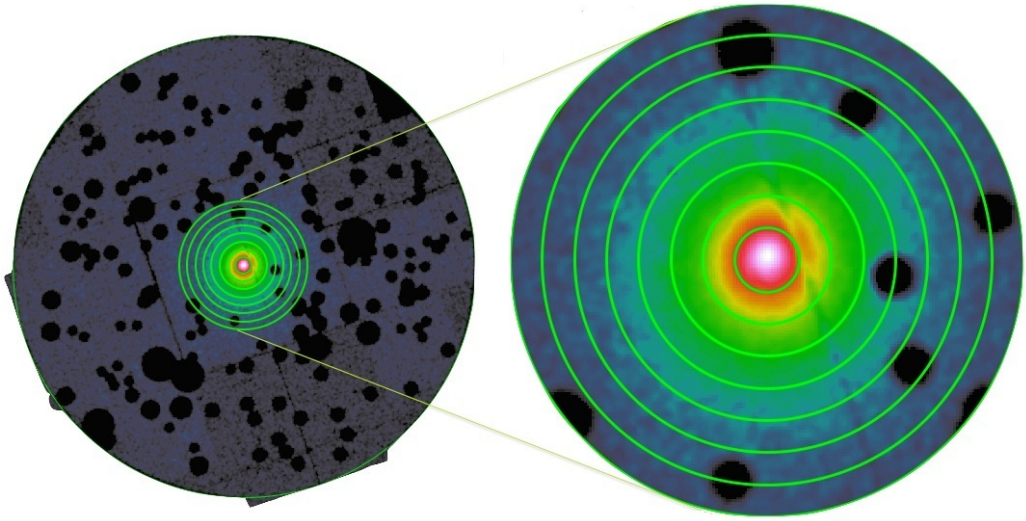

Figure 3.5: *Field of view of Abell 1835 with the concentric annuli considered for extraction of spectra. The image to the right shows a zoom in of the cluster's center and annuli.*

3.4.4 THE CLUSTER CENTER AND NUMBER OF COUNTS

To determine the center of the galaxy cluster the mosaic source image is used together with the exposure image and background image produced from the clean event files.

All images are manipulated by using the software IDL. The source image is divided by the normalized exposure map and has the background image subtracted, producing a image free from particle background.

A two dimensional Gaussian is fit to the particle free image considering a region of radius 500 kpc centered at the approximate cluster's center, identified by eye. The result of the fit is the peak of the X-ray emission and defined for further analysis to be the cluster's center.

For the clusters presenting substructure, Abell 2390 and MACSJ0744.9+3927, the Gaussian fit was not performed and it was assumed that the center's coordinates are the same as reported by Allen et al. (2008).

Reading the image files in IDL allows for inspection of the number of counts in the particle background subtracted image and permits to evaluate the width of an annulus centered at the cluster's center.

The annulus area is defined based on the number of counts it includes. Knowing the number of counts within a specific area is necessary to decide how the annuli regions considered for spectra extraction, and therefore radial analysis, should be distributed.

The field of view of the galaxy cluster Abell 1835 and the concentric annuli considered for extraction of spectra are illustrated in figure 3.5.

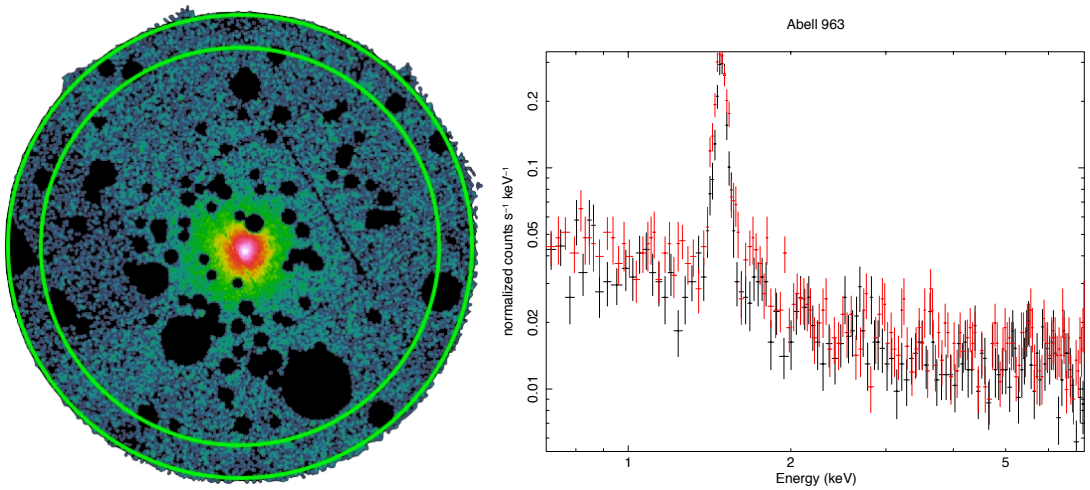

Figure 3.6: *Mosaic image of Abell 963 (left) with the annulus region surrounding the cluster selected for spectra extraction. The spectra (right) from MOS1 (black) and MOS2 (red) of the same region, used to model the cosmic X-ray background.*

3.5 MOS Spectra

The `XMM-ESAS` task `mos-spectra` produces both spectra and images from the cleaned event files. All spectra produced for scientific analysis had the energy range from 0.7 keV to 7.0 keV considered.

While the particle background is subtracted from the dataset, the cosmic X-ray background has to be modeled explicitly. Therefore, the first spectra extracted are from an annulus surrounding the galaxy cluster. The spectra are used to model the cosmic X-ray background under the assumption that the X-ray emission in the annulus area surrounding the cluster is a good representation of the cosmic background.

The different particle background components and the modeling of the cosmic X-ray background are described in detail in chapter 4.

Figure 3.6 shows a MOS1 and MOS2 mosaic image of Abell 963, the annulus region surrounding the cluster selected for the extraction of spectra and the spectra from MOS1 and MOS2 of the same region.

To allow for a radial analysis of the galaxy clusters, spectra from concentric annuli centered at the cluster's center are generated. The annuli are distributed in order to obtain a spectrum consisting of enough counts that will provide good statistics when fitting a model to the observed data. The criterion is to obtain a spectrum of each annulus containing at least a few 1000 counts. Figure 3.5 illustrates the annuli distribution selected for the cluster Abell 1835.

Other than spectra and images, the outputs files of `mos-spectra` include the redistribution matrix (RMF file) and the ancillary response file (ARF). The RMF matrix

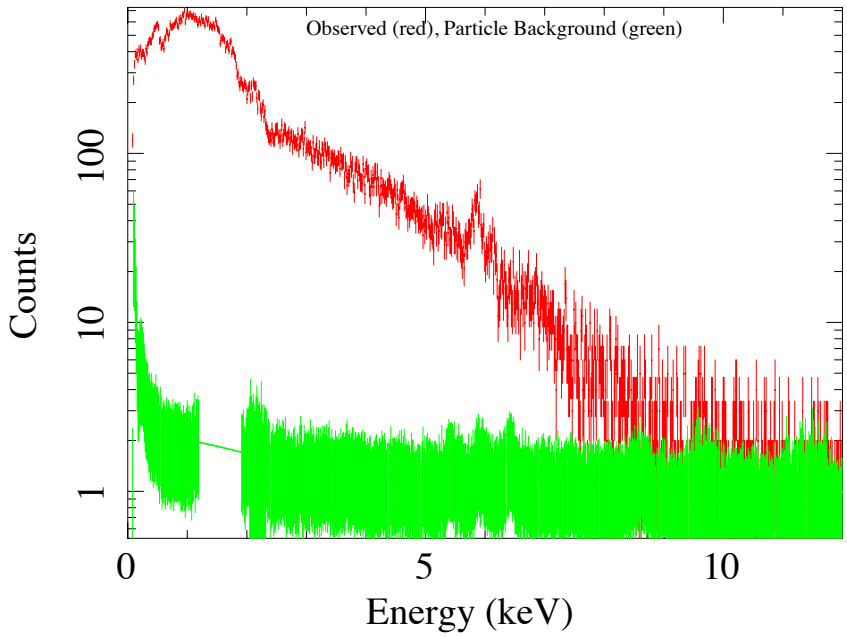

Figure 3.7: *The source spectrum of Abell 1413 (red) and the corresponding particle background spectrum (green) produced by the task mos-back.*

describes the response of the instrument as a function of energy and the ARF is an effective area vector. Both the RMF and ARF are used to perform spectral analysis allowing the fitting of spectral models to the observed spectral data. The spectral analysis is described in chapter 5.

3.5.1 PARTICLE BACKGROUND SPECTRA

For each spectrum, extracted from a specific region, a particle background file is also produced. The particle background image and spectrum are produced by the task `mos-back` which uses the intermediate files generated by `mos-spectra` to create a quiescent particle background spectrum. The source spectrum of Abell 1413 and the corresponding particle background produced by `mos-back` are shown in figure 3.7.

The particle background spectrum is used together with the source spectrum and response files, RMF and ARF, to perform spectral analysis, described in chapter 5.

3.5.2 PSF CORRECTION

Because of the size of the PSF in the EPIC detectors, a fraction of photons emitted in one part of the sky are detected at another position on the detector. This can cause an extracted spectrum of a region to have a flux contribution from different areas of the extended source emission.

To account for the effects of the PSF size, a modification of the `XMM-SAS` task `arfgen` is used. The cross-talk effective area file for X-rays detected in one region of the detector that originate in another region of the sky is produced by `arfgen` using both spectra from the region considered and from the neighboring regions.

A detector map is also a necessary input to `arfgen`. The map is produced in detector coordinates, with a pixel size small compared to the size of the region selected to properly sample the area selected.

The cross-talk effective area file, which is a modified ARF, is used together with the RMF, to account for the effects of the PSF in the spectral analysis. In the latest version of Xspec (v.12) the cross-talk between adjacent annuli is considered as an additional model component with the parameters linked to the cluster source spectral model.

3.6 FINAL EPIC MOS PRODUCTS

The MOS images and spectra produced and listed in this chapter are ready for scientific analysis. The filtered event files have the contamination by soft protons, X-ray point sources, substructures and CCDs operating in an anomalous states removed.

Using the filtered event files, images were produced to determine the centers of the galaxy clusters and number of counts available. The images produced are: 1) source images; 2) exposure maps; and 3) particle background images.

The images from each detector were combined in mosaic images. The source images are corrected by using the respective exposure maps and have the quiescent particle background images subtracted. The final images are used for spatial analysis of the clusters, described in chapter 5.

The spectral products are: 1) source spectra (including source and background) ; 2) particle background spectra; 3) redistribution matrices (RMF); 4) effective area files (ARF); and 5) cross-talk effective area files (modified ARF).

Source spectra and particle background spectra of an annulus surrounding each of the galaxy clusters were extracted together with their respective response files, ARF and RMF, and are used to model the cosmic X-ray background affecting each system. The background modeling is described in chapter 4.

Source spectra and particle background spectra of concentric annuli centered at each galaxy cluster center were extracted. The response files, ARF and RMF, of each annulus and the modified ARF to account for the cross-talk between annuli were produced. These files are used together in the spectral analysis of the galaxy clusters, as described in chapter 5.

4

THE X-RAY BACKGROUND

"I think my eyes are getting better.
Instead of a big dark blur, I see a big light blur."
Han Solo, Star Wars Episode VI: Return of the Jedi (1983)

ABSTRACT – *The aim of this chapter is to describe the X-ray background affecting the XMM-Newton observations of the galaxy clusters selected for this study. A short introduction to the several X-ray background components is presented. Both instrumental background and cosmic X-ray background are taken into consideration. The instrumental background is excised from the data, while the cosmic X-ray background is modeled explicitly. The best fit model of the cosmic X-ray background is derived making use of both ROSAT and XMM-Newton data.*

4.1 INTRODUCTION

The EPIC MOS detectors of XMM-Newton are affected by several different background components. For the analysis of extended sources like galaxy clusters the lack of proper consideration of the X-ray background affecting the data will lead to incorrect science results, affecting, among other things, the determination of the temperature of the X-ray emitting gas.

The background contamination is considered by identifying and removing the particle background from the dataset while the remaining cosmic background is modeled and included in the further spectral analysis. This chapter is based on the methods described in Snowden et al. (2008).

4.2 THE BACKGROUND COMPONENTS

The different X-ray background components originate from photons, particles and electric noise. Most of them vary in time and in position on the sky, it is therefore necessary to carefully address the individual background contamination of each observed galaxy cluster.

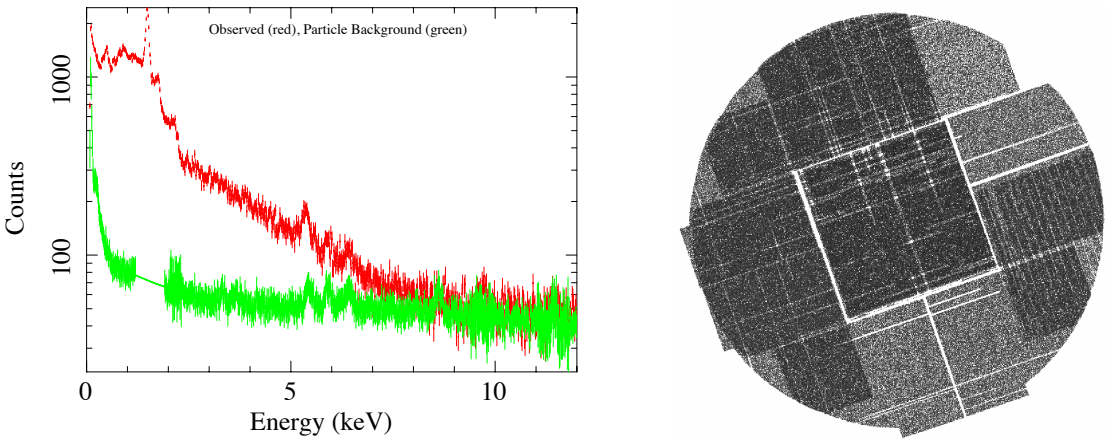

Figure 4.1: *Quiescent particle background spectrum and image of Abell 1835 created by mos-back. Left: the observed spectrum is represented in red and the modeled quiescent particle background in green. The Al and Si lines dominating the X-ray fluorescent background are visible in the observed spectrum between 1 keV and 2 keV. Right: combined quiescent particle background image of the detectors MOS1 and MOS2.*

The background components addressed in this study are the quiescent particle background, the fluorescent X-ray background, soft proton background, and last but not least, the cosmic X-ray background.

4.2.1 THE QUIESCENT PARTICLE BACKGROUND (QPB)

High energy particles such as cosmic rays interact with the detectors producing X-rays that are detected and form a continuum quiescent particle background.

The XMM-Newton Extended Source Analysis Software (`XMM-ESAS`) allows the identification of the quiescent particle background for both spectra and image analysis. The task `mos_back` creates both spectra and image of the particle background.

The quiescent particle background spectrum is used together with the observed source spectrum in the later spectral analysis. For each spectrum extracted from the cluster observation, a corresponding quiescent particle background spectrum and image are produced.

The quiescent particle background image is subtracted from the original cluster source image to produce a quiescent particle background free image for the later spatial analysis. Both spectra and images treated with the quiescent particle background still carry background contamination from other sources, e.g. the cosmic X-ray background component presented below.

Figure 4.1 shows the quiescent particle background image and the source spectrum with its respective particle background spectrum of the galaxy cluster Abell 1835.

Cluster	Redshift	Original	G.T.I.	Reduction
Abell 1413	0.143	82.448	63.84	22.5%
Abell 963	0.206	27.461	26.01	5.3%
Abell 2390	0.230	23.105	9.88	57.2%
Abell 1835	0.252	120.870	71.82	40.5%
MS2137.3-2353	0.313	22.621	10.80	52.2%
MACSJ0744.9+3927	0.686	98.286	62.58	36.3%
ClJ1226.9+3332	0.89	98.829	64.60	34.6%

Table 4.1: *Original observation exposure times and the good time intervals (G.T.I.) after removal of soft protons flares. Exposure times and G.T.I. are listed in kilo seconds. The last column (Reduction) represents the percentage of observation time excised due to contamination by soft proton flares.*

4.2.2 THE FLUORESCENT X-RAY BACKGROUND

The fluorescent X-ray background affecting XMM-Newton observations is generated by particles that interact with the satellite, creating X-ray photons that are registered by the detectors. It dominates the spectrum in the range 1.3-1.9 keV where Al and Si lines are observed.

The fluorescent background is excised from the data. The energy range between 1.2 keV and 1.9 keV is not considered in the spectral fitting. In figure 4.1 it is possible to observe the lines that dominate the fluorescent X-ray background of Abell 1835.

The fluorescent background could be modeled instead of being removed. Two Gaussian models could be added to the spectral fitting models to consider the contribution from the Al and Si lines, but that should be carefully considered as the extra model components may not properly describe the fluorescent background and could influence negatively in the overall spectral fitting of the cluster spectrum.

In this study, the energy range contaminated by the X-ray fluorescent background was excised for all data sets.

4.2.3 SOFT PROTON BACKGROUND

The soft proton background is produced by solar protons accelerated by magnetospheric reconnection events. Their relatively low energy is of the order of less than a few hundred keV, and is deposited in the CCD detectors.

The soft proton background is not simple to handle. It is strongly variable, sometimes undetectable, while in other cases present in strong flares easily visible in the examination of the light curves.

To aim towards freeing the observation from soft proton contamination, the light curves of the whole field of view were analyzed. That is done using the `XMM-ESAS` task `mos-filter`. In short, `mos-filter` provides a filtering of the light curve, described

in chapter 3. The filtering removes the time intervals affected by soft proton flares, and creates diagnostic files and plots that can be examined before proceeding with the data reduction.

Figure 4.2 shows the temporal filtering results for ClJ1226.9+3332.

Filtering the light curve in this way, and discarding the affected periods, reduces the observation time. For A2390 the reduction reaches 57%. Table 4.1 presents the exposure times before and after filtering.

There is no guarantee that the temporal filtering performed by `mos-filter` removes all soft protons, it is therefore necessary to also consider the possibility of residual contamination.

Checking for residual soft protons is done by comparing the count rates in the field of view beyond 10 arc minutes to the count rates in the area of the detectors outside the field of view (De Luca & Molendi 2004). The higher the ratio between the two count rates, the more contaminated the observation is. If the ratio between the two count rates is less than 1.15, the observation has no residual contamination by soft protons. Ratios between 1.15 and 1.3 indicate a slightly residual contamination. A observation presenting a ratio between 1.3 and 1.5 is very contaminated, and finally, a ratio larger than 1.5 indicates extreme residual soft proton contamination.

Fortunately, this sample of clusters contains only one cluster affected by residual contamination. The cluster MS2137.3-2353 has a ratio between the count rates of 1.43, meaning its observation is very contaminated by residual soft protons that were not successfully removed by filtering of the light curve. The effect of the residual soft proton contamination is addressed in chapter 5.

4.2.4 THE COSMIC X-RAY BACKGROUND (CXB)

The cosmic X-ray background consists of photons from different sources in the sky. The soft X-ray photons originate from the Local Hot Bubble surrounding the solar system, the Galactic Disk and Halo. The Galactic emission dominates the cosmic X-ray background spectrum at energies below 1 keV.

The hard X-ray photons are from unresolved background sources such as Active Galactic Nuclei (AGNs) and galactic stars (Hickox & Markevitch 2007; Kuntz & Snowden 2001). The contribution from unresolved background sources dominates the cosmic X-ray background spectrum at higher energies (above ≈ 1 keV).

The cosmic X-ray background is strongly variable over the sky and each component has to be modeled explicitly.

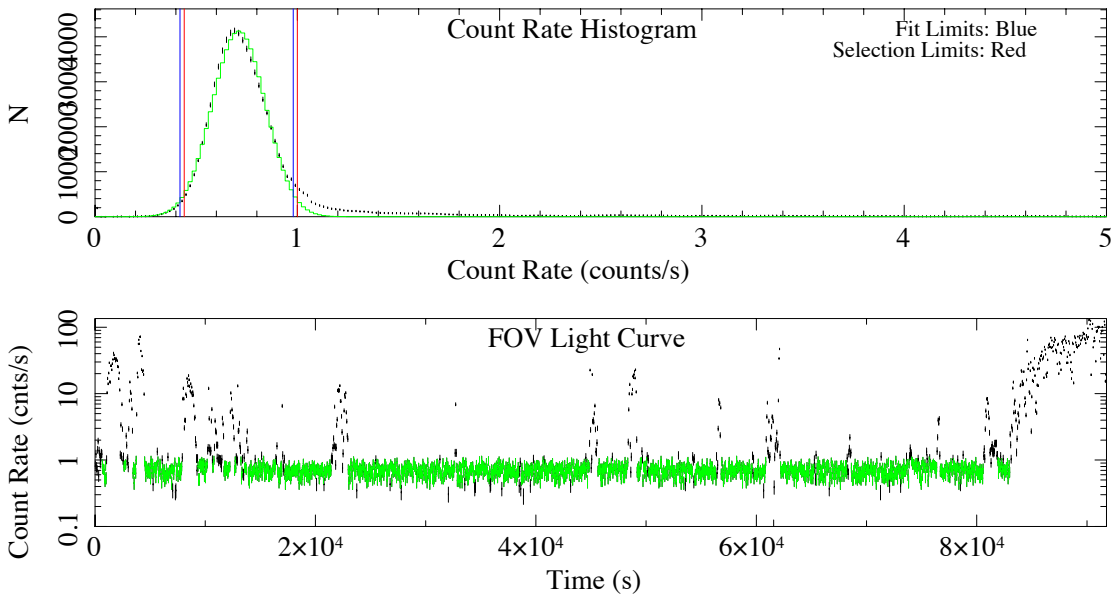

Figure 4.2: *Light curve analysis of ClJ1226.9+3332 produced by mos-filter. The upper panel shows the histogram of the light curve count rate and a Gaussian fit to the peak of the distribution. The thresholds for filtering are the vertical lines set at the mean value of the Gaussian plus 1.5σ. The lower panel shows the soft proton flares excluded (black) and the good time intervals are marked in green.*

4.3 Modeling the Cosmic X-ray Background

The cosmic X-ray background model includes the contribution of the Galactic halo emission, described by an absorbed thermal component, the Local Hot Bubble (LHB), described by an unabsorbed thermal component, and unresolved sources accounted by an absorbed power law.

$$S_{CXB} = N_H \times (T_{Halo} + P) + T_{LHB} \tag{4.1}$$

The equation 4.1 includes an absorption component, N_H, two thermal components, T_{Halo} and T_{LHB}, and a power law, P.

N_H is the total Galactic neutral hydrogen column density and it is fixed to the average value from the Leiden/Argentine/Bonn (LAB) Survey of Galactic neutral Hydrogen at the coordinates of the cluster (Kalberla et al. 2005).

The absorbed thermal component, T_{Halo}, represents the cosmic X-ray background from the Galactic halo. The absorbed power law, P, accounts for the extragalactic cosmic background coming from unresolved X-ray sources, and the unabsorbed thermal component, T_{LHB}, models the cosmic background from the Local Hot Bubble we are in.

The parameters used to model the cosmic X-ray background are shown in table 4.2.

Spectral component	Parameter	Initial value	Constraint
N_H column density	nH	Set	Fixed
CXB LHB	kT	0.25	Free
-	Abundance	1.0	Fixed
-	Redshift	0.0	Fixed
-	Normalization	5.0×10^{-6}	Free
CXB halo	kT	0.08	Free
-	Abundance	1.0	Fixed
-	Redshift	0.0	Fixed
-	Normalization	5.0×10^{-6}	Free
CXB Unresolved	γ	1.46	Fixed
-	Normalization	8.88×10^{-7}	Fixed/Free

Table 4.2: *The different cosmic X-ray Background model components of the spectral fitting.*

An example of the cosmic X-ray background model is shown in figure 4.4.

To model the cosmic X-ray background, both MOS spectra from the cluster sample and data from ROSAT All-Sky Survey (RASS) are used. The motivation for the use of RASS data is to better constrain the fit of a model to background spectrum.

For the most nearby cluster in this sample, Abell 1413, at redshift 0.143, the assumption that the annulus surrounding the cluster is a good representation of the cosmic X-ray background is uncertain due to the possible existence of cluster emission out to the outer part of the field of view. Using RASS data is therefore needed to provide better constrain to the spectral fit.

The lowest energy limit considered for extraction of MOS spectra is 0.7 keV, while RASS spectra is available from 0.1 keV, improving the determination of the cosmic X-ray background at low energies.

The MOS source spectrum and the quiescent particle background spectrum of an annulus surrounding each galaxy cluster are extracted. The region considered is in the outskirts of the field of view, between 12 and 14 arc minutes from the center of the field of view. Figure 4.3 shows the annulus region considered.

The X-ray background data from RASS is generated using the HEASARC X-ray background tool, developed and maintained by Edward J. Sabol of the HEASARC and based primarily on the research of Dr. Steve Snowden (see e.g., Snowden et al. 1997). For all clusters, the spectrum of an annulus between 20 and 60 arc minutes centered at the cluster coordinates is produced.

To model the cosmic X-ray background, two approaches are taken: 1) RASS and MOS spectra are fit separately; and 2) RASS and MOS spectra are fit simultaneously.

For the spectral analysis, the XSPEC package (Arnaud 1996) version 12.6.0 is used.

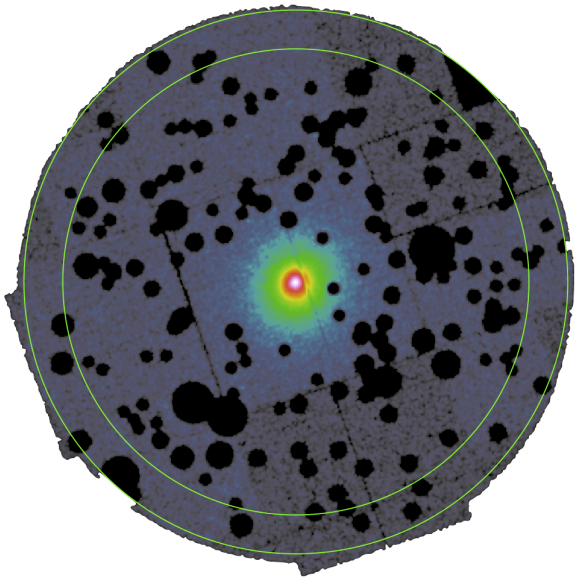

Figure 4.3: *Annulus surrounding the galaxy cluster Abell 1835. The diffuse X-ray emission identified in this outer annulus is assumed to represent cosmic X-ray background.*

4.3.1 THE USE OF RASS SPECTRA

In the first approach, the RASS and MOS spectra are fit separately. The RASS spectrum is fit considering the energy interval 0.1-3.0 keV.

The RASS spectrum is heavily binned and χ^2-statistics is used for the spectral fit. The best fit values obtained by fitting the RASS spectrum are used as starting values when fitting the XMM-Newton spectra of the outer annulus of each cluster.

Spectra from MOS1 and MOS2 are fit simultaneously and two constants are added to the fitting model to account for the extraction area and eventual calibration offset between the detectors.

Because the calibration of XMM-Newton at very low energies is uncertain, the MOS spectra are fit from 0.7 keV to 3.0 keV. At this energy interval, we can not constrain the values of the background components from MOS data alone. The starting values from the RASS best fit are set and fixed, and only the normalizations are allowed to vary.

The motivation for this approach came from the initial intention of not to bin the MOS spectra and use Cash statistics for the spectral fitting. RASS data is binned and has to be fit using χ^2-statistics. With the different statistical methods it would not be possible to fit spectra from both RASS and MOS simultaneously.

4.3.2 RASS AND MOS SIMULTANEOUS FIT

In the second approach, RASS and MOS spectra are fit simultaneously. The MOS spectra are binned considering 15 counts per bin and χ^2-statistics is used to fit the model

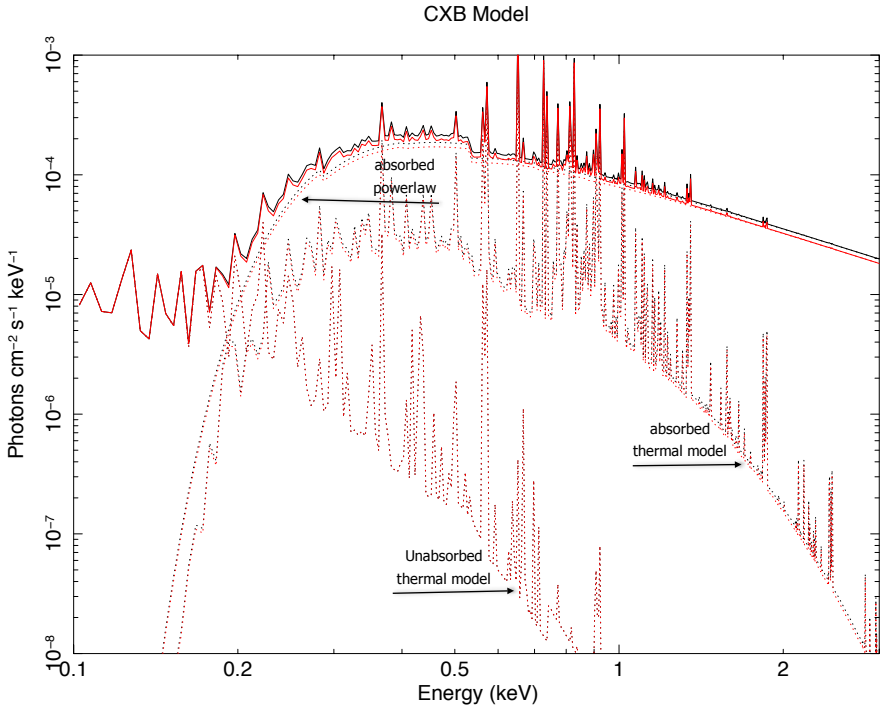

Figure 4.4: *Example of the cosmic X-ray background model obtained with XSPEC. The absorbed thermal and power law components added to the unabsorbed thermal component are represented in this plot and make the theoretical model fit to the spectra of MOS1(black) and MOS2 (red).*

described by equation 4.1 to the spectra.

The three spectra, from RASS, `MOS1` and `MOS2`, are loaded into XSPEC as individual data groups but have all free parameters listed in table 4.2 linked.

The RASS spectrum is scaled according to the extraction area in units of square arc minutes. Its is therefore necessary to also scale the MOS spectra for consistency with the scaled RASS data. Two constants are added to the model, one representing the region solid angle of the MOS detectors and another to account for any calibration offset between the detectors, allowing for linking the normalization parameters of both detectors.

The best fit model of the cosmic X-ray background to the spectra of ClJ1226.9+3332, considering both MOS and RASS spectra, is shown in figure 4.5.

4.4 Results

Background removal and modeling is performed on each of the observations of the seven galaxy clusters in this sample. Time intervals contaminated by soft protons flares are removed from the dataset. The contribution from the quiescent particle background

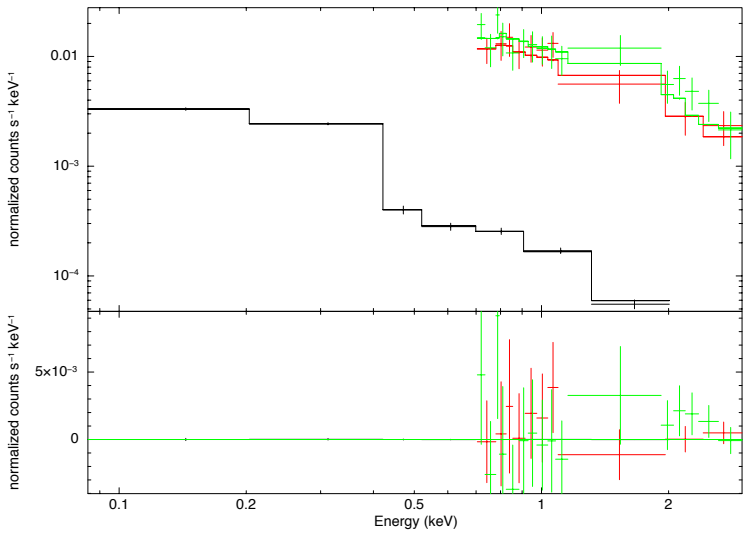

Figure 4.5: *Spectra and model of the cosmic X-ray background in ClJ1226.9+3332. The RASS spectrum is represented in black, MOS1 in red and MOS2 in green. The three spectra are fit simultaneously and have all free parameters linked. The lower panel shows the model residuals.*

is identified by the task `mos-back` and the cosmic X-ray background is accounted by fitting a model to both MOS and RASS spectra of an annulus surrounding the cluster.

The light curve analysis and the subsequent filtering for soft proton contamination reduces the observation time significantly. Table 4.1 presents the original observation times and the remaining good time intervals after applying the filtering. For the most affected system, Abell 2390, nearly 60% of the observation time is discarded. The least affected cluster is Abell 963 with only 5% of the observation time contaminated by soft proton flares.

Each of the seven clusters has an individual model of the cosmic X-ray background. The cosmic X-ray background model is added to the absorbed thermal component of the galaxy cluster model when fitting the final cluster spectrum. The combined model to fit the cluster spectrum is described in chapter 5.

Table 4.4 presents the best fit values of the free parameters obtained by fitting the RASS data alone and by fitting the spectra from both RASS and MOS simultaneously.

Trying to fit only the MOS spectra and allowing the temperature and normalizations to vary was not possible in the energy range 0.7-3.0 keV considered and MOS data alone can not properly constrain the background model parameters. The temperatures of the thermal components in this case are set to the values obtained by fitting the RASS spectrum.

Even with the values of the temperatures fixed, setting the normalization parameters free didn't provide sensible results. The solution was to fix the parameters to RASS best fit values, allowing only the power law normalization to vary. For all clusters this

results in significantly higher value for the power law normalization parameter, which for RASS spectra is fixed to 8.88×10^{-7} (Kuntz & Snowden 2000).

The absorbed power law model component represents the contribution from unresolved X-ray sources to the spectrum. The excision of point sources during the data reduction procedure do affect the power law component. The point source removal was not performed to a uniform threshold, it was chosen, therefore, to set the power law normalization parameter free for the spectral fitting.

The simultaneous fit of spectra from both RASS and MOS allow for the parameters to be set free. Comparing the best fit values from the two approaches, there is little difference in the results of the unabsorbed thermal component, representing the Local Hot Bubble we are in, while the absorbed thermal component and normalization of the power law, representing contributions from the Galactic halo and unresolved sources respectively, show a more significant variation.

The normalization of the power law representing unresolved point sources obtained is close to 8×10^{-7} for five out of seven clusters, with Abell 2390 and Abell 1835 presenting a higher normalization value.

The cosmic X-ray background model considered for the further data analysis is the one obtained by fitting using both RASS and MOS spectra simultaneously. The cluster data analysis and effects of the background modeling are presented and discussed in chapter 5.

Cluster	Component	Parameter	RASS	RASS + MOS
Abell 1413	Halo	kT	0.315	0.315
	-	Normalization	4.450×10^{-7}	2.75475×10^{-7}
	LHB	kT	0.101	0.101
	-	Normalization	2.683×10^{-6}	2.683×10^{-6}
	Unresolved	Normalization	8.88×10^{-7}	9.49×10^{-7}
Abell 963	Halo	kT	0.304	0.432
	-	Normalization	3.460×10^{-7}	2.843×10^{-7}
	LHB	kT	0.097	0.099
	-	Normalization	3.815×10^{-6}	3.871×10^{-6}
	Unresolved	Normalization	8.88×10^{-7}	7.89×10^{-7}
Abell 2390	Halo	kT	0.250	0.254
	-	Normalization	1.633×10^{-7}	1.339×10^{-6}
	LHB	kT	0.101	0.098
	-	Normalization	1.179×10^{-6}	1.149×10^{-6}
	Unresolved	Normalization	8.88×10^{-7}	1.49×10^{-6}
Abell 1835	Halo	kT	0.480	0.278
	-	Normalization	5.001×10^{-7}	8.175×10^{-7}
	LHB	kT	0.129	0.122
	-	Normalization	2.937×10^{-6}	2.838×10^{-6}
	Unresolved	Normalization	8.88×10^{-7}	1.03×10^{-6}
MS2137.3	Halo	kT	0.347	0.147
	-	Normalization	7.449×10^{-7}	5.074×10^{-6}
	LHB	kT	0.129	0.129
	-	Normalization	1.676×10^{-6}	1.005×10^{-6}
	Unresolved	Normalization	8.88×10^{-7}	8.04×10^{-7}
MACSJ0744.9	Halo	kT	0.334	0.504
	-	Normalization	3.113×10^{-7}	2.455×10^{-7}
	LHB	kT	0.106	0.105
	-	Normalization	7.628×10^{-7}	1.485×10^{-6}
	Unresolved	Normalization	8.88×10^{-7}	8.16×10^{-7}
ClJ1226.9	Halo	kT	0.272	0.310
	-	Normalization	1.907×10^{-7}	2.439×10^{-7}
	LHB	kT	0.104	0.104
	-	Normalization	2.793×10^{-6}	2.800×10^{-6}
	Unresolved	Normalization	8.88×10^{-7}	8.02×10^{-7}

Table 4.3: *The best fit parameters of the cosmic X-ray background model components.*

5

DATA ANALYSIS

"Ingen roser uden torne."

Danish proverb

ABSTRACT – *In this chapter the analysis of the XMM-Newton observations of the seven clusters of galaxies is described and discussed. The global properties of the clusters, such as temperature and metal abundance are derived from the spectral fitting. The radial analysis consists of the determination of the temperature, metal abundance and density profiles. The contribution from the X-ray background is accounted for and the possible effect of PSF smearing is taken into consideration. The spatial analysis is performed using the X-ray images of each cluster and a β model is fit to the X-ray surface brightness profiles.*

5.1 INTRODUCTION

The analysis of XMM-Newton data in this study consists of both spectral and image analysis. The products of the data reduction are combined to obtain the temperature, metal abundance and density profiles of each galaxy cluster.

For the spectral analysis the XSPEC package version 12.6.0 is used. The spectral files are binned and linked to their respective response and quiescent particle background files. It is considered at least 15 counts per bin and χ^2-statistics is used for the spectral fitting.

In the case of low number of counts χ^2-statistics is still used but the Churazov weighting method is applied which estimates the weight for a given channel by averaging the counts in the surrounding channels (Churazov et al. 1996).

The application of the Churazov weighting method to the spectral fit results best fit parameters consistent to the values obtained by using Cash statistics without binning the spectral files.

5.2 SPECTRAL MODEL

To model the cluster emission an absorbed thermal model is used in addition to the cosmic X-ray background model.

$$S = C_1 \times C_2 \times [S_{CXB} + (N_H \times T_c)] \tag{5.1}$$

The spectral model of the cosmic X-ray background S_{CXB} in equation 5.1 is described in chapter 4 and has the form

$$S_{CXB} = N_H \times (T_{b1} + P_b) + T_{b2} \tag{5.2}$$

The equation 5.1 includes two constants, C_1 and C_2, an absorption component, N_H, a thermal model, and the cosmic X-ray background model S_{CXB} . The cosmic background model described by equation 5.2, includes an absorption component, N_H, two thermal components, T_{b1} and T_{b2}, and a power law, P_b.

C_1 represents any offset between the calibration of the detectors MOS1 and MOS2 and it is allowed to vary freely. C_2 represents the solid scale angle for the extraction region of the annuli and is kept fixed. The value of C_2 is different for each annulus and it is given in units of square arc minutes.

In practice, the role of C_2 is to define how much cosmic background should be considered for each annulus, as the cosmic X-ray background model is also in units of square arc minutes.

N_H is the total Galactic neutral hydrogen column density and it is fixed to the average value from the LAB Survey of Galactic neutral Hydrogen at the cluster's coordinates (Kalberla et al. 2005).

T_c is an absorbed thermal component of the galaxy cluster, where the temperature, metal abundance and normalization are allowed to vary. T_{b1} is part of the cosmic X-ray background model, it is an absorbed thermal component representing the Galactic halo.

The absorbed power law P_b accounts for the extragalactic cosmic X-ray background coming from unresolved X-ray sources. The last parameter, T_{b2}, an unabsorbed thermal component, models the cosmic X-ray background from the Local Hot Bubble we are in.

The model components describing the cosmic X-ray background have all parameters set and fixed to the values obtained by modeling the cosmic X-ray background, described in chapter 4.

The XSPEC plasma models used in this study are the Astrophysical Plasma Emission Code (`APEC`) thermal models, the photoelectric absorption (`PHABS`) model with set cross section and metal abundance model by Anders & Grevesse (1989).

Table 5.1 presents the model components and parameters used to fit the cluster spectra. The approach taken for model selection and spectral fitting adopted here is similar to the one presented in Snowden et al. (2008).

Spectral component	Parameter	Initial value	Constraint
Constants	C_1	1.0	Free*
-	C_2	Set	Fixed
nH column density	nH	Set	Fixed
Cluster	kT	5.0	Free
-	Abundance	0.3	Free
-	Redshift	Set	Fixed
-	Normalization	5.0x10^{-4}	Free
CXB Halo	kT	0.25	Free / Fixed*
-	Abundance	1.0	Fixed
-	Redshift	0.0	Fixed
-	Normalization	5.0x10^{-6}	Free / Fixed*
CXB LHB	kT	0.08	Free / Fixed*
-	Abundance	1.0	Fixed
-	Redshift	0.0	Fixed
-	Normalization	5.0x10^{-6}	Free / Fixed*
CXB Unresolved	γ	1.46	Fixed
-	Normalization	8.88x10^{-7}	Free/Fixed*

Table 5.1: *The different model components and parameters of spectral fitting. The absorbed thermal model describes the cluster. The cluster redshift is set and fixed to the known value from Allen et al. (2008). *The parameters describing the background are set and fixed to the best fit values obtained by modeling the cosmic X-ray background (CXB).*

5.3 SPECTRAL FITTING AT R_{2500}

To obtain the global properties of the clusters, such as an average temperature, metal abundance and gas density, the spectrum extracted from a circular area centered at the cluster's center and with radius equivalent to R_{2500} is fit.

The definition of radius R_{2500} is expressed in chapter 6. In short, the value of R_{2500} is defined to be the radius at which the mean enclosed cluster mass density is equal to 2500 times the critical density of the Universe at the cluster's redshift. The radius R_{2500} is therefore specific to each cluster. The values of redshift and radius R_{2500} adopted in this analysis are reported by Allen (2008).

The energy range considered for the spectral fit is from 0.7 keV to 7.0 keV. The energy range between 1.2 keV and 1.9 keV is excised from the fitting due to the contamination by the fluorescent X-ray background, described in chapter 4.

As discussed in chapter 4, the fluorescent background could, instead of being excised, be modeled by adding two Gaussian model components to the already extensive model list described in table 5.1. The use of such Gaussian models has to be considered

Cluster	redshift	R_{2500}	T_{2500}^{A08}	$\langle T_{2500} \rangle$	$\langle Z/Z_{\odot} \rangle$
Abell 1413	0.143	599^{+17}_{-19}	7.80±0.35	7.34±0.09	0.38±0.02
Abell 963	0.206	540^{+24}_{-27}	7.26±0.28	6.09±0.15	0.37±0.04
Abell 2390	0.230	662^{+42}_{-30}	11.72±1.43	9.11±0.44	0.34±0.06
Abell 1835	0.252	684^{+27}_{-26}	10.57±0.62	7.44±0.08	0.34±0.01
MS2137.3-2353	0.313	479^{+18}_{-10}	5.65±0.30	4.18±0.10	0.50±0.06
MACSJ0744.9+3927	0.686	466^{+40}_{-23}	8.67±0.98	7.73±0.42	0.31±0.06
ClJ1226.9+3332	0.890	521^{+123}_{-54}	11.95±1.97	12.36±0.94	0.21±0.09

Table 5.2: *Results of spectral fitting considering the region within R_{2500} [from Allen et al. (2008)]. The values of R_{2500} are given in kpc, the temperatures T_{2500}^{A08} and $\langle T_{2500} \rangle$ in keV and the metal abundances Z, in solar units $\langle Z_{\odot} \rangle$. The column T_{2500}^{A08} presents the average, mass weighted, temperatures reported by Allen et al. (2008) and are comparable to the values $\langle T_{2500} \rangle$ obtained in this study. Errors are computed considering 68% confidence.*

carefully because it can affect the normalization of the continuum part of the spectrum and therefore could compromise the determination of the cluster thermal component. To prevent this problem and avoid introducing more free parameters to the model, it was chosen to simply exclude the contaminated energy range.

The spectra from the detectors MOS1 and MOS2 are loaded to XSPEC as separate data groups and fit simultaneously. The cluster temperature, metal abundance and normalization parameters of each data group are linked.

The complete model has 17 parameters for each detector, a total of 34 parameters considering both MOS detectors, but only seven free parameters. The free parameters are the constant C_1 for the MOS2 data group, and the three parameters, temperature, metal abundance and normalization, for each MOS detector.

Note that with the two data groups, one for each MOS detector, the constant C_1 is set and fixed to 1.0 for the MOS1 data group and allowed vary for the MOS2 data group. The values of the free C_1 are often close to 1.0 and accounts for any difference in the calibration between the detectors.

Fitting the global cluster spectra within R_{2500} provides a first look into the properties of the galaxy clusters in question. The average values obtained are used as a starting point for fitting the many annuli of each galaxy cluster.

Table 5.2 presents the value of R_{2500} and cluster redshift from Allen et al. (2008), and the results obtained in this study by fitting the cluster's spectra with in R_{2500}. The average properties of the X-ray emitting gas such as temperature, metal abundance and density are listed.

Figure 5.1 shows the cluster Abell 963 spectra extracted considering a circular region of radius equal to R_{2500} centered at the cluster center and a folded model achieved with XSPEC.

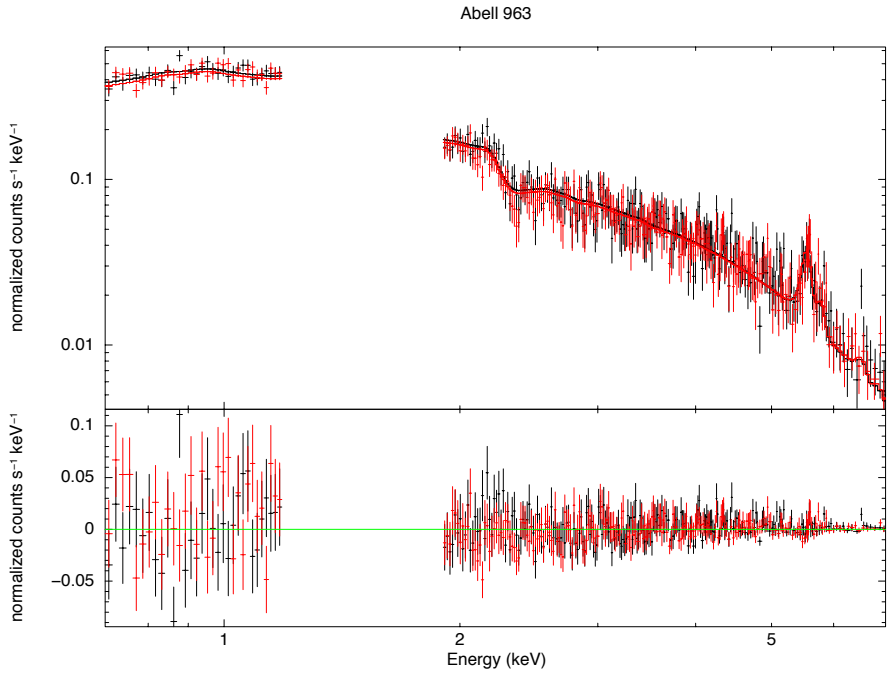

Figure 5.1: *X-ray spectra of Abell 963 considering a circular region of radius equal to R_{2500} centered at the cluster center. The spectra of MOS1 (black) and MOS2 (red) are fit simultaneously. The energy interval 1.2-1.9keV dominated by the X-ray fluorescent background is not included in the fitting process. The lower panel shows the model residuals.*

5.4 RADIAL ANALYSIS - PROFILES

The hot gas trapped in the cluster of galaxies potential is not isothermal. To obtain the gas temperature, metal abundance and density profiles it is necessary to perform a radial analysis. For that the spectra from concentric annuli centered at the cluster's center are extracted and fit.

The size and number of annuli were chosen to provide a significant fit. The choice is not unique. For systems with abundant numbers of counts, the annuli where defined so that the difference between the outer radius and inner radius is 0.5 arc minutes. For systems with less abundant numbers of counts, the annuli were defined in order to contain enough counts to allow for good statistics of the spectral fit, typically a few thousand counts per annulus.

To set up the spectral fit the data from each annulus and detector is loaded to XSPEC as a separate data group. The values of the parameters describing the cosmic X-ray background are the same for all annuli and fixed to the values obtained in the background modeling, described in chapter 4.

The free parameters belonging to the same annulus are linked and the calibration constant C_1 is allowed to vary for the MOS2 data groups.

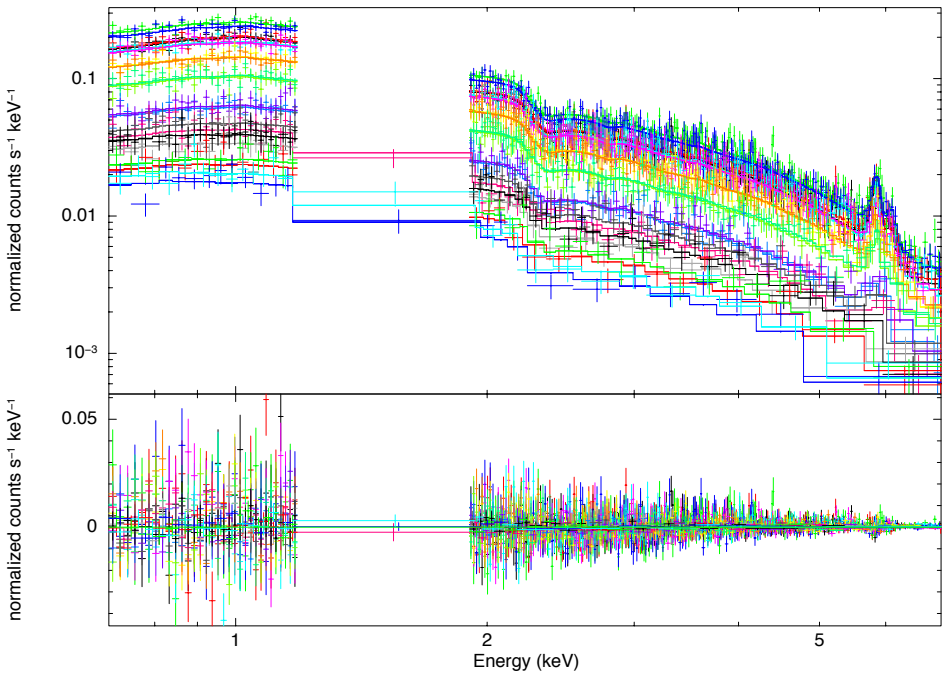

Figure 5.2: *X-ray spectra of Abell 1413. The spectra and model of 10 concentric annuli are fit simultaneously. The energy interval 1.2-1.9keV dominated by the X-ray fluorescent background is not included in the fitting process. The lower panel shows the model residuals.*

Cluster	Annuli	Parameters (+PSF)	Free parameters (+PSF)
Abell 1413	10	340+216	70+108
Abell 963	7	238+144	49+72
Abell 2390	4	136+72	28+36
Abell1835	6	204+120	42+60
MS2137.3-2353	3	102+48	21+24
MACSJ0744.9+3927	5	170+96	35+48
ClJ1226.9+3332	4	136+72	28+36

Table 5.3: *Overview of the numbers of annuli considered for each galaxy cluster, total numbers of model parameters, and the numbers of parameters allowed to vary when fitting a model to the spectra. Applying the correction for the eventual PSF smearing adds many extra parameters to the fit. Those are linked to the original cluster's parameters.*

Table 5.3 shows an overview of the number of annuli considered for each galaxy cluster and the model parameters of the spectral fitting.

Figure 5.2 presents the spectra and folded model of Abell 1413 with the spectra from 10 annuli fit simultaneously. The energy interval 1.2-1.9keV dominated by the X-ray fluorescent background is not included in the fitting process.

5.4.1 PSF CORRECTION

To account for the effects of the finite PSF of XMM-Newton we use a modification of the XMM-ESAS task `arfgen`. The modified version of `arfgen` accounts for the cross-talk due to X-rays detected in one region that are emitted in another. This effect is in particular relevant in clusters presenting cool cores with strong temperature gradients, and can affect the results of the spectral fit.

The cross-talk between adjacent annuli is accounted in XSPEC version 12 as an additional model component with the parameters linked to the cluster spectral fit.

In practice new ancillary response files `ARF` are created considering the cross-talk between neighboring annuli. For two neighboring annuli, e.g. annulus one and two, `arfgen` is set to consider the contribution from annulus one in annulus two. The command returns the effective area in annulus two coming from the PSF overflow of flux from annulus one.

New `ARF` files considering the cross-talk are created for every annulus and its adjacent annuli. That means each annulus now has two extra `ARF` files (with exception of the innermost and outermost annuli having only one neighboring annulus each and therefore only one extra `ARF` file). Each extra `ARF` file is added to the respective data group with an additional model.

$$S_{psf} = N_H * T_c \tag{5.3}$$

Equation 5.3 represents the additional model components, an absorbed thermal model with parameters linked to the respective annulus spectral model.

Using as an example the case of the cluster Abell 1835, with eight annuli, 14 extra models accounting for the possible effects of the PSF smearing are added to the original spectral model presented by equation 5.1. Each extra model has five parameters that are linked to the values of the absorbed thermal component representing the galaxy cluster.

Figure 5.3 shows the effect of the correction on the temperature profile of Abell 1835. For wide annuli, the contribution from the cross-talk is expected to be small.

The possible effects of the PSF smearing was considered for all clusters in the sample with results very similar to those illustrated in figure 5.3.

5.4.2 DEPROJECTED TEMPERATURE PROFILES

The observed X-ray emission in an annulus is a superposition of gas shells of potentially different temperatures. The spectral fitting is therefore affected by the projection effect that each shell in the line of sight has in the cluster spectrum. To account for this effect a deprojection technique is applied to the spectral model.

The spectra, response matrices and quiescent particle background files for all annuli are loaded to XSPEC and fit simultaneously to the same model used for the projected

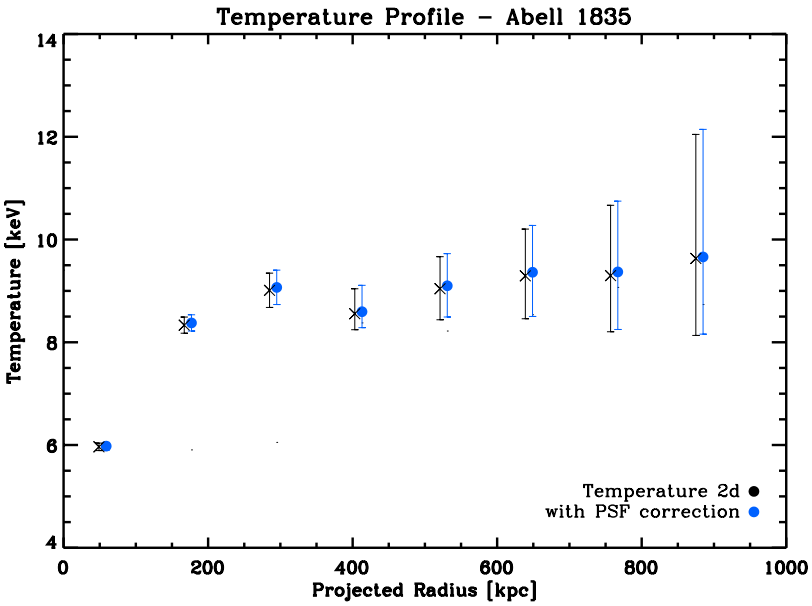

Figure 5.3: *Effect on the temperature profile of the PSF correction applied to Abell 1835. The effect is barely significant. The offset in the projected radius positions are purely for visual purposes.*

temperature profile, but now combined with the XSPEC mixing model `projct`.

The XSPEC convolution model `projct` accounts for projection effects and is used to deproject the profiles. The spectra extracted from a series of concentric annuli are fit simultaneously while `projct` performs a 3D to 2D projection of spherical shells onto circular annuli.

The `projct` model adds three fixed parameters for each data group in use, which are used to define the inner boundary of the region being deprojected. In this study the inner boundary considered is simply the center of the cluster. In this way the contribution of all shells are considered.

Even though many of the parameters are fixed to known values or linked, it can be difficult to obtain proper convergence of the now deprojected spectral model. Careful attention to the spectral fitting is necessary to prevent the model from diverging or stopping at a local minimum.

To minimize the number of free parameters of the deprojected model, the metal abundance values are set and fixed to the values resulting from the projected model.

5.4.3 Effect of background model

To test the effect of the X-ray background in the temperature profiles three different approaches were applied to the spectra within R_{2500} of each galaxy cluster: 1) Both the quiescent particle background spectrum and the explicit model of the cosmic X-ray background, obtained by fitting MOS and RASS spectra simultaneously, were consid-

Cluster	$T_{CXB,QPB}$	$T_{no\ CXB,QPB}$	$T_{no\ CXB,no\ QPB}$
Abell 1413	7.34±0.10	7.34±0.09	8.38±0.09
Abell 963	6.09±0.15	6.08±0.15	6.32±0.14
Abell 2390	9.11±0.44	9.05±0.44	9.57±0.43
Abell1835	7.44±0.08	7.41±0.08	8.01±0.08
MS2137.3-2353	4.18±0.10	4.20±0.10	4.47±0.14
MACSJ0744.9+3927	7.72±0.42	7.68±0.39	11.59±0.71
ClJ1226.9+3332	12.36±0.94	12.39±0.91	16.14±1.14

Table 5.4: *Effect of the X-ray background on the determination of the average temperature of the galaxy clusters. The temperature $T_{CXB,QPB}$ is obtained by fitting the cluster's spectra considering both the quiescent particle background and the cosmic X-ray background, the $T_{no\ CXB,QPB}$ by considering only the quiescent particle background and no cosmic X-ray background, and the $T_{no\ CXB,no\ QPB}$ without considering any background. The errors reported are computed considering 68% confidence.*

ered when fitting the cluster's spectra. 2) The quiescent particle background is subtracted but no explicit model describing the cosmic X-ray background was included in the spectral fit; and 3) No background was considered.

The inclusion of an explicit model of the cosmic X-ray background has negligible effect in the resulting average temperature values for the systems studied and the energy range of 0.7 keV to 7.0 keV considered. The best fit values for the temperatures are the same for all clusters whether or not the cosmic X-ray background model is considered.

While the cosmic X-ray background seems to have no effect in the spectral fit within R_{2500}, the consideration of the quiescent particle background does affect the temperature results significantly. To not consider the quiescent particle background results in a higher value for temperatures of all galaxy clusters, with the largest effect being observed in the galaxy clusters at the highest redshifts.

The effect of the X-ray background in the determination of the cluster's average temperatures is not the same observed in the radial analysis when deriving the temperature profiles. The cosmic X-ray background appears to have little effect in the innermost temperature bins but does affect the temperatures at larger radii, where the cluster emission is not as strong.

The best fit average temperature values within R_{2500} obtained by fitting a model to the cluster spectra considering both the quiescent particle background and the cosmic background, only the particle background and no cosmic X-ray background, and not considering any background are listed in table 5.4.

Figure 5.4 shows the average gas temperature within R_{2500} for all clusters obtained by applying the different background approaches.

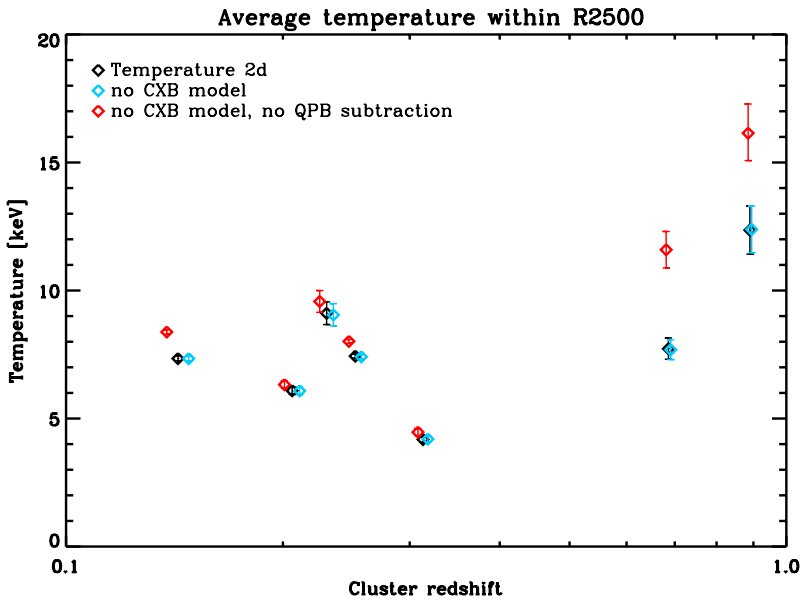

Figure 5.4: *Effect of the cosmic X-ray background model and the quiescent particle background spectra in the resulting average temperature of each galaxy cluster. The resulting temperatures are systematically higher when the particle background is not considered in the spectral fitting procedure.*

5.4.4 Metal abundance

The metals produced by stars in galaxies member of the clusters are kept within the cluster's gravitational potential. The metal abundance can be determined from the emission lines of heavy elements in the spectra. X-ray spectroscopy is a powerful tool for analyzing the metal abundance of the intra cluster gas.

In this study, the average metal abundances and profiles for each galaxy cluster are obtained through the spectral analysis. Studies of the chemical abundances of nearby clusters yield a typical mean value for the metallicity in clusters of approximately 0.3 $Z_{\odot}$ (Rosati et al. 2002), where $Z_{\odot}$ represents solar metallicity.

The average Fe abundances of the clusters studied here are listed in table 5.2. The metal abundance profiles are shown in figure 5.8.

5.5 Spatial analysis

To better understand the distribution of the X-ray emitting gas, the spatial analysis of the cluster is performed through the use of X-ray imaging.

To perform the spatial analysis, the images extracted from each cluster are used. Chapter 3 describes the procedures used to produce mosaic source images, exposure maps and particle background images by combining the images from the detectors MOS1 and MOS2.

The combined images are studied using the software IDL. The source image is divided by the normalized exposure map and has the particle background image subtracted, generating an image that is free from particle background.

The image created is still affected by other sources of X-ray background other than the subtracted particle background. The cosmic X-ray background affecting the image can not be directly subtracted and has to be modeled.

The subsequent spatial analysis consists of producing an X-ray surface brightness profile, removal of the remaining X-ray background and the derivation of the slope of the gas density through modeling of the X-ray surface brightness profile.

5.5.1 THE SURFACE BRIGHTNESS PROFILE

The surface brightness profile is produced using the particle background free image.

The cluster's image is divided in concentric annuli centered are the cluster's center and with a width of 5 arc seconds. The number of counts within each annulus is divided by the area of the respective annulus, producing a profile of the number of counts per unit of area as a function of the cluster's projected radius.

It is assumed that the errors in the number of counts follow a Poisson distribution and are therefore considered to be the square root of the number of counts. The surface brightness profiles of all the galaxy clusters are shown in figure 5.5.

5.5.2 REMAINING BACKGROUND

Assuming a spherical gas cloud in hydrostatic equilibrium and that the volume density of galaxies follows a King profile (King 1972), the X-ray surface brightness profile can be approximated by a β model (Cavaliere & Fusco-Femiano 1976).

To account for the remaining background, a β model is fit to the extracted X-ray surface brightness profile with a constant added to it.

$$S_X(r) = S_0\left(1 + \left(\frac{r}{R_c}\right)^2\right)^{-3\beta+\frac{1}{2}} + C \ , \tag{5.4}$$

Equation 5.4 describes the β model used to model the X-ray surface brightness profile. $S_X(r)$ is the X-ray brightness as a function of the cluster's projected radius r. S_0 describes the innermost brightness, R_c is the core radius and C is the constant accounting for the remaining X-ray background. The free parameters are S_0, R_c, β and the constant C.

The β model is often a good description of X-ray surface brightness profiles for relaxed systems not hosting a cool core. The central X-ray excess is one of the first pieces of evidence of cooling flows in galaxy clusters (Jones & Forman 1984), where the standard β model underestimates the brightness in the central regions.

Cluster	β	R_c	C	χ^2/D.O.F.
Abell 1413	0.56 ± 0.01	33.65 ± 0.80	0.030 ± 0.002	175.86/145
Abell 963	0.54 ± 0.01	22.36 ± 0.64	0.109 ± 0.003	47.14/66
Abell 2390	0.44 ± 0.01	10.55 ± 0.70	0.100 ± 0.006	90.93/61
Abell1835	0.74 ± 0.01	43.50 ± 1.04	0.101 ± 0.002	53.83/54
MS2137.3-2353	0.69 ± 0.02	12.54 ± 0.41	0.110 ± 0.002	32.00/56
MACSJ0744.9+3927	0.55 ± 0.01	10.71 ± 0.36	0.140 ± 0.002	28.98/46
ClJ1226.9+3332	0.66 ± 0.02	15.53 ± 0.71	0.124 ± 0.002	42.52/56

Table 5.5: *The best fit parameters obtained by fitting a β model to the X-ray surface brightness profile of each galaxy cluster. Errors are computed considering 68% confidence. R_c listed in arcseconds and C listed in counts/arcsec^2.*

Variations of the original β model have been proposed, e.g., a double β model with a power law component to account for the brighter center Roncarelli et al. (2006). In this study a single β model was fit to the profile. In cases where central X-ray excess was present the model was fit without considering the innermost part of the profile. The best fit values of the parameters are listed in table 5.5.

One of the motivations for fitting a β model is to remove the excess X-ray background that could not be subtracted by using the particle background image. To do that, it is necessary to constrain the constant C added to the model.

The best-fit value obtained for the constant C is subtracted from the original surface brightness profile to create a background subtracted X-ray brightness profile. Figure 5.5 shows the original surface brightness profile, the best fit β model and the final, background subtracted, surface brightness profile.

The best fit parameters resulting from fitting a β model to X-ray surface brightness profiles are considered in the derivation of the total masses of the galaxy clusters, described in chapter 6.

5.6 RESULTS

The results from the spectral fit within R_{2500} are listed in table 5.2. Both the average temperatures and metal abundances are listed. The errors reported are computed at 68% confidence.The average temperatures are consistent with the results reported by Allen et al. (2008).

The temperature profiles obtained by performing the radial analysis are shown in figure 5.6. Both the projected (2_D) and deprojected (3_D) temperature profiles derived are compared to the results reported by Allen et al. (2008) using Chandra observations.

The fit for the clusters radial analysis vary in quality and the values of χ^2 and degrees of freedom are listed in table 5.6. The good fit indicates that the assumption of an isothermal plasma within each shell describes the system well. A good fit is expected

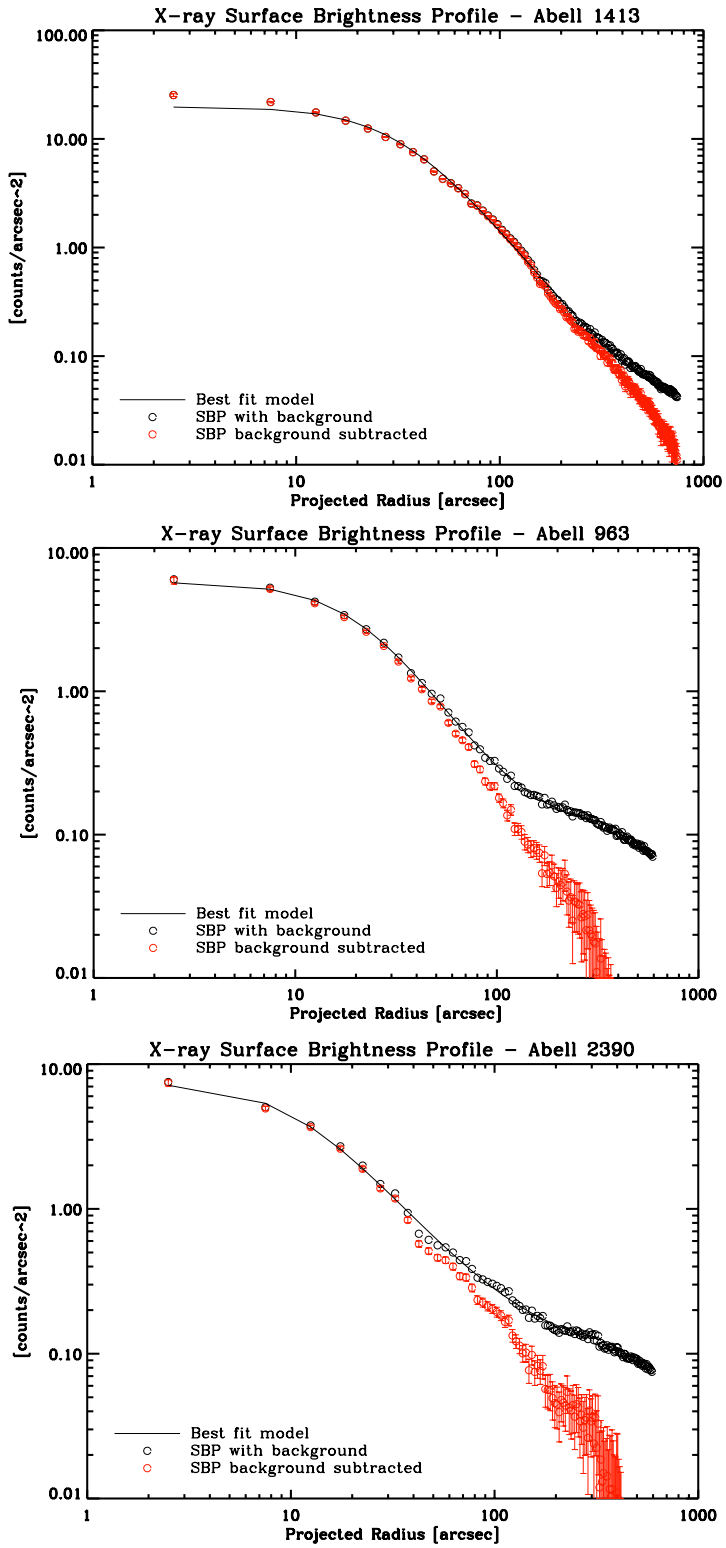

Figure 5.5: *X-ray surface brightness profile of the clusters Abell 1413, Abell 963 and Abell 2390, showing the profile with residual background (black circles), the best fit β model (black line) and the final profile with the residual background subtracted (red circles). The error bars (poisson) in the original profile (black) are not included for visual purposes. Figure continues.*

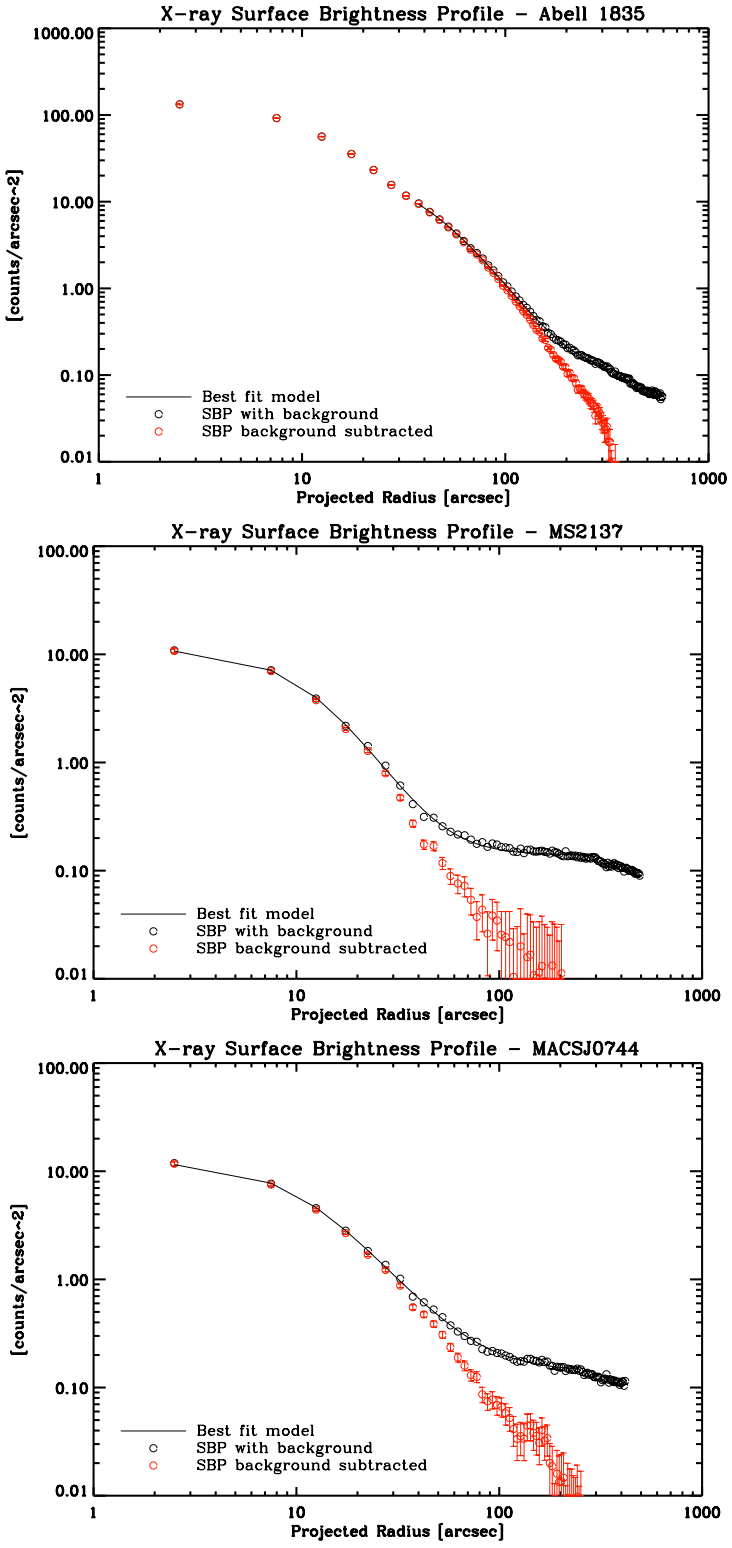

Figure 5.5 *continued, X-ray surface brightness profile of the clusters Abell 1835, MS2137.3-2353 and MACSJ0744.9+3927. Figure continues.*

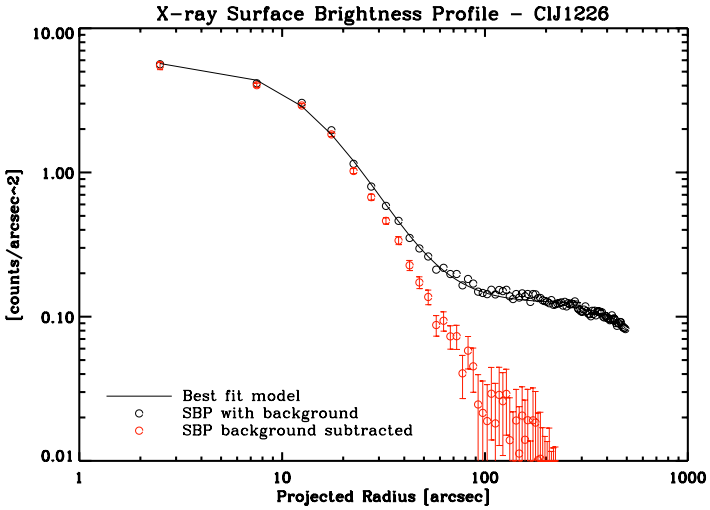

Figure 5.5 *continued, X-ray surface brightness profile of the cluster ClJ1226.9+3332.*

Cluster	Annuli	$2_D\ \chi^2$	2_D d.o.f.	$3_D\ \chi^2$	3_D d.o.f.
Abell 1413	10	6052.01	7382	6114.79	7402
Abell 963	7	4490.08	5166	4514.27	5180
Abell 2390	4	2683.52	2952	3209.67	3701
Abell 1835	6	5141.59	5904	5271.64	5920
MS2137.3-2353	3	2534.31	2952	2543.86	2960
MACSJ0744.9+3927	5	2677.87	3692	2679.90	3701
ClJ1226.9+3332	4	2259.15	2952	2265.77	2961

Table 5.6: *Fit quality based on χ^2 test for the projected (2_D) and deprojected (3_D) spectral models. The values of χ^2 and degrees of freedom (d.o.f.) obtained from the best fit are listed.*

to be particularly difficult to achieve for systems with only a few bins to describe the clearly non isothermal clusters.

The possible effect of the PSF smearing was considered. The PSF correction is barely significant for all systems analyzed in this study. The correction would probably have a larger impact if the annuli size was smaller. Even for the clusters hosting a cool core, with the resolution of the data in use, the effect of the correction is very small.

The metal abundance profiles were derived from the spectral fitting. For some of the outer annuli, the values of the metal abundance is unconstrained, in those cases the value of metal abundance is linked to the value of the abundance of the neighboring annulus. The metal abundance profiles of the seven galaxy clusters are shown in figure 5.8.

The temperature and metal abundance are direct outputs from the spectral fits while the density is derived from the normalization parameter of the APEC model. The nor-

malization parameter K is based on the angular size distance, redshift and the integrated cluster emissivity EI over the volume V of the cluster.

$$K = \frac{10^{-14}}{4\pi(d_A(z+1))^2} \int n_e n_H dV, \tag{5.5}$$

where

$$EI = \int n_e n_H dV \ . \tag{5.6}$$

Considering the condition of the X-ray emitting gas, as being described as of low density, hot and fully ionized plasma, the average electron density $\langle n_e \rangle$ of each shell is calculated assuming that the n_e and hydrogen number density n_H are related so that $n_e \approx 1.2 n_H$.

$$\langle n_e \rangle = \left(\frac{1.2EI}{V} \right)^{\frac{1}{2}} \tag{5.7}$$

The average gas density in each shell is derived by converting the electron number densities into mass densities, considering the gas as a fully ionized plasma.

$$\langle \rho_{gas} \rangle = \mu m_H n_{gas} = 1.92 \mu m_H n_e \tag{5.8}$$

The density profiles derived are shown in figure 5.9.

5.7 Discussion

This chapter presented the results from spectral fitting. The average properties of the seven galaxies clusters were derived together with the radial profiles.

A correction for eventual PSF smearing was considered and the results show it is a nearly negligible effect for the cases studied. The results considered for further analysis are the ones with the correction applied.

It was shown how the different approaches deal with the background subtraction and modeling, and how they affect the result of spectral fitting. It is clear that improper consideration of the background contamination can introduce systematic errors in the temperature profiles.

The average temperature and deprojected profiles are compared to the results reported by Allen et al. (2008) using Chandra data. Both the average values of the temperature and profiles from Chandra are systematically higher than the values obtained in this study. The data analysis performed in Allen et al. (2008) uses an older version of Chandra calibration and studies by Reese et al. (2010) have shown that the use of the old calibration results in values of the temperature on average 10% higher than the most recent calibration would provide.

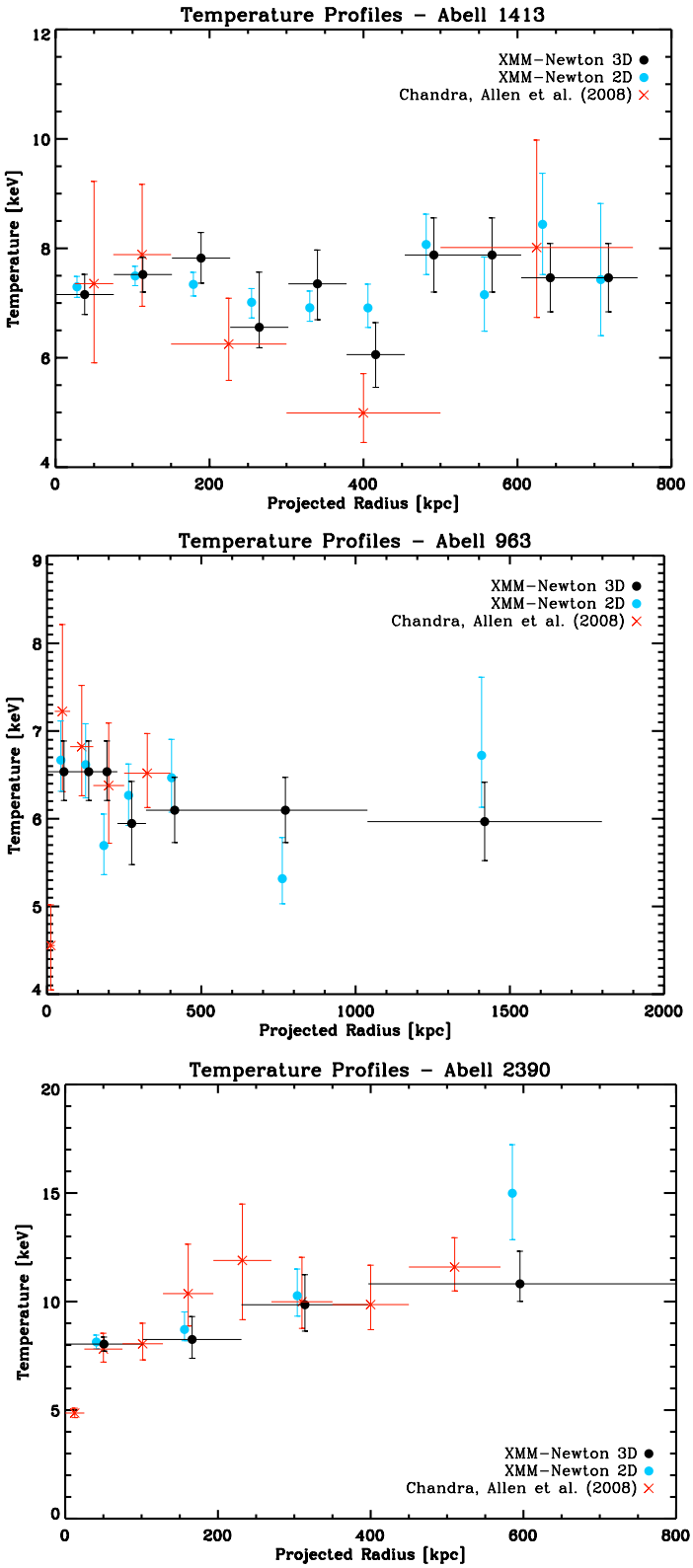

Figure 5.6: *Comparison between the projected (2d, in blue) and deprojected (3d, in black) temperature of obtained by spectral analysis of XMM-Newton observations and the Chandra deprojected profiles (red) from et al. Allen (2008). Chandra values of the temperatures are reduced by 10%. The results for the clusters Abell 1413, Abell 963 and Abell 2390 are presented. Figure continues.*

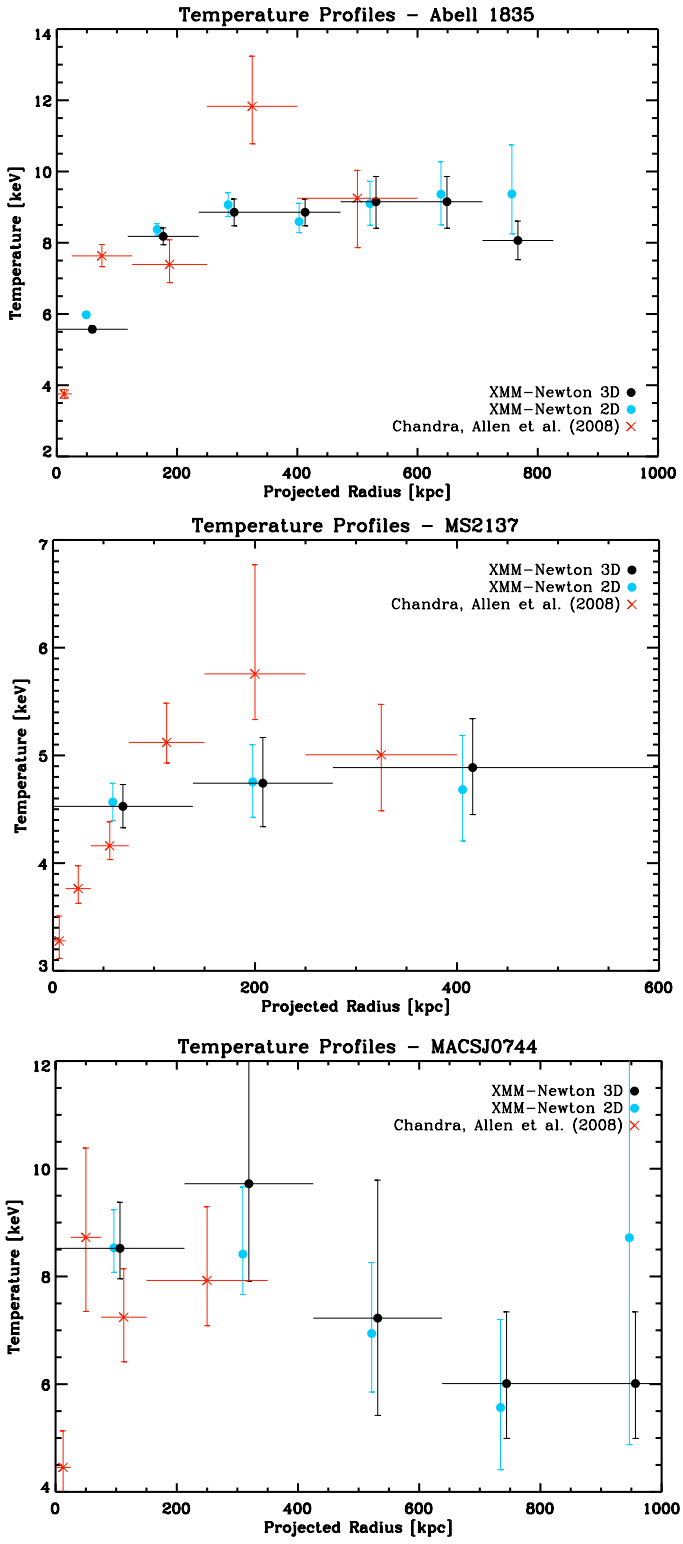

Figure 5.6 *continued, temperature profiles of the clusters Abell 1835, MS2137.3-2353 and MACSJ0744.9+3927. Figure continues.*

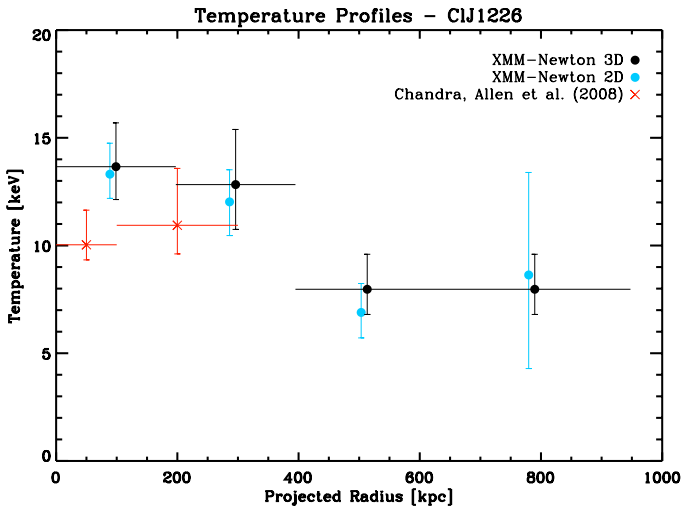

Figure 5.6 *continued, temperature profiles of the cluster ClJ1226.9+3332.*

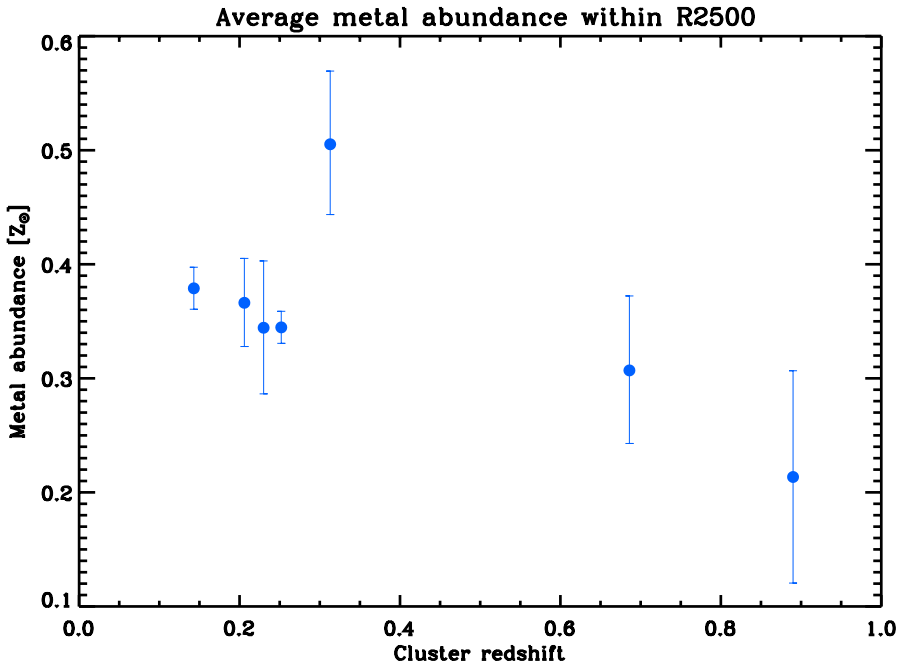

Figure 5.7: *Average metal abundance within radius R_{2500} of each galaxy cluster. The average metal abundances are shown as a function of the cluster redshifts.*

The temperature results obtained in the present analysis do agree with the reported Chandra values if the Chandra temperatures are reduced by 10%. The only exception is the galaxy cluster MS2137.3-2353 which even considering the 10% correction still shows a significant lower temperature profile. The possible explanation is the residual soft

proton contamination affecting the observation of this system, and therefore, changing the X-ray temperature measured.

The values of gas temperature and density obtained in this analysis are used to derive the clusters mass profiles, described in chapter 6.

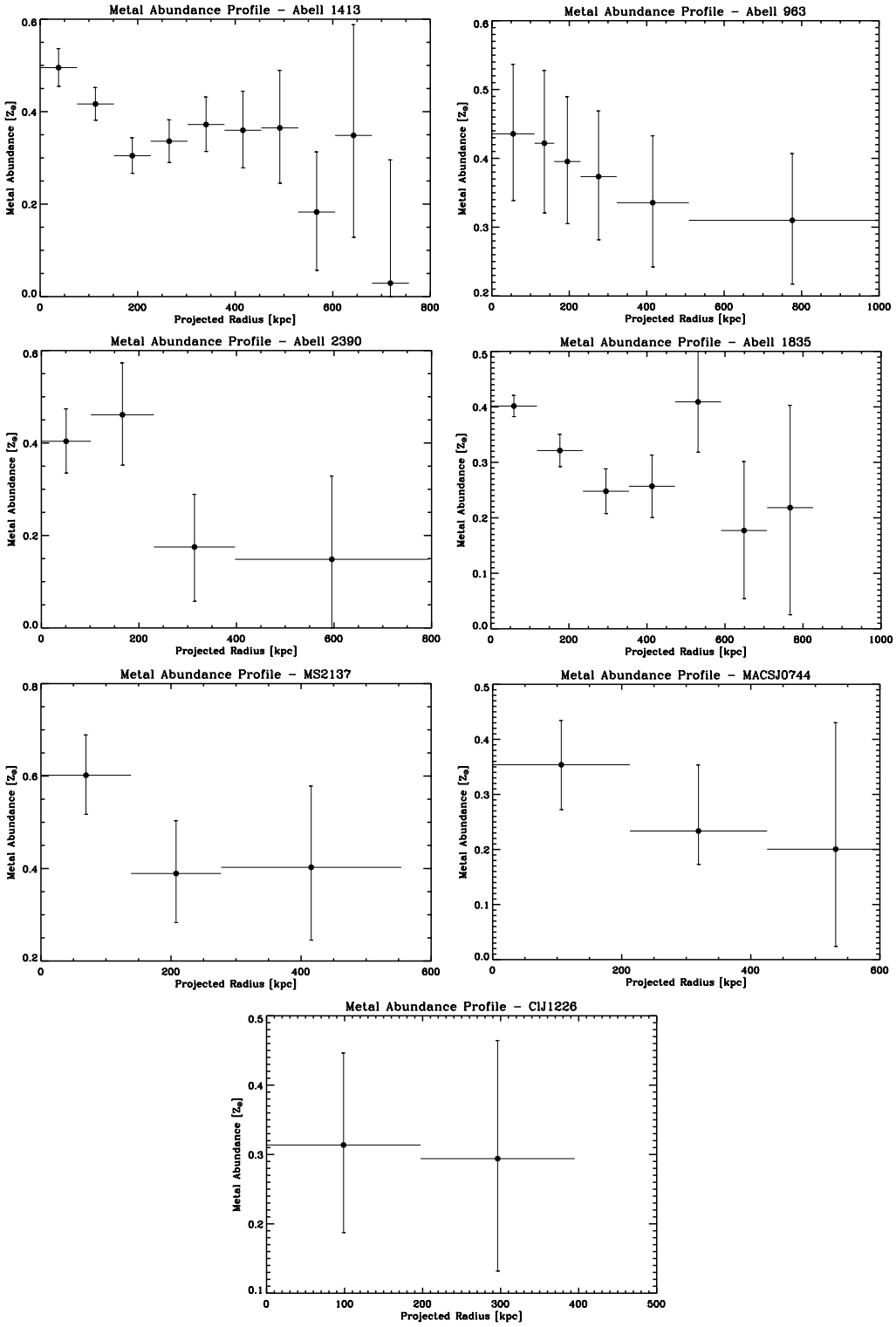

Figure 5.8: *Metal abundance profiles obtained from spectral analysis.*

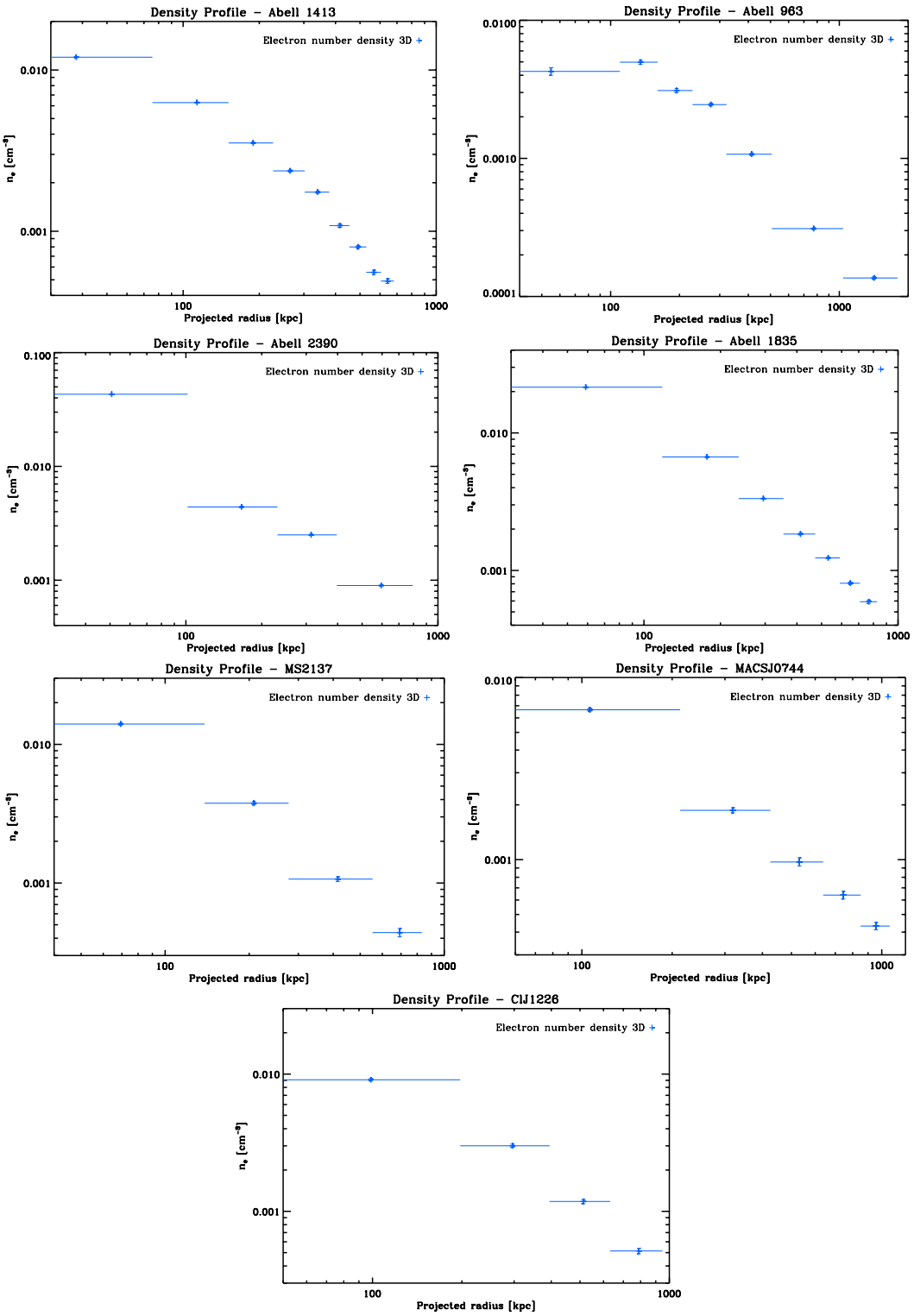

Figure 5.9: *Deprojected (3D) gas density profiles.*

6

MASS PROFILES

"Misura ciò che è misurabile,
e rendi misurabile ciò che non lo è."

Galileo Galilei (1564-1642)

ABSTRACT – *This chapter presents the mass distributions of the seven galaxy clusters included in this study. The mass profiles are derived under the assumptions of spherical symmetry and hydrostatic equilibrium. The total cluster masses and gas masses within R_{2500} are calculated by taking different assumptions on the distributions of the gas density and temperature. The total mass profiles, derived model independently, are fit with a NFW model with the best fit parameters considered in the derivation of the clusters total masses, concentration parameters c_{2500}, and its relation to the clusters masses and redshift. The gas mass fractions are computed assuming both a model independent approach and a NFW model to obtain the total masses of the clusters.*

6.1 INTRODUCTION

Precise measurements of the mass profiles of galaxy clusters are essential for the study of the mass distribution in the Universe. The analysis of XMM-Newton observations described in chapter 5 allows for the derivation of the mass distribution in each of the seven galaxy clusters included in this sample under the assumption of hydrostatic equilibrium. The gas temperature and density profiles obtained from spectral analysis are combined to obtain the mass profiles of the clusters and the total masses within R_{2500}.

6.2 THE TOTAL CLUSTER MASS

The cluster total mass includes both baryonic matter and dark matter. Most of the baryonic matter in a galaxy cluster is in the form of the hot X-ray emitting gas (e.g., White et al. 1993; David et al. 1995; Fukugita et al. 1998; Evrard 1997). Under the assumption of spherical symmetry and hydrostatic equilibrium of the gas within the cluster potential it is possible to obtain the cluster total mass (Sarazin 1988) using the gas temperature

and density derived from X-ray observations. For a spherical system the equation of hydrostatic equilibrium is

$$\frac{d\,P}{d\,r} = -\frac{G\,M(<r)\,\rho_{gas}(r)}{r^2} \quad . \tag{6.1}$$

In equation 6.1, P is the gas pressure, $M(<r)$ is the total mass enclosed within a radius r, $\rho_{gas}(r)$ is the gas density at radius r and G is the gravitational constant.

The gas trapped in the cluster potential has very high temperatures and low density therefore it is well described as an ideal gas. In this case, the pressure can be written as

$$P = n\,k_B\,T \quad . \tag{6.2}$$

Equation 6.2 is the ideal gas law, where n is the particle number density, k_B is the Boltzmann constant and T is the gas temperature. The gas density is assumed to be

$$\rho_{gas} = \mu m_H n \approx 1.92 \mu m_H n_e \quad . \tag{6.3}$$

Where μ is the gas mean molecular weight, m_H is the hydrogen mass and n_e the electron number density, assuming a fully ionized plasma with the particle number density $n = n_e + n_H + n_{He} \approx 1.92 n_e$. Using equation 6.3, equation 6.2 takes the form

$$P = \frac{\rho_{gas}\,k_B\,T}{\mu\,m_H} \quad . \tag{6.4}$$

Combining equations 6.1 and 6.4 the cluster total mass within a radius r_j is given by

$$M(<r_j) = -\frac{k_B T_j r_j}{G\mu m_H}\left(\frac{d\ln\,\rho_{gas,j}}{d\ln r_j} + \frac{d\ln T_j}{d\ln r_j}\right) \quad . \tag{6.5}$$

The information necessary to calculate the cluster total mass using equation 6.5 is obtained from the XMM-Newton spectral analysis, described in chapter 5. Both the gas temperature and density profile as a function of the projected distance from the cluster center are used to obtain the cluster total mass. The radius r_j is the distance from the cluster center to the center of each cluster shell for which the gas temperature and density are derived.

To compute the cluster total mass within a certain radius it is necessary to calculate the gradients of the gas temperature and density at that radius. That is done using the values of temperature and density in the neighboring shells.

$$\frac{d\ln\rho_{gas,j}}{d\ln r_j} = \frac{\ln\rho_{gas,j+1} - \ln\rho_{gas,j-1}}{\ln r_{j+1} - \ln r_{j-1}} \tag{6.6}$$

$$\frac{d\ln T_j}{d\ln r_j} = \frac{\ln T_{j+1} - \ln T_{j-1}}{\ln r_{j+1} - \ln r_{j-1}} \tag{6.7}$$

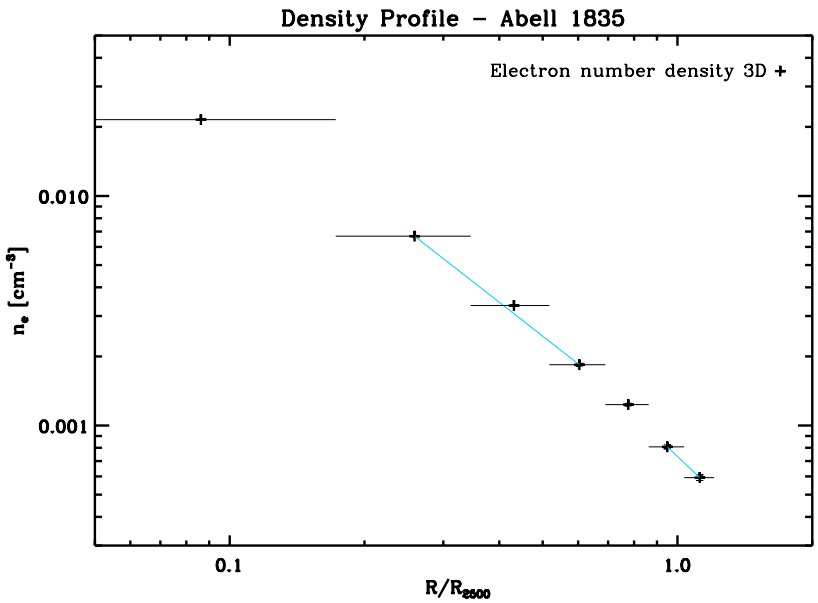

Figure 6.1: *Gas density profile of the cluster Abell 963 with the blue line connecting the data points used for the approximation of the gradient. For the inner density bins the two neighboring points are considered. For the innermost and outermost the nearest neighboring point is considered.*

Equations 6.6 and 6.7 are used as an approximation of the function derivatives at r_j. For the innermost and outermost shell the gradient is calculated using the one neighboring shell.

$$\frac{d\ln\rho_{gas,j}}{d\ln r_j} = \frac{\ln\rho_{gas,j} - \ln\rho_{gas,j-1}}{\ln r_j - \ln r_{j-1}} \tag{6.8}$$

$$\frac{d\ln T_j}{d\ln r_j} = \frac{\ln T_j - \ln T_{j-1}}{\ln r_j - \ln r_{j-1}} \tag{6.9}$$

The main limitation in calculating the gradient using equations 6.6-6.9 is the number of annuli. The number of annuli, and therefore, how well the temperature and density profiles can be constrained, depends on the quality of the observation available. The greater the number of X-ray photons observed, the greater the number of annuli, and therefore, the better the quality of the mass measurement derived.

In figure 6.1 the deprojected density profile of Abell 1835 is presented with an example of data points considered for computing the gradient of the density.

To calculate the uncertainty in the gradient the gas density and temperature are assumed to be independent, the errors are therefore added in quadrature.

6.2.1 GAS DENSITY GRADIENT FROM THE SURFACE BRIGHTNESS PROFILE

To compute the cluster total mass within a defined radius using equation 6.5 both the gradient of the gas temperature and density are used. The equations 6.6-6.9 describe the calculation of the gradients by fitting a straight line between adjacent data points. Another approach is to fit a parametric model to the density profile and use it to derive the gradient of the gas density, used in equation 6.5.

The X-ray emissivity scales as the gas density squared. Under the assumption of spherical symmetry, the gas distribution in the galaxy cluster can be derived from the analysis of the X-ray surface brightness profile.

$$\rho_{gas}(R) \propto \left(1 + \left(\frac{R}{R_c}\right)^2\right)^{-\frac{3}{2}\beta} \tag{6.10}$$

The β model presented in equation 6.10 describes the gas density as a function of distance from the cluster's center R. The values of β and R_c used in equation 6.10 are obtained by fitting a β model to the X-ray surface brightness profile, described in chapter 5.

Applying the values of the best fit parameters of the β model to equation 6.10 and calculating the derivative of density model as a function of the radius allow for the determination of the gradient of the density, and equation 6.5 takes the form:

$$M(< r_j) = -\frac{k_B T_j r_j}{G\mu m_H}\left(-\frac{3\beta r_j^2}{R_c^2 + r_j^2} + \frac{d\ln T_j}{d\ln r_j}\right) \quad . \tag{6.11}$$

6.3 DEFINING R_{2500}

The value of R_Δ is defined to be the radius at which the mean enclosed cluster mass density is equal to Δ times the critical density of the Universe at the cluster's redshift.

$$\rho_{crit}(z) = \frac{3H(z)^2}{8\pi G} \tag{6.12}$$

In equation 6.12, ρ_{crit} is the critical energy density of the Universe at the cluster observed redshift z, H is the Hubble parameter and G the gravitational constant. The cluster mass within a radius r_Δ can be written as a function of the critical density.

$$M_\Delta = \frac{4}{3}\pi r_\Delta^3 \rho_{crit}\Delta \tag{6.13}$$

In equation 6.13, Δ is simply the overdensity contrast to the critical density of the Universe.

In this study, the overdensity considered is 2500. The value of the radius R_{2500} is dependent on the cluster density and the critical energy of the Universe at the cluster's redshift, its value is, therefore, particular for each cluster.

The values of redshift and radius R_{2500} adopted are reported by Allen et al. (2008) and listed in table 6.1.

6.4 TOTAL CLUSTER MASS WITHIN R_{2500}

To calculate the total masses of the galaxy clusters enclosed within R_{2500}, equation 6.5 is used. The values of the temperatures and gradients of the gas density and temperature measure at R_{2500} are considered.

$$M_{2500}^{obs} = -\frac{k_B T_{2500} R_{2500}}{G\mu m_H}\left(\frac{d\ln\ \rho_{gas,2500}}{d\ln r_{2500}} + \frac{d\ln T_{2500}}{d\ln r_{2500}}\right) \tag{6.14}$$

The mass M_{2500}^{obs} calculated through equation 6.14, depends only on the temperature and gradients of temperature and gas density measured at R_{2500}.

The value of the gas temperature precisely at R_{2500} is not available directly from the spectral analysis. The temperature at R_{2500} is obtained by a linear interpolation of the neighboring temperature data points. The values of the clusters temperatures at R_{2500}, T_{2500}, are listed in table 6.1.

The gradient of the gas density is obtained by two different approaches: 1) by a interpolation in the logarithmic scale of the neighboring density data points obtained from the spectral analysis, and 2) by assuming a β model to the gas distribution within the cluster potential.

The total cluster mass M_{2500} is computed in four distinct ways:

1) Model independent, assuming no parametric model for the temperature and density distributions;

2) model dependent, assuming no parametric model for the temperature distribution, but assuming that the gas density is well described by a β model;

3) Isothermal, model independent, assuming the gas to be isothermal and no parametric model for the gas density;

4) Isothermal, model dependent, assuming the gas to be isothermal and a β model describing the gas density.

For the model independent approach, equations 6.5-6.9 are used to compute the total cluster mass M_{2500}^{obs}, based on the measured values of gas temperature and density obtained from the spectral analysis, described in chapter 5.

For the model dependent approach, equation 6.5 is used together with equations 6.7 and 6.9 to calculate the temperature gradient, and equation 6.11 is applied to compute

Cluster	redshift	$R_{2500}[kpc]$	$\langle T_{2500}\rangle[keV]$	$T_{2500}[keV]$
Abell 1413	0.143	599^{+17}_{-19}	7.34±0.09	7.76±0.84
Abell 963	0.206	540^{+24}_{-27}	6.09±0.15	6.46±0.64
Abell 2390	0.230	662^{+42}_{-30}	9.11±0.44	10.82±1.15
Abell 1835	0.252	684^{+27}_{-26}	7.44±0.08	8.83±0.76
MS2137.3-2353	0.313	479^{+18}_{-10}	4.18±0.10	4.89±0.45
MACSJ0744.9+3927	0.686	466^{+40}_{-23}	7.73±0.42	8.00±3.09
ClJ1226.9+3332	0.890	521^{+123}_{-54}	12.36±0.94	7.97±1.40

Table 6.1: *Comparison between the average temperature values, $\langle T_{2500}\rangle$, within R_{2500} and the temperature, T_{2500}, derived from the temperature profile at R_{2500}. The values of R_{2500} are from Allen et al. (2008).*

the total cluster mass M^{β}_{2500}.

For the isothermal case, both model independent and model dependent approaches are considered under the assumption that the hot intra cluster gas can be described as a single temperature plasma within R_{2500}.

The results for the clusters total masses obtained from the different approaches are listed in table 6.2. In figure 6.2 the masses for each clusters are plotted as a function of the cluster's redshift.

6.4.1 Assuming an isothermal gas

By assuming that the gas within the intra cluster medium is isothermal, the gradient of the temperature in equation 6.5 is set to zero.

$$M^{iso}_{2500} = -\frac{k_B\langle T_{2500}\rangle R_{2500}}{G\mu m_H}\left(\frac{d\ln\ \rho_{gas,2500}}{d\ln r_{2500}}\right) \quad . \tag{6.15}$$

Equation 6.15 is used to calculate the cluster total mass within R_{2500} under the assumption of isothermal distribution of the X-ray emitting gas. The temperature $\langle T_{2500}\rangle$ is the average temperature of the intra cluster gas obtained by fitting a model to the cluster spectrum, extracted considering the region within R_{2500}, described in chapter 5.

The values of the cluster's average temperatures $\langle T_{2500}\rangle$ within at R_{2500} are listed in table 6.1.

6.5 The mass profiles

To obtain the cluster's total mass profiles, equation 6.5 was applied to each temperature data point and gradients of the temperature and gas density obtained for each cluster annulus.

Because the total cluster mass calculated through equation 6.5 depends only on the temperature and gradients of temperature and gas density measured at an specific ra-

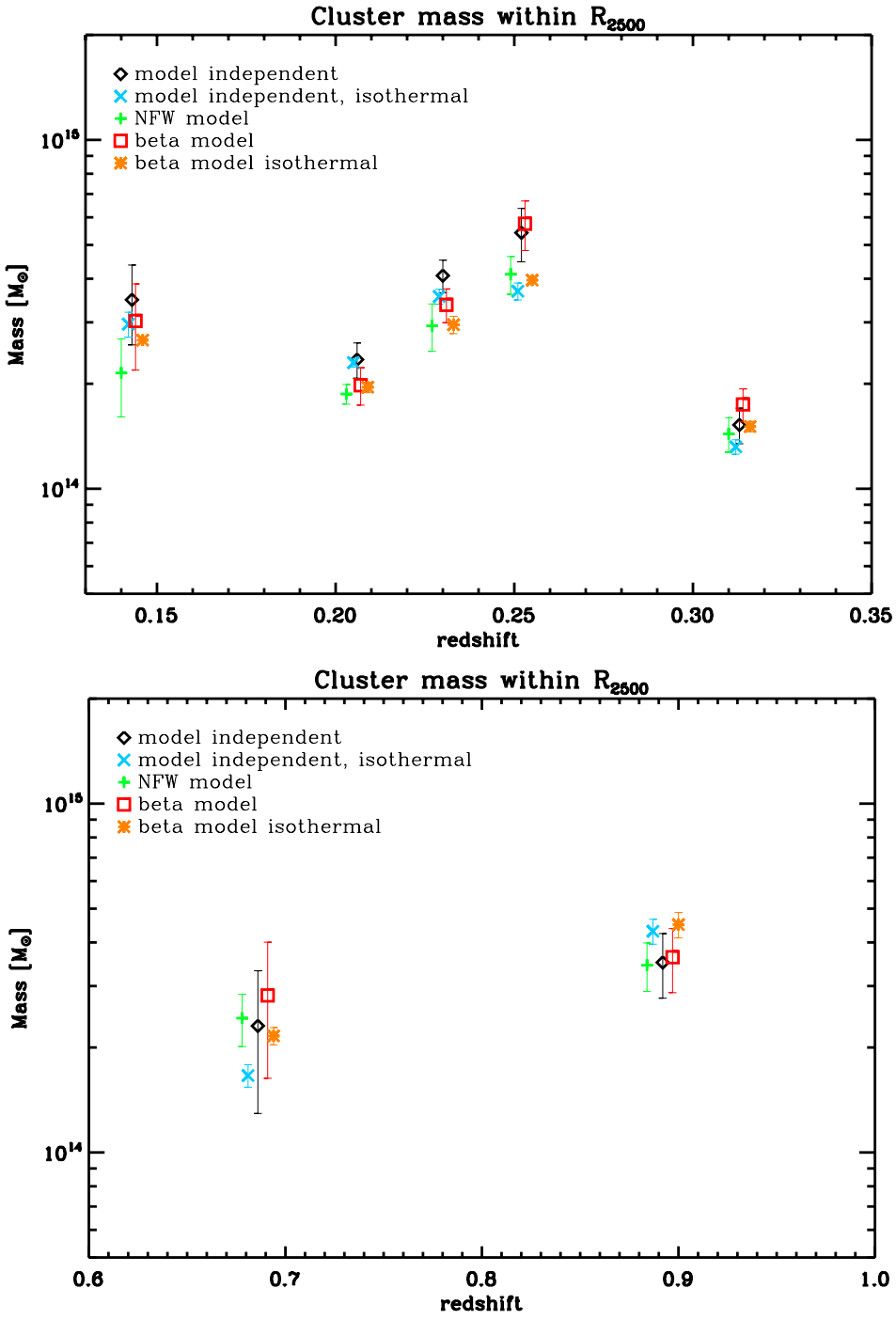

Figure 6.2: *Total cluster mass within R_{2500} calculated for each galaxy cluster taking different approaches. The upper panel shows the results for the clusters at relatively low redshift, while the masses computed for the two highest redshift systems are presented in the lower panel. The plots are separated for visual purposes only.*

Cluster	M_{2500}^{obs}	M_{2500}^{iso}	M_{2500}^{β}	$M_{2500}^{\beta,iso}$	M_{2500}^{NFW}
Abell 1413	3.48±0.90	2.96±0.24	3.03±0.84	2.67±0.46	2.15±0.54
Abell 963	2.35±0.27	2.30±0.07	1.98±0.24	1.95±0.06	1.87±0.12
Abell 2390	4.08±0.44	3.56±0.18	3.37±0.37	2.95±0.17	2.93±0.45
Abell 1835	5.42±0.95	3.68±0.21	5.75±0.93	3.96±0.07	4.12±0.51
MS2137.3-2353	1.52±0.18	1.32±0.06	1.74±0.19	1.51±0.05	1.44±0.16
MACSJ0744.9+3927	2.31±1.01	1.66±0.012	2.82±1.19	2.16±0.12	2.43±0.41
ClJ1226.9+3332	3.51±0.74	4.30±0.35	3.62±0.76	4.49±0.38	4.44±0.54

Table 6.2: *Total cluster mass within radius R_{2500} of each galaxy cluster in the sample calculated from different approaches. The masses are listed in units of $10^{14} M_{\odot}$.*

dius r, it is possible to obtain the cluster total mass within the radius defined as the center of the annulus where the temperature and density are measured.

To produce the mass profiles, the model independent approach was taken with the gradients of the temperature and gas density calculated using equations 6.6-6.9. The total mass profiles of each galaxy cluster are presented in figure 6.3.

6.6 MODELING THE MASS PROFILES

Simulations of structure formation considering cold dark matter predict that the density profiles of dark matter halos, can be approximated by a universal profile (Navarro et al. 1995, 1997).

$$\rho(r) = \frac{\rho_0}{\left(\frac{r}{r_s}\right)\left(1+\frac{r}{r_s}\right)} \tag{6.16}$$

The so-called Navarro-Frenk-White (NFW) profile introduced by equation 6.16 describes the density distribution in dark matter halos, where r is the distance from the cluster center, r_s is the scale radius and ρ_0 is the density at the cluster's center.

To model the observed mass profiles an analytical model for the mass is obtained by integrating equation 6.16 over the cluster's volume.

$$M(<r) = 4\pi\rho_0 r_s^3 \left[\ln\left(\frac{r_s+r}{r_s}\right) - \frac{r}{r_s+r}\right] \tag{6.17}$$

Equation 6.17 is the integrated mass within a enclosed radius r. The observed mass profiles are fit with the NFW integrated mass profile with the central density ρ_0 and the scale radius r_s as free parameters.

The model mass profile is compared with the observed mass profile and the goodness of fit is calculated using the sum over all mass data points.

Cluster	Mass bins	ρ_0 $[\times 10^6 M_\odot kpc^{-3}]$	r_s $[kpc]$	c_{2500}	$\chi^2/_{D.O.F.}$
Abell 1413	9	$2.98^{+2.12}_{-1.16}$	212^{+82}_{-61}	$2.83^{+1.11}_{-0.82}$	37.51 / 7
Abell 963	7	$0.27^{+0.08}_{-0.06}$	770^{+131}_{-108}	$0.70^{+0.12}_{-0.10}$	36.37 / 5
Abell 2390	5	$44.73^{+21.05}_{-14.35}$	72^{+16}_{-13}	$9.25^{+2.13}_{-1.71}$	53.36 / 3
Abell 1835	7	$0.62^{+0.19}_{-0.15}$	628^{+146}_{-111}	$1.09^{+0.26}_{-0.20}$	29.28 / 5
MS2137.3-2353	4	$3.70^{+1.64}_{-1.12}$	174^{+39}_{-32}	$2.75^{+0.63}_{-0.51}$	4.21 / 2
MACSJ0744.9+3927	5	$2.96^{+3.21}_{-1.60}$	255^{+131}_{-81}	$1.83^{+0.95}_{-0.59}$	0.37 / 3
ClJ1226.9+3332	4	$14.03^{+16.54}_{-7.65}$	136^{+63}_{-42}	$3.84^{+2.01}_{-1.23}$	0.17 / 2

Table 6.3: *NFW model best fit parameters.*

$$\chi^2 = \sum_j \left(\frac{M_{obs}(j) - M_{NFW}}{\sigma_{obs}(j)} \right)^2 \tag{6.18}$$

In equation 6.18, M_{obs} is the observed mass profile, M_{NFW} is the analytical mass model and σ_{obs} is the error in the observed mass profile.

For each galaxy cluster mass model, the best fitting parameter values and uncertainties were determined using χ^2 minimization. The 1σ error estimate of the model parameters is defined by the contour where $\chi^2 = \chi^2_{min} + 1$. The contour plots for all seven galaxy clusters analyzed are shown in figure 6.3.

The observed mass profiles, derived in taking a model independent approach, are considered for the NFW fit. Due to the calculation of the gradient of the gas temperature and density considering the neighboring data points, the mass derived for each data point may be slightly correlated to its adjacent mass value but mass data points further away than the immediately adjacent points are not correlated (Voigt & Fabian 2006).

When a model is assumed to describe the distribution of the gas temperature or density, the resulting mass profile has mass values that are correlated. To fit the NFW model using χ^2 statistics to mass data points calculated by assuming a model to the gas temperature or density would be statistically invalid (Voigt & Fabian 2006).

Both the observed mass profiles, obtained by combining the results from the spectral fit and the equation of hydrostatic equilibrium, and the best fit of the NFW mass model, described by equation 6.17, are shown in figure 6.3 .

The best fitting parameters of the NFW model for each galaxy cluster, and the values of χ^2 minimization, are presented in table 6.3.

6.6.1 MODEL MASS WITHIN R_{2500}

In order to directly compare the results and uncertainties between the observed mass profiles, calculated in a model independent approach, and the values obtained by fit-

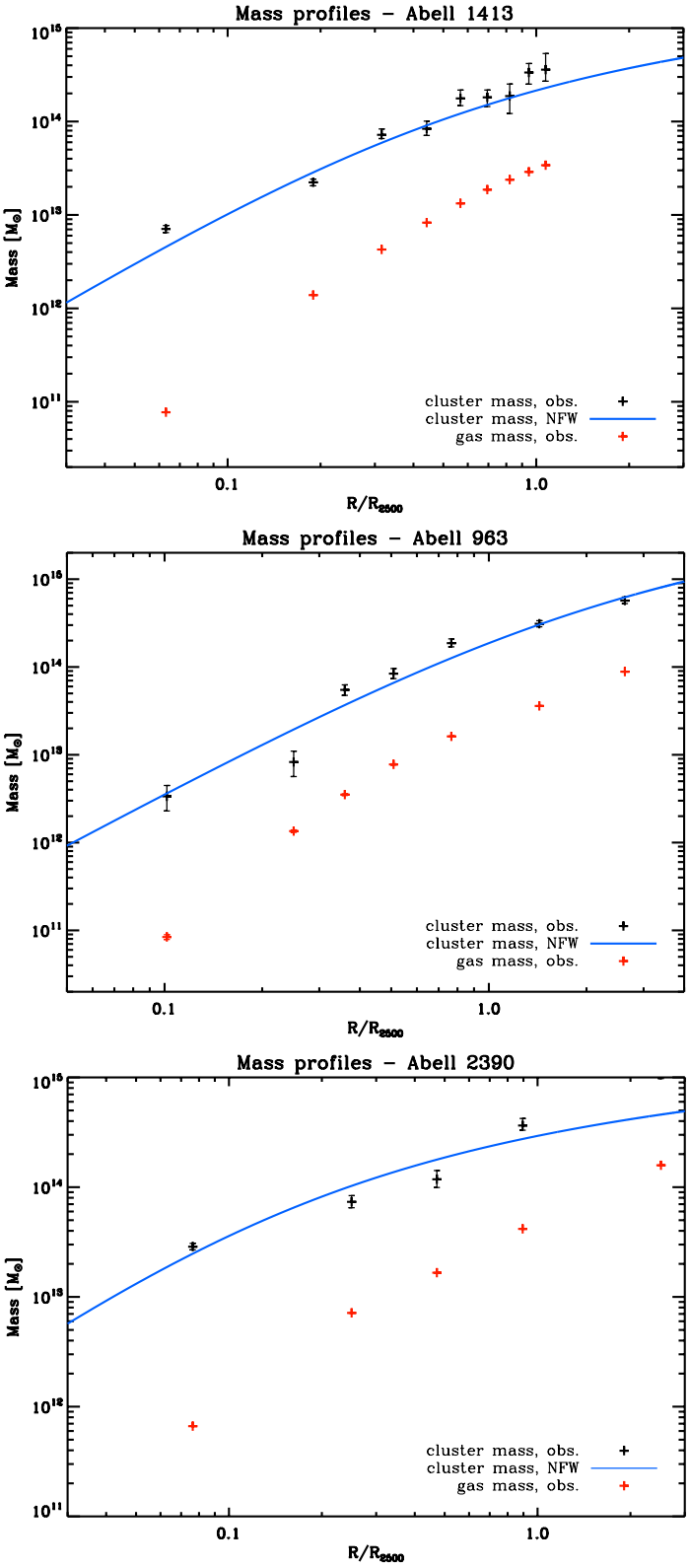

Figure 6.3: *Cluster total mass profiles (black), best fit NFW model (blue) and gas mass profiles (red) of the clusters Abell 1413, Abell 963 and Abell 2390. Figure continues.*

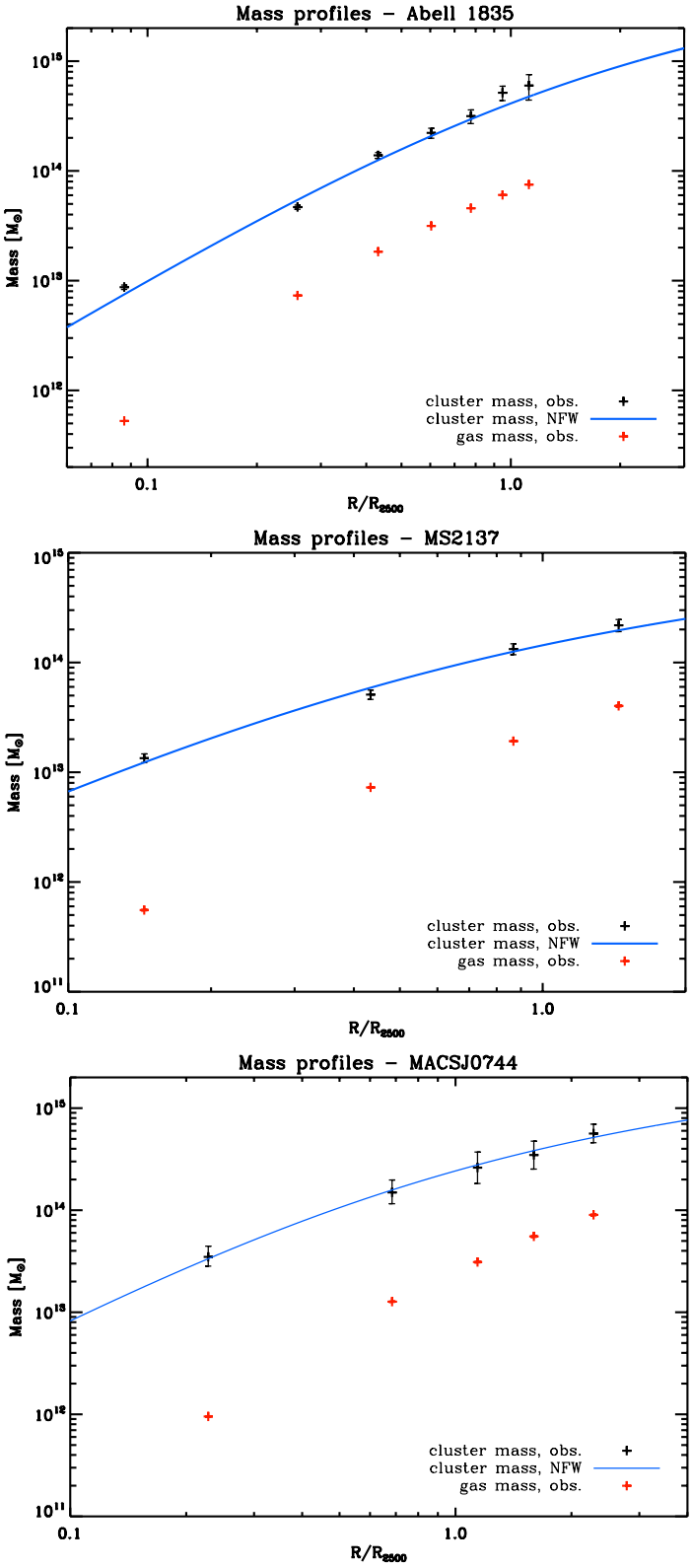

Figure 6.3 *continued, luster total mass profiles (black), best fit NFW model (blue) and gas mass profiles (red) of the clusters Abell 1835, MS2137.3-2353 and MACSJ0744.9+3927. Figure continues.*

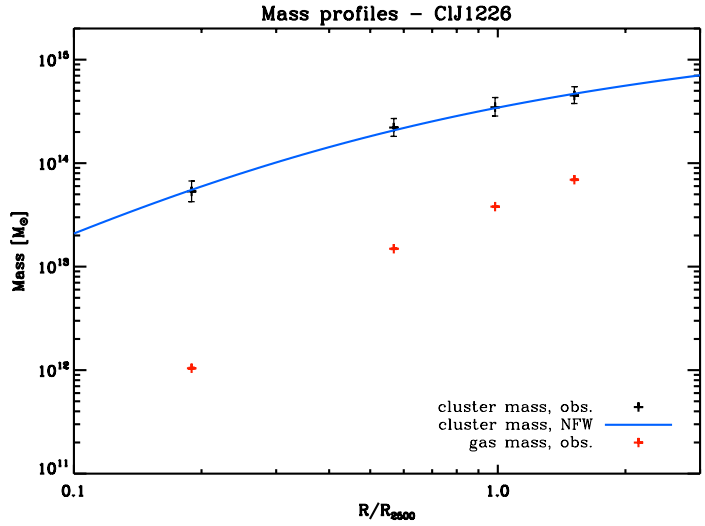

Figure 6.3 *continued, cluster total mass profiles (black), best fit NFW model (blue) and gas mass profiles (red) of the cluster ClJ1226.9+3332.*

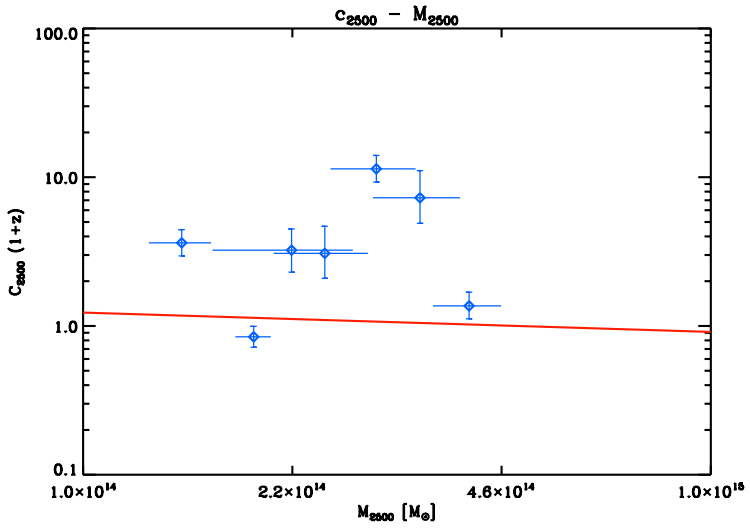

Figure 6.4: *The blue points show the concentration parameter c_{2500} as a function of the cluster's total mass M_{2500} obtained in this study. The red line indicates the mean relation log $c_{2500} = 0.35 - 0.130$ log $(M_{2500}/10^{12} M_{\odot})$ from the N-body simulations of Macciò et al. (2008), based on the WMAP5 cosmology.*

ting a NFW mass model to the observed mass profile, the values of the clusters masses within radius R_{2500} were computed for both methods. The values of the observed masses M_{2500}^{obs} and the masses obtained by fitting a NFW model to the mass profiles, M_{2500}^{NFW}, are listed in table 6.2.

To obtain the mass within R_{2500} from the NFW mass model, the values of R_{2500} and the best fitting parameters are used in equation 6.17.

The two parameters allowed to vary when adjusting the analytical model to the data, ρ_0 and r_s, are highly correlated. To obtain the confidence interval for the mass calculated from the model we take the following approach:

For each combination of ρ_0 and r_s resulting in the same mass value the probability density function is calculated resulting in a Gaussian distribution with the mean value at the mass obtained by the best fitting parameters. The confidence intervals are computed at 68%.

6.6.2 Concentration parameter

An output of the NFW model is the concentration parameter. The concentration parameter, c_Δ, at a given mass, M_Δ, is defined to be the ratio of the radius r_Δ and the scale radius.

$$c_\Delta = \left(\frac{r_\Delta}{r_s}\right) \tag{6.19}$$

In equation 6.19, Δ is the overdensity contrast to the critical density of the Universe. In this study, the overdensity considered is 2500. The value of c_{2500} for each cluster is obtained by dividing R_{2500} by the value of r_s obtained by modeling of the mass profile.

$$c_{2500} = \left(\frac{R_{2500}}{r_s}\right) \tag{6.20}$$

The ΛCDM model makes theoretical prediction for concentrations of the dark matter halos. The concentration parameter c is related to the halo's time of formation. (e.g., Navarro et al. 1997; Bullock et al. 2001; Dolag et al. 2004; Macciò et al. 2008), it is therefore, expected an inverse correlation between the cluster mass and its concentration.

Halos of earlier formation are expected to have a higher concentration (Bullock et al. 2001) as the less massive systems form from a higher density environment than the more massive ones, expected to form recently, from a lower density environment. This relation has been supported by the observation of mass profiles in galaxy clusters (e.g., Schmidt & Allen 2007; Comerford & Natarajan 2007, and references therein). The dark matter halo's concentration is also expected to scale as $(1+z)^{-1}$ (Bullock et al. 2001).

The concentration parameters c_{2500} for this cluster sample are calculated using equation 6.20 and are listed in table 6.3. Figure 6.4 shows the concentration parameter as a function of the cluster total mass and the theoretical prediction $c_{2500} - M_{2500}$ from Macciò et al. (2008).

6.7 Gas mass

The gas mass within each cluster shell is obtained by multiplying the average density derived at that shell to the shell's volume. The average density in each cluster shell and

density profiles are presented in chapter 5.

$$M_{gas,j} = \frac{4}{3}\pi \left(r_i^3 - r_{i-1}^3\right) \rho_{gas,j} \tag{6.21}$$

Using equation 6.21, the gas mass in each cluster shell is computed. The $\rho_{gas,j}$ is the average density within the shell, r_i is the distance from the cluster center to the outer boundary of the shell and r_{i-1} is the distance from the cluster center to the inner boundary of the shell.

To obtain the total gas mass enclosed in a radius r_i the sum of the gas mass in each shell within r_i is calculated.

$$M_{gas}(< r_i) = \sum_{j}^{n} \frac{4}{3}\pi \left(r_i^3 - r_{i-1}^3\right) \rho_{gas,j} \tag{6.22}$$

The integrated gas masses within R_{2500} of the galaxy clusters in this study are listed in table 6.4.

6.8 THE GAS MASS FRACTION

The gas mass fraction is the ratio between the gas mass and the total cluster mass within a defined radius.

$$f_{gas,r_j} = \frac{M_{gas}(< r_j)}{M_T(< r_j)} \tag{6.23}$$

Combining the gas mass profiles and the total cluster mass profiles, the gas mass fraction profiles are obtained using equation 6.23. The gas mass profile of Abell 1835 is shown in figure 6.6.

The gas mass fractions at R_{2500} are calculated for each galaxy cluster using the cluster's gas mass and total mass within R_{2500}.

$$f_{gas,2500} = \frac{M_{gas,2500}}{M_{2500}} \tag{6.24}$$

The results of the integrated gas mass, observed total mass, modeled total mass and the gas mass fractions at R_{2500}, are listed in table 6.4.

The gas mass fractions of each cluster, obtained by considering both the observed masses and the masses derived from the NFW fit, as a function of cluster's redshift, are represented in figure 6.7.

6.9 RESULTS AND DISCUSSION

In this chapter the outputs from spectral and spatial analysis are used to derive the masses of the seven galaxy clusters included in this study.

Cluster	$M_{gas,2500}$ $[\times 10^{13} M_\odot]$	M_{2500}^{obs} $[\times 10^{14} M_\odot]$	M_{2500}^{NFW} $[\times 10^{14} M_\odot]$	$f_{gas,2500}^{obs}$	$f_{gas,2500}^{NFW}$
Abell 1413	3.038±0.028	3.48±0.90	2.15±0.54	0.087±0.022	0.141±0.036
Abell 963	2.278±0.038	2.35±0.27	1.87±0.12	0.097±0.011	0.122±0.008
Abell 2390	4.808±0.15	4.08±0.44	2.93±0.45	0.117±0.013	0.164±0.026
Abell 1835	6.466±0.041	5.42±0.95	4.12±0.51	0.119±0.021	0.157±0.020
MS2137.3-2353	2.359±0.051	1.52±0.18	1.44±0.16	0.154±0.018	0.164±0.019
MACSJ0744.9+3927	2.467±0.10	2.31±1.01	2.43±0.41	0.107±0.047	0.102±0.018
ClJ1226.9+3332	3.879±0.064	3.51±0.74	3.44±0.55	0.111±0.023	0.113±0.018

Table 6.4: *Gas mass, total cluster mass and gas mass fraction, calculated at* R_{2500}.

Under the assumption of hydrostatic equilibrium and spherical symmetry, the total cluster mass within R_{2500} is calculated throught different approaches.

First no model is assumed to the gas temperature and density distributions. The total mass M_{2500}^{obs} is computed based solely on the spectral data points. The mass M_{2500}^{iso} is then calculated assuming that the hot, X-ray emitting gas, is described by a single temperature plasma.

The total cluster masses M_{2500}^{obs} calculated by taking a model independent approach, with the gradient of the gas density and temperature calculated considering the neighboring data points, present larger uncertainties than the ones obtained in the isothermal approach M_{2500}^{iso}. The reason for this discrepancy is the uncertainty in the gradient of the temperature which is calculated considering only two data points.

Assuming a model for the temperature distribution would reduce the uncertainty in the determination of the temperature gradient, but it would also result in correlated mass values and model dependence.

A better spatial resolution of the temperature profile, and precise determination of the temperature within each cluster shell, would provide significant improvement in the determination of the gas temperature gradient, and therefore, improved quality of the mass measurement.

The average temperature within R_{2500} is compared to the derived temperature at R_{2500}. The clusters hosting a cool core, show an average temperature systematically lower than the local temperature at R_{2500}. The cool core clusters in this sample are Abell 2390, Abell 1835 and MACSJ0744.9+3927.

For the clusters Abell 1413 and Abell 963, not hosting a cool core, the local temperature at R_{2500} is consistent with the average temperature measured within that radius, indicating an isothermal temperature distribution.

The galaxy cluster MS2137.3+2353 shows a temperature at R_{2500} consistent with the average temperature. Due to poor quality of the observation, which suffered from

soft protons flares and residual soft proton contamination, described in chapter 3, the derivation of the temperature profile of MS2137.3+2353 achieved in this study failed to properly resolve the cool core in this system.

The highest redshift cluster, ClJ1226.9+3332, presents a temperature at R_{2500} lower than the average temperature. For this cluster, the temperature profile, presented in chapter 5, shows a clear decrease in the temperature as a function of radius.

For six out of seven galaxy clusters in this sample, the assumption of an isothermal gas results in total cluster masses values consistent with the total masses obtained considering the local temperature at R_{2500} and the gradient of the temperature profile within the 1σ confidence interval. The only exception is the cluster Abell 1835, host of a strong cool core, and therefore, a significant temperature gradient. For this cluster the isothermal assumption results in a lower values for the total cluster mass.

The comparison between the average gas temperature, $\langle T_{2500} \rangle$, and the cluster temperature T_{2500} at R_{2500} is shown in table 6.1, and the effect of the temperature in the cluster mass calculation, together with the results of M_{2500} obtained by the different approaches are listed in table 6.2.

For the model dependent approach, a β model is assumed to describe the gas density. The total cluster mass is calculate considering both a non isothermal temperature profile (M^{β}_{2500}) and an isothermal distribution of the gas ($M^{\beta,iso}_{2500}$).

The total masses derived by assuming that the gas density is well described by a β model results in total masses consistent with the mass values from the non isothermal, model independent approach, for all galaxy clusters. Assuming an isothermal distribution for the gas temperature results in lower mass values for three clusters, Abell 963, Abell 2390 and Abell1835.

Both the Abell 2390 and Abell 1835 are systems hosting a cool core, it is therefore expected that the isothermal assumption compromises the computation of the cluster total mass.

For Abell 963, despite the temperature analysis indication of an isothermal system, this assumption combined to the β model describing the gas density distribution results in a slightly lower mass value.

The β model seems to describe the X-ray surface brightness profile of Abell 963 well, but for all galaxy clusters in this study, X-surface brightness profile, to which the β model was fit to, still carries contamination from the cosmic X-ray background. Despite adding a constant to the β model, aiming to account for the cosmic X-ray background contamination, the residual background contamination could affect the best fitting parameters of the β model.

A NFW model is fit to the clusters' observed total mass profiles M_{2500} . From the values of the best fitting parameters, the mass M^{NFW}_{2500} is derived and compared to the mass values M_{2500} obtained from spectral and spatial analysis, also listed in table 6.2. The observed mass profiles together with the best fit NFW model are shown in figure

6.3.

The contour plots illustrating the 1σ confidence interval of the NFW model parameters, central density, ρ_0, and the scale radius, r_s, are presented in figure 6.5.

The masses within R_{2500}, calculated based on the best fitting parameters of a NFW model fit to the observed mass profiles, agree within 1σ confidence interval to the model independent masses derived for five clusters. The clusters Abell 963 and Abell 2390 show a sightly lower value for M_{2500}^{NFW} when compared to the model independent mass M_{2500}^{obs}.

Inspection of the mass profile of these two systems show that the mass data point closest to R_{2500} is significantly higher than its neighboring data point, not producing a smooth profile, indicating the limitation of the method for these specific systems at this radius.

There is a possibility that the gradient of the gas density calculated considering the neighboring data points does not reproduce the real density slope at R_{2500} for these two clusters. Particularly for the cluster Abell 2390, which is known to be a disturbed system, the lack of resolution of the profiles can significantly compromise the determination of the gas density and temperature gradients.

The NFW model fit to the mass data points allow for the determination of the innermost cluster density ρ_0, and the scale radius r_s. The best fit value of r_s is combined to the value R_{2500} for each cluster to derive the concentration parameter at an overdensity of 2500. The mass profiles for most clusters in this study do not reach radii beyond R_{2500}, the correct determination of r_s is challenging if it lies further than the outermost mass bin radius.

The concentration parameter c_{2500} is calculated from the combination of R_{2500} and the best fit values of r_s for each galaxy cluster. The values obtained for the concentration parameter and best fitting NFW parameters are listed in table 6.3. Figure 6.4 is a plot of the concentration parameter c_{2500} as a function of cluster mass M_{2500}, where the relation obtained in this study is compared to the theoretical prediction from Macciò et al. (2008).

For the majority of systems in this study the concentration parameter c_{2500} values are significantly higher than the theoretical prediction. This discrepancy could be the result of an underestimation of the scale radius r_s. Also, the N-body simulations of Macciò et al. (2008) include dark matter only, while real galaxy clusters include, other than dark matter, X-ray emitting gas and stars, and the processes affecting the baryonic mass components, such as cooling and feedback, modify the overall mass distributions (Schmidt & Allen 2007). The values of r_s obtained in this study are compared to previous reported results in chapter 7.

The gas mass profiles are calculated from the spectral analysis by using the average density within each annulus and adding the gas shells. The values of the gas mass $M_{gas,2500}$ and cluster total mass M_{2500}^{obs} derived are compared to obtain the cluster's gas

mass fraction $f^{obs}_{gas,2500}$. Table 6.4 lists the values of $M_{gas,2500}$, M^{obs}_{2500}, M^{NFW}_{2500}, and the gas mass fractions $f^{obs}_{gas,2500}$ and $f^{NFW}_{gas,2500}$ for each galaxy cluster in this sample.

The gas mass fractions computed are compared to the results reported by Allen et al. (2008). The values of the model independent f_{gas} are consistent with the reported by Allen et al. (2008) for six clusters, with the result for the cluster MS2137.3+2353 presenting a higher f_{gas} value than the reported by Allen et al. (2008).

The poor quality of MS2137.3+2353 observation does not allow for a good resolution of the temperature profile for this cluster and results in a underestimation of the cluster temperature and temperature gradient at R_{2500}, affecting directly the derived cluster total mass. The gas mass fraction for this system is therefore overestimated due to the underestimation of the cluster total mass.

The comparison of the results discussed here to several other studies of galaxy clusters is shown in chapter 7.

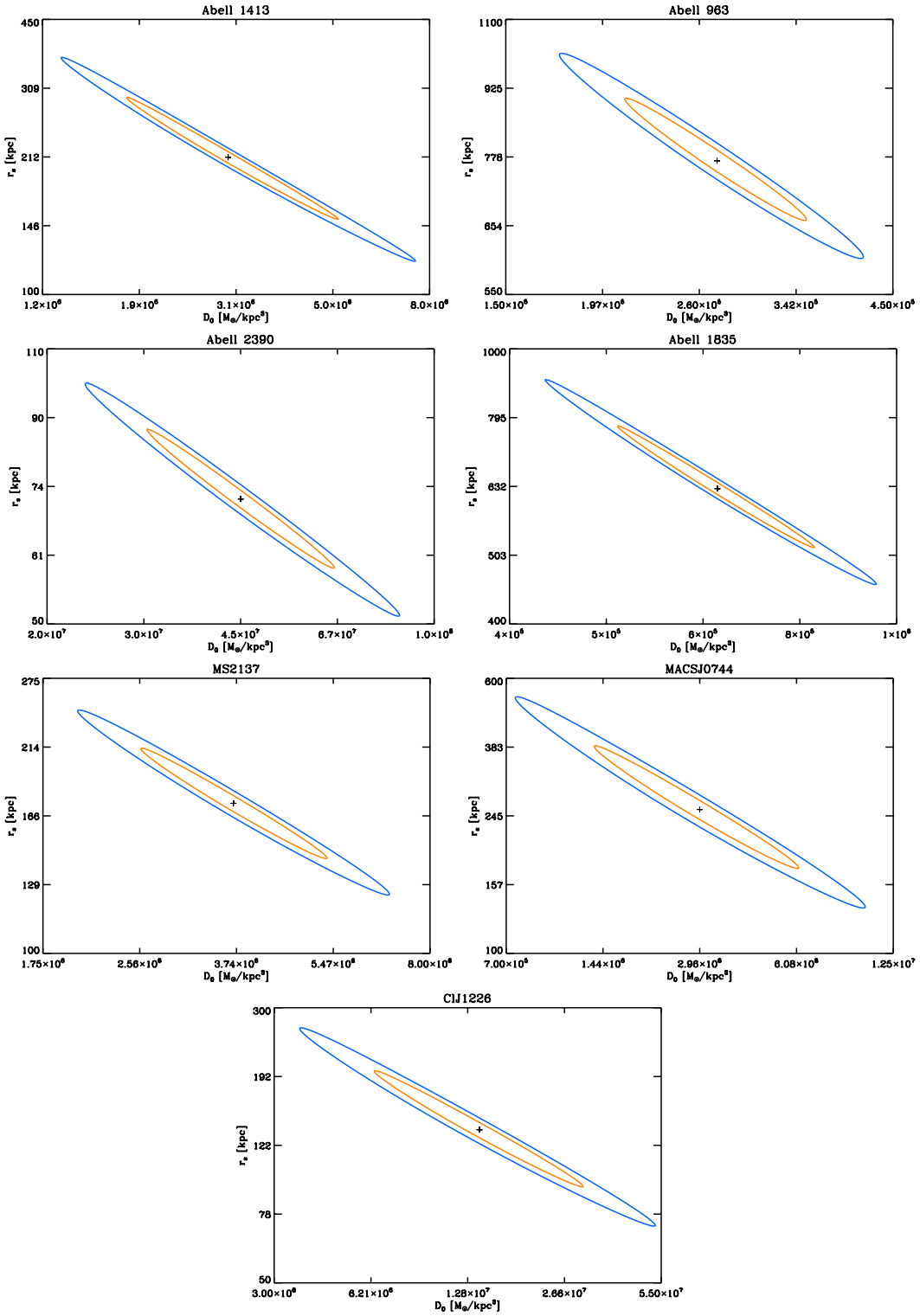

Figure 6.5: *Best fit parameters of the NFW model. Contour plots of the χ^2 minimization showing the 1σ (orange) and 2σ (blue)confidence intervals for the parameters rs and ρ_0 .*

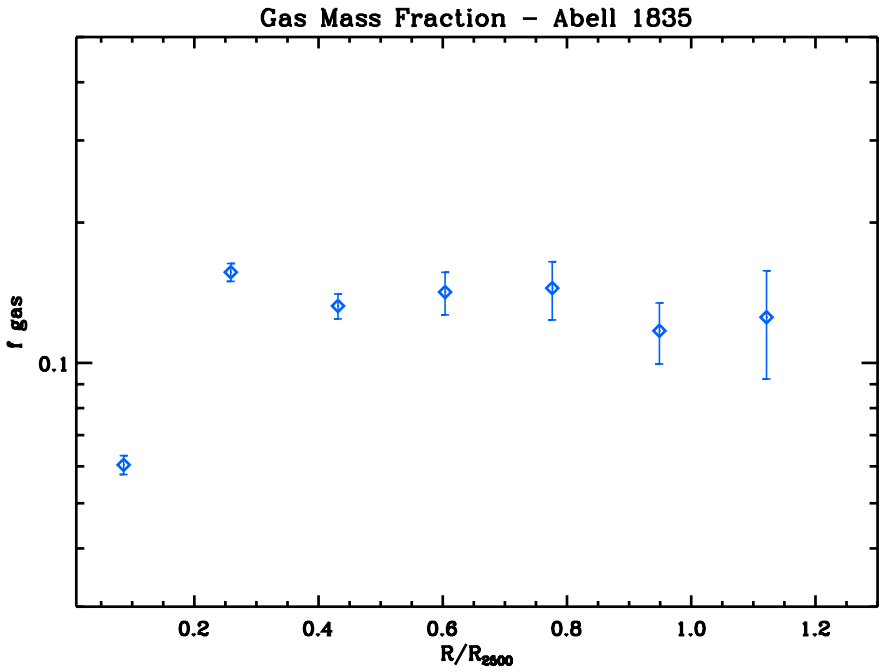

Figure 6.6: *Gas mass fraction profile of the galaxy cluster Abell 1835.*

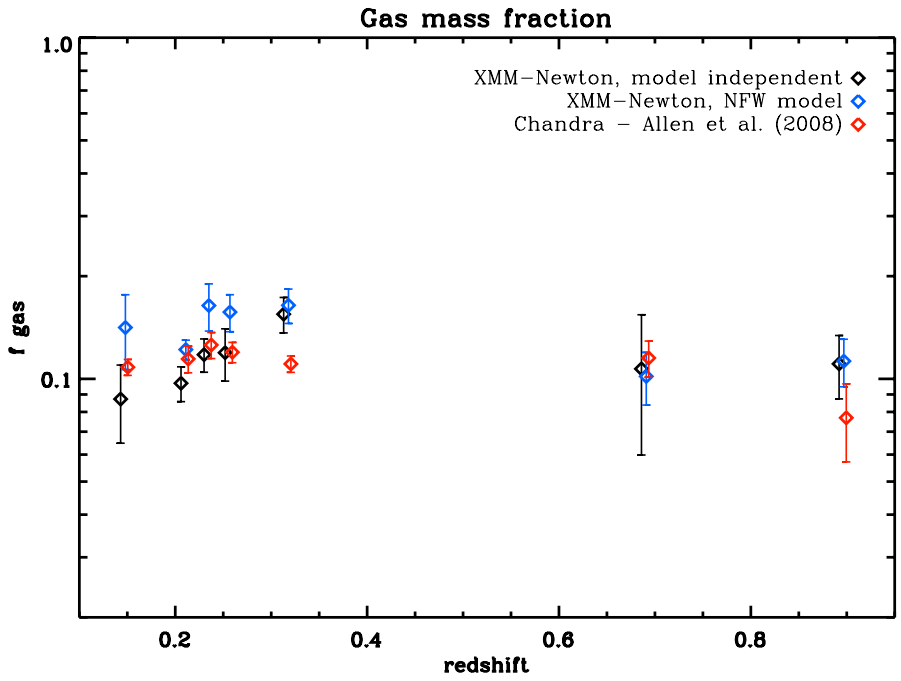

Figure 6.7: *Gas mass fraction as a function of redshift, calculated at* R_{2500}.

7

PREVIOUS STUDIES

"Det er ganske sandt,
hvad philosophien siger,
at livet maa forstaaes baglænds."

Søren Kirkegaard (1843)

ABSTRACT – *In this chapter, a brief comparison between the results derived in this study and some previous studies is presented. In this chapter the results of the gas mass fractions and mass distributions obtained in the present study are confronted to the most recent independent studies using X-rays. The observed X-ray mass profiles are compared to the most recent strong lensing results by Richard et al. (2010).The gas mass fractions obtained allow for constraints on cosmological parameters. The cosmological constraints from the XMM-Newton gas mass fractions are compared to the results reported in Allen et al. (2008).*

7.1 INTRODUCTION

The X-ray cluster sample analyzed in this study was selected from the XMM-Newton public archive. All systems discussed in this work have previous studies reported by several authors, including X-rays, gravitational lensing and multi-wavelength studies.

Previous studies report X-ray analysis from both XMM-Newton and Chandra of one of more clusters belonging to the sample studied here (e.g., Ettori et al. 2010; Allen et al. 2008; Schmidt & Allen 2007; Zhang et al. 2007; Maughan et al. 2007; Voigt & Fabian 2006; Allen et al. 2004; Pratt & Arnaud 2002; Allen et al. 2001).

X-ray measurements of cluster masses are made under the assumption of hydrostatic equilibrium and spherical symmetry. Added to these common assumptions, previous studies make use of different approaches for describing the gas density, temperature and total mass distributions, which combined allow for the derivation of the mass profile.

Gravitational lensing studies allow for the determination of the projected cluster mass along the line of sight. The X-ray and lensing methods are independent and complementary. As for the X-rays studies, gravitational lensing analysis of the systems

Cluster	$f_{gas,2500}^{obs}$	$f_{gas,2500}^{NFW}$	$f_{gas,2500}^{A08}$
Abell 1413	0.087±0.022	0.141±0.036	0.1082±0.0058
Abell 963	0.097±0.011	0.122±0.008	0.1144±0.0102
Abell 2390	0.117±0.013	0.164±0.026	0.1257±0.0110
Abell 1835	0.119±0.021	0.157±0.020	0.1197±0.0082
MS2137.3-2353	0.154±0.018	0.164±0.019	0.1106±0.0061
MACSJ0744.9+3927	0.107±0.047	0.102±0.018	0.1151±0.0140
ClJ1226.9+3332	0.111±0.023	0.113±0.018	0.0769±0.0198

Table 7.1: *Gas mass fractions at r_{2500} derived in this study and the reported by Allen et al. (2008) [A08].*

studied here are addressed by many authors (e.g., Richard et al. 2010; Zhang et al. 2010; Donnarumma et al. 2009; Mahdavi et al. 2008; Gavazzi 2005; Smith et al. 2005; Sand et al. 2004, 2002; Allen 1998).

The cluster mass distributions in clusters and parameters related to those distributions are reported by several authors considering different overdensities. To allow for the direct comparison of results, the focus is on studies reporting mass distributions at an overdensity of 2500.

7.2 THE GAS MASS FRACTION SAMPLE

One of the motivations of this study was independently measure, using XMM-Newton observations, the gas mass fractions reported and used by Allen et al. (2008) to study the evolution of the gas mass fraction and constrain cosmological parameters.

The method applied by Allen et al. (2008) to derive the gas mass and total mass profiles of the clusters (Schmidt & Allen 2007) makes use of the X-ray surface brightness profile and the deprojected X-ray gas temperature, under the assumptions of hydrostatic equilibrium, spherical symmetry and total mass distributions described by an NFW model. The X-ray surface brightness profile and the model for the mass distribution are used together with an enhanced version of the Cambridge X-ray deprojection code (White et al. 1997) to predict the temperature profile of the X-ray gas. The radial resolution of the temperature profiles obtained in this way is much higher than the coarse radial temperature profiles obtained in the present study, derived considering solely the spectral data. The method used by Allen et al. (2008) does not require parametric models for the X-ray temperature, gas density or surface brightness to measure the total gravitating mass, but still depends on a an NFW model to parametrize the total mass distributions. The values of the gas mass fractions obtained in this study and that reported by Allen et al. (2008) are listed in table 7.1 and shown in figure 6.7.

The model independent gas mass fractions from XMM-Newton are in agreement

Cluster	redshift	Exposure time XMM-Newton (ks)	Exposure time Chandra (ks)
A1413	0.143	62.3	64.5
A963	0.206	22.1	35.8
A2390	0.230	9.8	79.2
A1835	0.252	68.4	18.0 + 10.3
MS2137.3-2353	0.313	10.8	20.0 + 26.6
MACSJ0744.9+3927	0.686	60.1	17.1 + 15.6 + 41.3
ClJ1226.9+3332	0.890	64.6	25.7 + 26.3

Table 7.2: *Exposure times after data filtering for the XMM-Newton observations used in this study and the Chandra observations used by Allen et al. (2008).*

with the values reported from Chandra data (Allen et al. 2008) for six out of seven systems. The cluster MS2137.3-2353 presents a higher gas mass fraction. The total cluster mass of MS2137.3-2353 is likely to be underestimated due to the residual soft proton contamination affecting the XMM-Newton observation of this system.

The confidence intervals of f_{gas} reported by Allen et al. (2008) are, on average, 58% lower than those computed for $f^{obs}_{gas,2500}$, derived in this study in a model independent approach. This difference reflects the lack of assumptions on the cluster's mass distribution and the coarse radial sampling, limited by the quality of the data used.

Comparing to the uncertainties in $f^{NFW}_{gas,2500}$, obtained by fitting an NFW model to the observed mass profiles, the confidence intervals by Allen et al. (2008) are, on average, 43% lower. Here the difference between the average confidence interval is smaller than for the model independent approach, but also reflects that the coarse radial sampling and the lack of mass bins at larger radii affects the quality of the fit.

As discussed in chapter 6, a greater spatial resolution of the temperature profile, and precise determination of the temperature within each cluster shell, would provide significant improvement in the determination of the gas temperature gradient, and therefore, improved quality of the mass measurement.

The spatial resolution of the temperature profile depends of the number of X-ray photons observed and on the resolution of the instrument used. The comparison between XMM-Newton and Chandra (Allen et al. 2008) exposure times after all cleaning and screening processes were applied is shown in table 7.2. For most systems considered in this study, the Chandra observations have superior exposure time than the XMM-Newton observations. Combining multiple observations, and therefore increasing the number of X-ray photons available, would allow for improvement in the quality of the mass measurements.

7.3 COSMOLOGICAL CONSTRAINTS

The gas mass fractions from XMM-Newton observations derived in this study can be used to constrain cosmological parameters.

To investigate which information XMM-Newton observations can provide on cosmological parameters, the gas mass fractions obtained in this study are submitted to the same Monte Carlo Markov Chain (MCMC) method used by Allen et al. (2008) for the cosmological analysis (Rapetti et al. 2005, 2007).

The model independent gas mass fractions derived from XMM-Newton observations of the clusters studied here were given to David Rapetti (private communication), who performed the cosmological analysis assuming standard priors (see Allen et al. 2008) on the cosmological baryon density $\Omega_b h$ (Freedman et al. 2001; Kirkman et al. 2003) and an extra prior restraining Ω_Λ to be positive values. The description and discussion of the methods applied by David Rapetti to derive cosmological constraints is beyond the scope of this thesis. Information on the MCMC method is found in Lewis & Bridle (2002),Rapetti et al. (2005, 2007), and references therein.

The 1σ and 2σ confidence constraints in the Ω_m, Ω_Λ plane for the XMM-Newton gas mass fraction data are shown in figure 7.1, together with the constraints reported by Allen et al. (2008).

The cosmological constraints from the XMM-Newton gas mass fraction data are in agreement with the results reported by Allen et al. (2008). The confidences contours for Ω_m are fair, while the low number of clusters in this sample does not allow for significant constraints on Ω_Λ.

7.4 PREVIOUS X-RAY STUDIES

The cluster's masses and gas mass fraction obtained in this study are in general good agreement with several previous X-ray studies.

Nulsen et al. (2010) report a model independent method implemented in XSPEC to compute the total mass of a galaxy cluster. Common to this study are the galaxy clusters Abell 1413, Abell 2390 and Abell 1835.

The mass values within R_{2500} reported by Nulsen et al. (2010) are $(3.6^{+0.5}_{-0.6}) \times 10^{14} M_\odot$ for Abell 1413, $(4.0^{+0.5}_{-1.1}) \times 10^{14} M_\odot$ for Abell 2390 and $(7.1^{+1.0}_{-2.1}) \times 10^{14} M_\odot$ for Abell 1835. For all three galaxy clusters there is agreement with the results reported in this study.

In the work by Mahdavi et al. (2008), measurements of spatially resolved weak gravitational lensing and hydrostatic X-ray masses for a sample of 18 clusters of galaxies are reported using data from the Canada-France-Hawaii Telescope (CFHT) and Chandra. Of the 18 galaxy clusters, Abell 963 and Abell 2390 are common to this study.

X-ray masses measured within R_{2500} by Mahdavi et al. (2008) are $(1.92 \pm 0.21) \times 10^{14} M_\odot$ for Abell 963 and $(3.75 \pm 0.31) \times 10^{14} M_\odot$ for Abell 2390. The gas mass fractions reported at the same radius are 0.11 ± 0.01 and 0.14 ± 0.01 for Abell 963 and Abell 2390

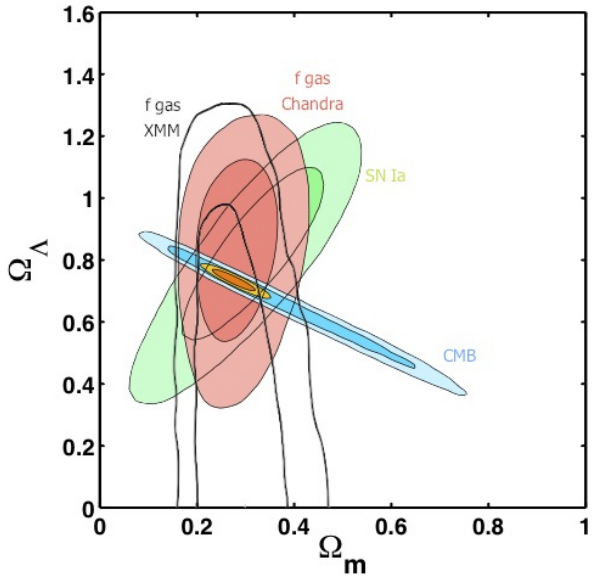

Figure 7.1: *Cosmological constraints showing the 1 and 2σ confidence constraints in the Ω_m, Ω_Λ plane for the XMM-Newton gas mass fraction data (black, no filling) over plotted on the results reported by Allen et al. (2008) for the Chandra gas mass fraction data (red contours). [Original figure from Allen et al. (2008)].*

respectively. Both the total X-ray masses and gas mass fractions reported by Mahdavi et al. (2008) are in agreement with the results reported here.

Maughan et al. (2007) report XMM-Newton and Chandra observations of the galaxy cluster ClJ1226.9+3332 and a detailed X-ray mass analysis of this high redshift cluster. The overall X-ray properties of this system such as temperature, metal abundance and mass profiles derived by Maughan et al. (2007) are reproduced in the present study and there is general agreement between the properties derived.

Maughan et al. (2007) report values of $(3.00 \pm 0.2) \times 10^{13} M_\odot$ and $(3.2^{+0.5}_{-0.4}) \times 10^{14} M_\odot$ for the gas mass and total cluster mass respectively, and a gas mass fraction of 0.10 ± 0.01, calculated at $R_{2500} = 430$ kpc. Both the gas mass and total cluster mass derived in this study are slightly higher than the value reported by Maughan et al. (2007), with the cluster total mass and gas mass fraction agreeing within the 68% confidence interval. The reason for these discrepancies is the value of R_{2500} considered by Maughan et al. (2007) which is lower than the value assumed in this study.

Vikhlinin et al. (2006) present gas and total mass profiles of 13 galaxy clusters, derived from Chandra data. Common to this study are Abell 1413 and Abell 2390. Vikhlinin et al. (2006) report masses values within R_{2500} of $(3.08 \pm 0.19) \times 10^{14} M_\odot$ and $(3.50 \pm 0.28) \times 10^{14} M_\odot$ for Abell 1413 and Abell 2390 respectively. The gas mass fractions reported are 0.092 ± 0.003 for Abell 1413 and 0.127 ± 0.005 for Abell 2390. For both systems, the total cluster's masses and gas mass fractions agree with the results

Cluster	r_s	r_s (D09)	r_s (S07)	r_s (M07)	r_s (V06)	r_s (A01)
A 1413	$0.21^{+0.08}_{-0.06}$	-	$0.48^{+0.13}_{-0.09}$	-	2.05	-
A 963	$0.77^{+0.13}_{-0.11}$	-	$0.39^{+0.12}_{-0.08}$	-	-	-
A 2390	$0.07^{+0.02}_{-0.01}$	-	-	-	1.18	$0.76^{+1.59}_{-0.39}$
A 1835	$0.63^{+0.15}_{-0.11}$	-	$0.58^{+0.08}_{-0.09}$	-	-	$0.55^{+0.18}_{-0.09}$
MS2137	$0.17^{+0.04}_{-0.03}$	$0.15^{+0.02}_{-0.02}$	$0.18^{+0.02}_{-0.02}$	-	-	$0.16^{+0.03}_{-0.03}$
MAC0744	$0.26^{+0.13}_{-0.08}$	-	$0.32^{+0.18}_{-0.09}$	-	-	-
ClJ1226	$0.14^{+0.06}_{-0.04}$	-	-	0.18 ± 0.04	-	-

Table 7.3: *Comparison between the bets fit values of the scale radius (listed in units of Mpc) obtained in this study and previous X-ray studies by Donnarumma et al. (2009) [D09], Schmidt & Allen (2007) [S07], Maughan et al. (2007) [M07], Vikhlinin et al. (2006) [V06] and Allen et al. (2001) [A01].*

reported in the present study.

In table 7.3 the best fit NFW model parameter r_s derived for this cluster sample is listed together with the value reported by several authors. The NFW model appears to be a particularly good fit to the observed XMM-Newton mass profiles of Abell 1835, MS2137.3-2353, MACSJ0744.9+3927 and ClJ1226.9+3332, see chapter 6. The r_s value derived for these clusters are in agreement with the values reported by Schmidt & Allen (2007), Donnarumma et al. (2009), Maughan et al. (2007) and Allen et al. (2001). The best fit value of r_s for the clusters Abell 1413, Abell 963 and Abell 2390, is not in agreement with the previous studies reported here. The value of χ^2 minimization, presented in table 6.3, also indicates that the NFW model is a poor fit to the observed mass profile derived in this study for these three systems.

7.5 GRAVITATIONAL LENSING

Gravitational lensing and X-ray observations are two independent methods used to determine the total gravitating mass in galaxy clusters. Discrepancies between the mass determinations from the two methods have been studied by several authors (e.g., Loeb & Mao 1994; Miralda-Escude & Babul 1995; Kneib et al. 1995; Mahdavi et al. 2007; Zhang et al. 2008; Gavazzi 2005; Richard et al. 2010). The underlying assumptions on both X-ray and lensing methods could be responsible for these discrepancies, e.g. projection effects along the line of sight affecting the lensing analysis, lack of hydrostatic equilibrium due to non thermal pressure support of the gas, inhomogeneity of the gas in the central parts of the cluster.

The cluster's X-ray total masses derived in this study are compared to the masses obtained by strong lensing analysis reported by Richard et al. (2010). The studies by Richard et al. (2010) present statistical analysis of a sample of 20 strong lensing clusters, for which five are common to the present study using XMM-Newton observations. The

strong lensing analysis is based on high-resolution Hubble Space Telescope imaging of the cluster cores and follow-up spectroscopic observations using the Keck-I telescope.

The study by Richard et al. (2010) reports the total cluster mass within a radius of 250 kpc. The strong lensing model was extended to radii beyond R_{2500} by Johan Richard (private communication), allowing for the comparison to the model independent X-ray masses presented in this thesis.

The 3D X-ray masses were projected on the sky in order to compare to the projected 2D strong lensing masses. Both strong lensing and projected X-ray mass profiles are shown in figure 7.2.

The XMM-Newton mass profile of the clusters Abell 1413 and Abell 963 are in good agreement with independent measurements from strong lensing studies. For the cluster Abell 1835, hosting a strong cool core, the XMM-Newton mass profile is in agreement with the strong lensing profile at larger radii (> 600 kpc). The XMM-Newton mass profile of Abell 2390 is in agreement with the strong lensing profile at intermediate radii, but presents a slightly lower value at larger radii.

The strong lensing mass profile of the galaxy cluster MS2137.3-2353 is significantly higher than the mass profile obtained in this study with XMM-Newton data. The X-ray total cluster mass could be biased low due to residual soft proton contamination of the XMM-Newton observation of this system.

A similar discrepancy between lensing and X-ray masses for this particular cluster is also reported by Gavazzi (2005) when comparing his lensing model to X-ray observations by Allen et al. (2001). Gavazzi (2005) suggests that a prolate halo aligned towards the line of sight could explain discrepancies between his best fit lensing model and the X-rays constraints by Allen et al. (2001). Morandi et al. (2010a,b) suggest that accounting for the 3D geometry can solve the discrepancy between the mass determined from X-ray and gravitational lensing observations.

The X-ray mass of the cluster MS2137.3-2353 measured at R_{2500} derived in the present study has a value of $(1.52 \pm 0.18) \times 10^{14} M_{\odot}$. The mass value is slightly lower than the $(1.89^{+0.25}_{-0.31}) \times 10^{14} M_{\odot}$ reported by Allen et al. (2001), but is still consistent within the 68% confidence interval.

Work by Donnarumma et al. (2009) presents new X-ray and strong lensing mass measurements of MS2137.3-2353, where the discrepancy between the strong lensing and the X-ray mass measurement at larger radii is not found. Donnarumma et al. (2009) shows that the strong lensing mass estimate is affected by the modeling of the brightest cluster galaxy (BCG) and the uncertainty on the BCG mass determination could introduce a systematic bias in the lensing measurements. The strong lensing mass profile by Donnarumma et al. (2009) shows lower mass values and seems to be closer to the XMM-Newton mass values obtained in this study. Donnarumma et al. (2009) also report a scale radius r_s of $153.1^{+23.3}_{-19.5}$ kpc, consistent with the value derived here.

For all clusters in this sample, at small radii (< 100 kpc) the strong lensing mass

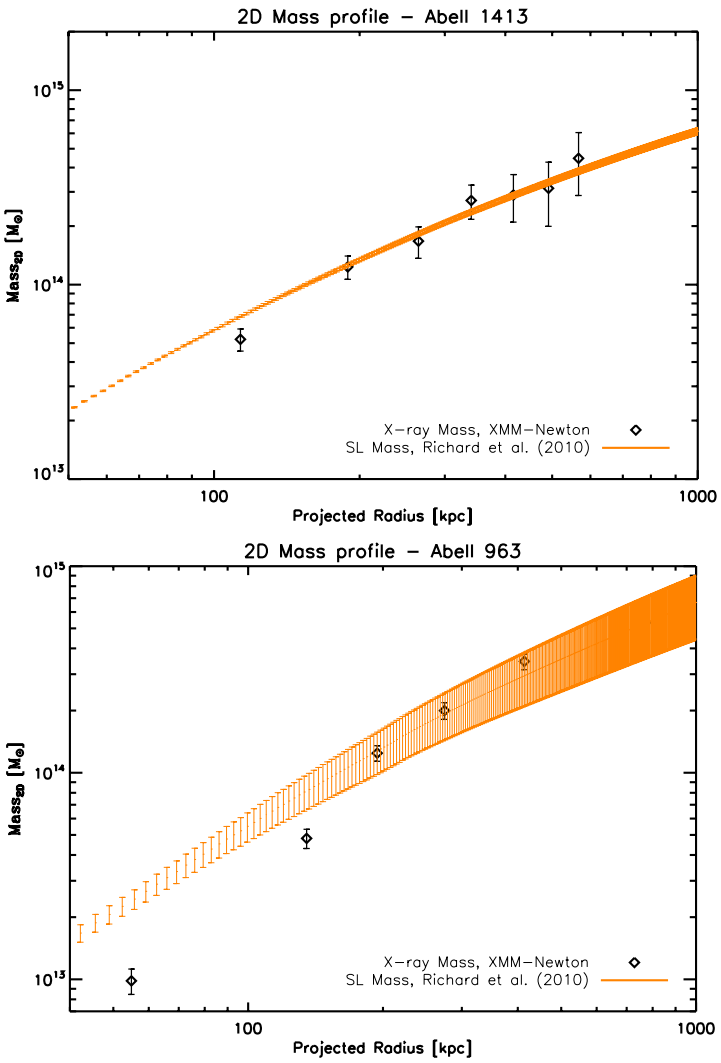

Figure 7.2: *The reprojected, two dimensional mass profiles of Abell 1413, Abell 963 and Abell 2390, derived in this study, and the strong lensing mass profiles by Richard et al. (2010). Figure continues.*

profiles of Richard et al. (2010) are discrepant to the mass profiles determined from the XMM-Newton data. The resolution of the mass profiles from XMM-Newton derived in this study may be to coarse to provide comparable results at low radii, or the assumption of hydrostatic equilibrium of the hot intra cluster gas may not valid at the innermost regions of these galaxy clusters. Also since the lensing technique is sensitive to the integrated mass along the line of sight, the discrepancy may be related to substructures on these scales and could in principle result in larger central lensing masses, due to alignments with mass concentrations along the line of sight not related to the cluster (Wambsganss et al. 2005).

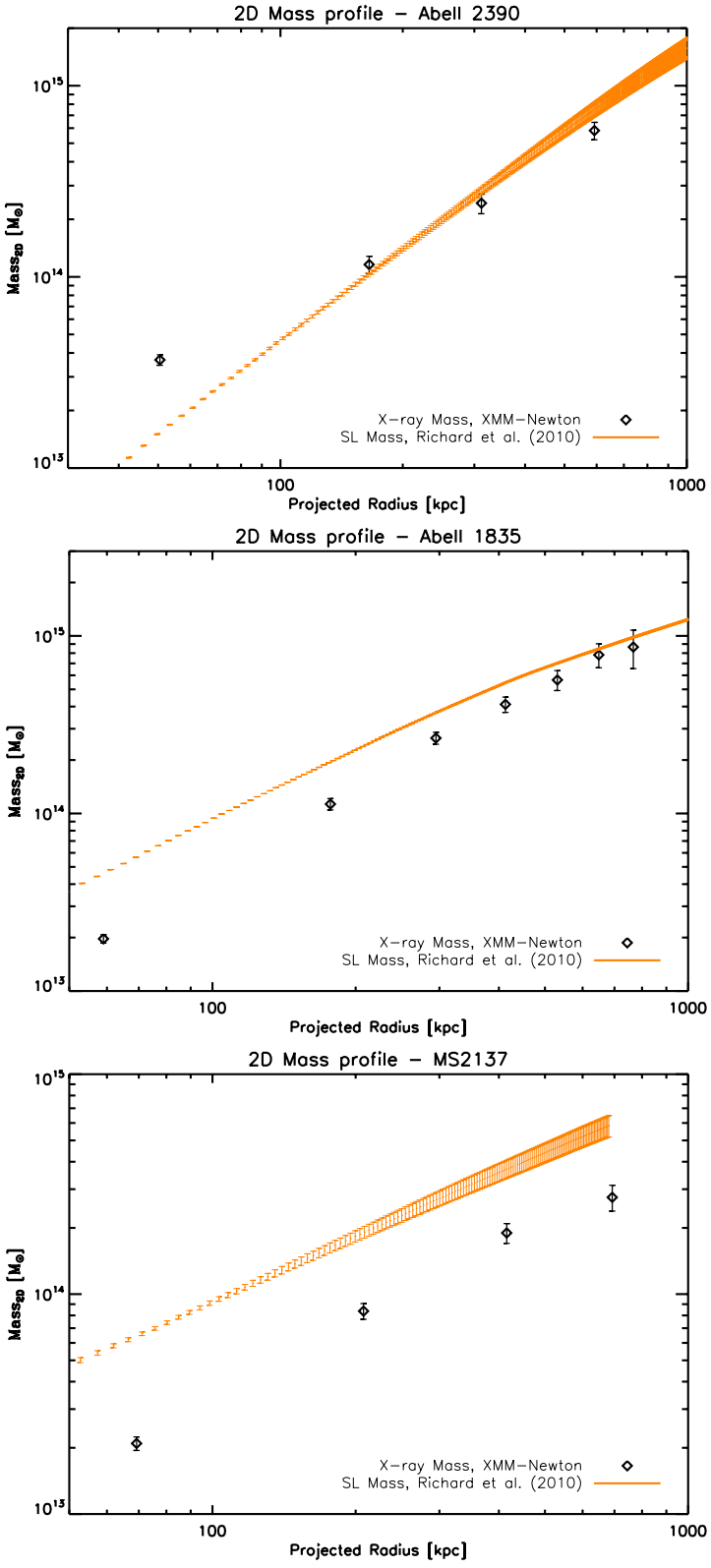

Figure 7.2 *continued, two dimensional mass profiles of Abell 1835 and MS2137.3-2353.*

7.6 DISCUSSION

The results of the cluster's masses, gas mass fractions and NFW model best fit parameters obtained by analysis of XMM-Newton data were compared to several previous studies.

The gas mass fractions derived in the model independent approach are in agreement with the previous study of Allen et al. (2008) and can be used to constrain cosmological parameters.

Despite the lack of assumptions on the total mass distribution and distributions of the gas temperature and density, the analysis of XMM-Newton data allows for determination of the cluster's total gravitating masses, gas masses and therefore, gas mass fractions, in concordance to previous independent studies of the same systems that use and combine data from different observatories.

The best fitting values derived for the NFW model parameter r_s are in agreement with previous results for the clusters Abell 1835, MS2137.3-2353, MACSJ0744.9+3927 and ClJ1226.9+3332.

For the cluster Abell 1413, r_s value is lower than the one reported by Schmidt & Allen (2007) and by Vikhlinin et al. (2006). The r_s value derived for Abell 963 is significantly higher compared to the previous result by Schmidt & Allen (2007). The cluster Abell 2390 has a r_s value significantly lower than the previous result by Vikhlinin et al. (2006) and by Allen et al. (2001). The NFW model fit to the observed mass profile of these systems is of poor quality and the best fit value of the parameter r_s derived is not reliable.

The systems presenting good agreement between the r_s value derived here and previous independent studies are all at higher redshift than the three systems presenting discrepancies.

The comparison between mass profiles from XMM-Newton derived in this study and strong lensing profiles by Richard et al. (2010) is presented and reasonable agreement is observed for the two lowest redshift systems, Abell 1413 and Abell 963. The clusters Abell 1835 and Abell 2390 show partial agreement, while for MS2137.3-2353 the strong lensing mass seems to be overestimating the total cluster mass profile.

The comparison and agreement to previous independent studies is a necessary consistence check and indicates robustness of the XMM-Newton mass values derived in this study.

8

SUMMARY AND CONCLUSIONS

"So Long, and Thanks for All the Fish."

Douglas Adams, The Hitchhiker's Guide to the Galaxy (1984)

8.1 SUMMARY OF MAIN RESULTS

This thesis presents a study where the gas mass fraction of seven clusters of galaxies, observed with XMM-Newton, was measured by using a model independent approach.

The primary aim of this work was to check for biases and determine the magnitude of uncertainties involved in the derivation of the cluster masses by comparing the results obtained from XMM-newton observations to previous X-rays studies from Chandra and XMM-Newton, and optical studies of strong gravitational lensing.

To the present date, studies of the gas mass fraction in galaxy clusters considering systems at high redshifts are largely based on Chandra observations. The two main reasons for that are the effect of the background affecting XMM-Newton detectors and the need to model the effects of the PSF when dealing with relaxed clusters with very sharply peaked, cool cores.

The effect of the background and PSF in the XMM-Newton observations of this sample of clusters were investigated. For the spatial resolution of the radial bins considered in this sample, the effect of the PSF smearing is negligible. For the background affecting the XMM-Newton observations used, the situation is different. Failure to properly consider the background introduces a systematic error in the determination of the temperature profile, and consequently in the derivation of the total mass of the clusters.

The radial distributions of temperature, metal abundance and density of the gas were determined through spectral analysis, and the X-ray surface brightness profile is obtained from the X-ray images.

The derivation of the integrated gas mass was done by considering the discrete density data points from spectral analysis only, without assuming any models. The average density within each gas shell is derived from the normalization of the X-ray spectrum and the relative uncertainty associated with it is fairly small, of the order of

1-3%. As a result, the 1σ confidence interval of the gas mass is on average 2% of the gas mass value.

The accuracy in the determination of the gas mass fraction is thus mainly dependent on the uncertainty in the total cluster mass measurement. Other than the model independent approach, where the gradients of the temperature and density are determined based solely on the spectral data points, tests of the different assumptions on the distributions of temperature and density and their effect on the determination of the cluster mass and uncertainty were performed.

The uncertainty in the mass measurement is reduced by 75% on average, if the assumption of an isothermal gas is adopted, showing clearly that the main source of uncertainty lies on the determination of the temperature gradient. This assumption results in mass values which are in general agreement with the model independent mass values derived, but the mean mass value is systematically lower for the clusters hosting a cool core.

In general, the X-ray surface brightness profile is well fit by a single β model, with the exception being the galaxy cluster Abell 1835, hosting a strong cool core, where the single β model could not reproduce the innermost cluster brightness. The use of a β model to derive the gradient of the density results in a total mass in good agreement with the model independent values.

To fit an NFW model to the model independent mass profiles results in uncertainties in the total mass value computed at R_{2500} that are on average 40% lower than the model independent one. This improvement in the confidence interval may not reproduce the true mass error, particularly for clusters with only a few mass data points or where the NFW model results in a poor fit.

The uncertainty resulting from the model independent approach is more conservative, and significant improvement can be achieved by greater spatial resolution of the temperature profile. This can be accomplished with longer exposure times combined with the careful consideration of the effects of background and PSF presented in this thesis.

The model independent measurements of the gas mass fractions from XMM-Newton observations are in overall agreement with the results from Chandra, but for the cluster MS2137.3-2353 a systematic effect is expected due to residual soft proton contamination.

The gas mass fractions from XMM-Newton, derived in this study, can be used to constrain cosmological parameters. In this work, a test of the capability of XMM-Newton observations on cosmological constraints results in consistence with the constraints by Allen et al. (2008) with Chandra data based on a much larger sample. The constraint on Ω_m is comparable to previous results and, as expected from a small sample of clusters, no significant constraint on dark energy was achieved. A larger sample of clusters from XMM-Newton ($\gtrsim 50$ clusters), would provide better constraints on Ω_Λ.

Although the sample of clusters considered in this study is small compared to the most recent previous studies using Chandra observations (Ettori et al. 2009; Allen et al. 2008), and more recent work on XMM-Newton observations at low redshift range (Ettori et al. 2010), it represents a complementary and independent study of the gas mass fraction in clusters of galaxies and motivates the use of XMM-Newton to constrain cosmological parameters.

8.2 FUTURE WORK

A natural continuation of this work is to combine several observations of each galaxy cluster in this sample to obtain greater resolution in the determination of the distributions of the gas density and temperature within the potential of the clusters. To make proper use of the X-ray surface brightness profile, implementing a deprojection technique would also improve the predictions on these distributions.

Combining several observations of the same system would allow for improvement in the determination of the total gravitating mass, gas mass and therefore, the derivation of the gas mass fraction. A high signal-to-noise detection gives the possibility to determine the mass distributions in clusters to larger radii without relying on parametric models.

The results obtained in this study permit the investigation of scaling relations of the properties of the clusters, such as the mass-temperature relation and its evolution with redshift. A more detailed study would improve the determination of the distribution of the metals in the intra cluster medium and test the evolution of the chemical enrichment in clusters.

Both the determination of cosmological parameters and evolution of the properties of clusters would benefit enormously from a larger sample of cluster observations over a wide redshift range.

As for the individual systems, two clusters of galaxies in this sample, Abell 2390 and MACSJ0744.9+3927, have significant presence of substructure. The regions affected were excised and not considered in the X-ray analysis performed here. The assumption of hydrostatic equilibrium used to compute the masses of clusters is weakened when applied to disturbed clusters, thus, it would be interesting to investigate how much the inclusion of substructure affects the proper determination of cluster observables and derived masses.

BIBLIOGRAPHY

Allen, S. W. 1998, MNRAS, 296, 392

Allen, S. W., Ettori, S., & Fabian, A. C. 2001, MNRAS, 324, 877

Allen, S. W., Rapetti, D. A., Schmidt, R. W., et al. 2008, MNRAS, 383, 879

Allen, S. W., Schmidt, R. W., Ebeling, H., Fabian, A. C., & van Speybroeck, L. 2004, MNRAS, 353, 457

Allen, S. W., Schmidt, R. W., & Fabian, A. C. 2002, MNRAS, 334, L11

Allen, S. W., Schmidt, R. W., Fabian, A. C., & Ebeling, H. 2003, MNRAS, 342, 287

Anders, E. & Grevesse, N. 1989, Geochim. Cosmochim. Acta, 53, 197

Arnaud, K. A. 1996, in Astronomical Society of the Pacific Conference Series, Vol. 101, Astronomical Data Analysis Software and Systems V, ed. G. H. Jacoby & J. Barnes, 17–+

Bartelmann, M. & Schneider, P. 2001, Phys. Rep., 340, 291

Bennett, C. L., Halpern, M., Hinshaw, G., et al. 2003, ApJS, 148, 1

Bialek, J. J., Evrard, A. E., & Mohr, J. J. 2001, ApJ, 555, 597

Biviano, A. 2000, in Constructing the Universe with Clusters of Galaxies

Böhringer, H. & Werner, N. 2010, A&A Rev., 18, 127

Bookbinder, J. 2010, in Presented at the Society of Photo-Optical Instrumentation Engineers (SPIE) Conference, Vol. 7732, Society of Photo-Optical Instrumentation Engineers (SPIE) Conference Series

Bullock, J. S., Kolatt, T. S., Sigad, Y., et al. 2001, MNRAS, 321, 559

Burles, S., Nollett, K. M., & Turner, M. S. 2001, ApJ, 552, L1

Byram, E. T., Chubb, T. A., & Friedman, H. 1966, Science, 152, 66

Cavaliere, A. & Fusco-Femiano, R. 1976, A&A, 49, 137

Churazov, E., Gilfanov, M., Forman, W., & Jones, C. 1996, ApJ, 471, 673

Comerford, J. M. & Natarajan, P. 2007, MNRAS, 379, 190

David, L. P., Jones, C., & Forman, W. 1995, ApJ, 445, 578

Davis, T. M., Mörtsell, E., Sollerman, J., et al. 2007, ApJ, 666, 716

De Luca, A. & Molendi, S. 2004, A&A, 419, 837

Dolag, K., Bartelmann, M., Perrotta, F., et al. 2004, A&A, 416, 853

Donnarumma, A., Ettori, S., Meneghetti, M., & Moscardini, L. 2009, MNRAS, 398, 438

Ettori, S., Borgani, S., Moscardini, L., et al. 2004, MNRAS, 354, 111

Ettori, S. & Fabian, A. C. 1999, MNRAS, 305, 834

Ettori, S., Gastaldello, F., Leccardi, A., et al. 2010, A&A, 524, A68+

Ettori, S., Morandi, A., Tozzi, P., et al. 2009, A&A, 501, 61

Ettori, S., Tozzi, P., & Rosati, P. 2003, A&A, 398, 879

Evrard, A. E. 1997, MNRAS, 292, 289

Fabian, A. C. & Allen, S. W. 2003, in Texas in Tuscany. XXI Symposium on Relativistic Astrophysics, ed. R. Bandiera, R. Maiolino, & F. Mannucci, 197–208

Forman, W., Kellogg, E., Gursky, H., Tananbaum, H., & Giacconi, R. 1972, ApJ, 178, 309

Freedman, W. L., Madore, B. F., Gibson, B. K., et al. 2001, ApJ, 553, 47

Friedman, H., Lichtman, S. W., & Byram, E. T. 1951, Physical Review, 83, 1025

Fukugita, M., Hogan, C. J., & Peebles, P. J. E. 1998, ApJ, 503, 518

Gavazzi, R. 2005, A&A, 443, 793

Giacconi, R. 1980, Scientific American, 242, 80

Giacconi, R. 2003, Reviews of Modern Physics, 75, 995

Giacconi, R., Gursky, H., Paolini, F. R., & Rossi, B. B. 1962, Physical Review Letters, 9, 439

Giacconi, R., Gursky, H., & Waters, J. R. 1964, Nature, 204, 981

Golwala, S. R., Aguirre, J. E., Basu, K., et al. 2009, in ArXiv Astrophysics e-prints, Vol. 2010, astro2010: The Astronomy and Astrophysics Decadal Survey, 96–+

Harrison, F. A., Boggs, S., Christensen, F., et al. 2010, in Presented at the Society of Photo-Optical Instrumentation Engineers (SPIE) Conference, Vol. 7732, Society of Photo-Optical Instrumentation Engineers (SPIE) Conference Series

Hickox, R. C. & Markevitch, M. 2007, ApJ, 671, 1523

Hoekstra, H., Franx, M., Kuijken, K., & Squires, G. 1998, ApJ, 504, 636

Jansen, F. A. & XMM Science Operations Team. 2000, in Bulletin of the American Astronomical Society, Vol. 32, Bulletin of the American Astronomical Society, 724–+

Jenkins, A., Frenk, C. S., White, S. D. M., et al. 2001, MNRAS, 321, 372

Jones, C. & Forman, W. 1984, ApJ, 276, 38

Kaastra, J. S., Paerels, F. B. S., Durret, F., Schindler, S., & Richter, P. 2008, Space Sci. Rev., 134, 155

Kaiser, N. & Squires, G. 1993, ApJ, 404, 441

Kalberla, P. M. W., Burton, W. B., Hartmann, D., et al. 2005, A&A, 440, 775

Kellogg, E., Gursky, H., Leong, C., et al. 1971, ApJ, 165, L49+

King, I. R. 1972, ApJ, 174, L123+

Kirkman, D., Tytler, D., Suzuki, N., O'Meara, J. M., & Lubin, D. 2003, ApJS, 149, 1

Kneib, J. P., Mellier, Y., Pello, R., et al. 1995, A&A, 303, 27

Komatsu, E., Smith, K. M., Dunkley, J., et al. 2010, ArXiv e-prints

Kravtsov, A., Gonzalez, A., Vikhlinin, A., et al. 2009, in ArXiv Astrophysics e-prints, Vol. 2010, astro2010: The Astronomy and Astrophysics Decadal Survey, 164–+

Kravtsov, A. V., Nagai, D., & Vikhlinin, A. A. 2005, ApJ, 625, 588

Kravtsov, A. V., Vikhlinin, A., & Nagai, D. 2006, ApJ, 650, 128

Kuntz, K. D. & Snowden, S. L. 2000, ApJ, 543, 195

Kuntz, K. D. & Snowden, S. L. 2001, ApJ, 554, 684

Lewis, A. & Bridle, S. 2002, Phys. Rev. D, 66, 103511

Loeb, A. & Mao, S. 1994, ApJ, 435, L109

Macciò, A. V., Dutton, A. A., & van den Bosch, F. C. 2008, MNRAS, 391, 1940

Mahdavi, A., Hoekstra, H., Babul, A., & Henry, J. P. 2008, MNRAS, 384, 1567

Mahdavi, A., Hoekstra, H., Babul, A., et al. 2007, ApJ, 664, 162

Maughan, B. J., Jones, C., Jones, L. R., & Van Speybroeck, L. 2007, ApJ, 659, 1125

Miralda-Escude, J. & Babul, A. 1995, ApJ, 449, 18

Morandi, A., Pedersen, K., & Limousin, M. 2010a, ArXiv e-prints

Morandi, A., Pedersen, K., & Limousin, M. 2010b, ApJ, 713, 491

Muanwong, O., Thomas, P. A., Kay, S. T., & Pearce, F. R. 2002, MNRAS, 336, 527

Navarro, J. F., Frenk, C. S., & White, S. D. M. 1995, MNRAS, 275, 720

Navarro, J. F., Frenk, C. S., & White, S. D. M. 1997, ApJ, 490, 493

Nulsen, P. E. J., Powell, S. L., & Vikhlinin, A. 2010, ApJ, 722, 55

Peebles, P. J. & Ratra, B. 2003, Reviews of Modern Physics, 75, 559

Pen, U. 1997, New Astronomy, 2, 309

Pratt, G. W. & Arnaud, M. 2002, A&A, 394, 375

Predehl, P., Andritschke, R., Bornemann, W., et al. 2007, in Presented at the Society of Photo-Optical Instrumentation Engineers (SPIE) Conference, Vol. 6686, Society of Photo-Optical Instrumentation Engineers (SPIE) Conference Series

Press, W. H. & Schechter, P. 1974, ApJ, 187, 425

Rapetti, D., Allen, S. W., Amin, M. A., & Blandford, R. D. 2007, MNRAS, 375, 1510

Rapetti, D., Allen, S. W., & Weller, J. 2005, MNRAS, 360, 555

Reese, E. D., Kawahara, H., Kitayama, T., et al. 2010, ApJ, 721, 653

Richard, J., Smith, G. P., Kneib, J., et al. 2010, MNRAS, 404, 325

Roncarelli, M., Ettori, S., Dolag, K., et al. 2006, MNRAS, 373, 1339

Rosati, P., Borgani, S., & Norman, C. 2002, ARA&A, 40, 539

Sand, D. J., Treu, T., & Ellis, R. S. 2002, ApJ, 574, L129

Sand, D. J., Treu, T., Smith, G. P., & Ellis, R. S. 2004, ApJ, 604, 88

Sarazin, C. L. 1988, X-ray emission from clusters of galaxies, ed. Sarazin, C. L.

SAS User Guide, E. X.-N. S. 2010, User Guide to the XMM-Newton Science Analysis System - Issue 7.0, User Guide to the XMM-Newton Science Analysis System

Sasaki, S. 1996, PASJ, 48, L119

Schindler, S. 1999, A&A, 349, 435

Schindler, S. 2002, Mem. Soc. Astron. Italiana, 73, 965

Schmidt, R. W. & Allen, S. W. 2007, MNRAS, 379, 209

Smith, G. P., Kneib, J., Smail, I., et al. 2005, MNRAS, 359, 417

Smith, S. 1936, Contributions from the Mount Wilson Observatory / Carnegie Institution of Washington, 532, 1

Snowden, S. L., Egger, R., Freyberg, M. J., et al. 1997, ApJ, 485, 125

Snowden, S. L., Mushotzky, R. F., & Kuntz. 2010, COOKBOOK FOR ANALYSIS PROCEDURES FOR XMM-NEWTON EPIC MOS OBSERVATIONS OF EXTENDED OBJECTS AND THE DIFFUSE BACKGROUND - Version 4.0, XMM-ESAS cookbook

Snowden, S. L., Mushotzky, R. F., Kuntz, K. D., & Davis, D. S. 2008, A&A, 478, 615

Spergel, D. N., Bean, R., Doré, O., et al. 2007, ApJS, 170, 377

Sunyaev, R. A. & Zeldovich, Y. B. 1970, Comments on Astrophysics and Space Physics, 2, 66

Sunyaev, R. A. & Zeldovich, Y. B. 1972, Comments on Astrophysics and Space Physics, 4, 173

Takahashi, T., Mitsuda, K., Kelley, R., et al. 2010, in Presented at the Society of Photo-Optical Instrumentation Engineers (SPIE) Conference, Vol. 7732, Society of Photo-Optical Instrumentation Engineers (SPIE) Conference Series

Tinker, J., Kravtsov, A. V., Klypin, A., et al. 2008, ApJ, 688, 709

Tomlin, S. 1999, Nature, 401, 32

Tyson, J. A., Kochanski, G. P., & dell'Antonio, I. P. 1998, ApJ, 498, L107+

Vikhlinin, A., Kravtsov, A., Forman, W., et al. 2006, ApJ, 640, 691

Vikhlinin, A., Murray, S., Gilli, R., et al. 2009, in ArXiv Astrophysics e-prints, Vol. 2010, astro2010: The Astronomy and Astrophysics Decadal Survey, 305–+

Voigt, L. M. & Fabian, A. C. 2006, MNRAS, 368, 518

Wambsganss, J., Bode, P., & Ostriker, J. P. 2005, ApJ, 635, L1

Werner, N., de Plaa, J., Kaastra, J. S., et al. 2006, A&A, 449, 475

White, D. A., Jones, C., & Forman, W. 1997, MNRAS, 292, 419

White, S. D. M., Navarro, J. F., Evrard, A. E., & Frenk, C. S. 1993, Nature, 366, 429

White, S. D. M. & Rees, M. J. 1978, MNRAS, 183, 341

XMM Users Handbook, E. X.-N. S. 2010, XMM-Newton Users Handbook - Issue 2.8.1, XMM-Newton Users Handbook

Zhang, Y., Finoguenov, A., Böhringer, H., et al. 2007, A&A, 467, 437

Zhang, Y., Finoguenov, A., Böhringer, H., et al. 2008, A&A, 482, 451

Zhang, Y., Okabe, N., Finoguenov, A., et al. 2010, ApJ, 711, 1033

Zwicky, F. 1933, Helvetica Physica Acta, 6, 110

Zwicky, F. 1937, ApJ, 86, 217